

INAUGURAL-DISSERTATION

zur Erlangung der Doktorwürde der
Naturwissenschaftlich-Mathematischen
Gesamtfakultät der Ruprecht-Karls-Universität
Heidelberg

vorgelegt von
Dipl.-Chem. Heike Boehm
geboren in Haan/Rheinland

Tag der mündlichen Prüfung: 09. Dezember 2008

MICROMECHANICAL PROPERTIES AND STRUCTURE OF
THE PERICELLULAR COAT OF LIVING CELLS MODULATED
BY NANOPATTERNED SUBSTRATES

Gutachter:

Prof. Dr. J. P. Spatz

Physikalisch-Chemisches-
Institut
Universität Heidelberg

Max-Planck-Institut
für Metallforschung

Prof. Dr. J. Sleeman

Institut für Mikrovaskuläre Biologie
und Pathobiologie
Universität Heidelberg

Forschungszentrum
Karlsruhe

Abstract

The articular cartilage mainly consists of a complex extracellular matrix (ECM), which is subject to a high mechanical loading. To counteract the ongoing abrasion, a specialized cell type is embedded within the ECM. These so-called chondrocytes constantly recondition the ECM. To live and even divide in such a mechanically challenging environment, chondrocytes are protected by a several micron thick pericellular coat (PCC). The PCC is of vital biological importance for example in cell proliferation and migration, but also affected by increasing age or in conjunction with diseases like osteoarthritis. Water provides the essential part of the PCC and the coat therefore remains invisible in all light microscopy techniques. Hyaluronan (HA) forms the vital backbone of the PCC together with its HA-binding proteins. Whereas the individual components and even their molecular interactions are well understood, the mesoscopic structure of the PCC still lies in an unexplored field of science. Especially in matters of understanding the mechanisms for the PCC's dynamic adjustment and, more general, force transductions detailed studies on this topic are of lively interest.

In this thesis, new methods for the visualization of the PCC have been established, enabling its three dimensional visualization and its micromechanical characterization on living cells. The application of these techniques revealed the dynamic adjustment of the PCC during cell division, motility and phagocytosis. The mesoscopic structure of the PCC was successfully deduced and supported by model systems of grafted HA. Furthermore, the interplay between the ECM and the PCC has been investigated by adhesion-experiments mimicking the ECM in a well defined way.

Visualizing the Dynamic Pericellular Coat

The dynamic adjustment of the PCC could be observed on RCJ-P cells, serving as a well established model system for HA-rich PCCs, as well as on other cell lines and primary cells with only thin PCCs. This was accomplished by applying a novel fluorescent marker specific for HA consisting of an eGFP labeled HA-binding link module (GFPn): (a) The adjustment of the PCC during cell motility could be observed in transfected RCJ-P cells expressing fluorescently marked actin. The correlation of strong actin stress fibers on cell protrusions and GFPn stained PCCs indicate, that the PCC is rearranged during motility, where exploring protrusions are surrounded by significantly smaller PCCs. (b) The PCC is further adjusted during cell division, where it is accumulated at the cleavage furrow surrounding it on all sides. (c) During phagocytosis, particles larger than one micron are initially excluded by the PCC, but eventually taken up by the cell. This phagocytotic activity follows an exponential time curve depending on the size of the particle and can be enhanced by enzymatic digestion of the PCC. In order to enable the uptake of particles, the PCC needs to undergo conformational or structural changes to allow the penetration of the particles. This is evident by a significant change of PCC thickness in the presence of phagocytosable particles even if the cell does not take them up.

Characterization of the Mesoscopic Architecture of the PCC

In order to analyze the molecular architecture of the PCC, the relative distribution of HA has been mapped with GFPn in spinning disk microscopy providing for the first time distribution profiles of HA within the PCC. The experiments showed a decreasing concentration profile throughout the PCC preceded by an initial increase at the cell membrane over $1.7 \mu\text{m}$ (st. dev. 0.5). The increase has successfully been correlated to short membrane protrusions also visible in scanning electron microscopy (SEM) and in reflection interference microscopy (RICM). As the slope of the decreasing GFPn

intensity scales with the thickness of the PCC, a relative coordinate system has been defined based on the local width of the PCC which was determined with an independent technique, the particle exclusion assay (PEA). The new coordinate system enables the comparison of the HA distribution profiles of different cells and samples and of profiles obtained by other techniques.

Micromechanical profiles of the PCC were successfully acquired by exploiting the position sensitive detection of passive particle tracking microrheology (ptMR). Consistent with the HA distribution profiles, the micromechanical profile shows a decreasing viscoelasticity throughout the PCC, which can not be observed in cells devoid of PCCs. In contrast to other mechanical PCC measurement techniques, this method is not affected by the cell's mechanical properties and allows unobtrusive measurements of these soft hydrous coats on living cells.

Based on the obtained profiles, the mesoscopic architecture of the PCC was deduced. Correlating the obtained profiles to polymer physical theories revealed a mismatch with the expected profile of monodisperse end-grafted polymer brushes proposed by Alexander and de Gennes and refined by Milner, Witten and Cates. In contrast to these well defined model systems, the HA within the PCC is not only attached at its end to its synthase incorporated in the outer cell membrane, but also along the chain to specific cell membrane receptors. Additionally, the flexibility of the HA chain is modified by attached HA-binding proteins. Taking these consideration into account, a HA polymer brush stretched out by its binding proteins is proposed. Assuming each HA chain is bound at least twice to the cell membrane the suggested model matches the observed concentration profiles.

Regulating PCC Expression by Controlled Integrin Activation

Further, the PCC expression depends on the cell's ECM interactions. Chondrocytes interact with the ECM of the articular cartilage as well as with their PCC. These interactions can be decoupled in adhesion studies with different surface functionalizations mimicking the ECM interactions. The thickness of the PCC is not related to the adhesion area, the PCC-to-adhesion area ratio determines the proliferation rate. Adhesive nanostructured substrates generally allow controlling the density and spacing of integrin activating peptides on an otherwise inert background very precisely and are thus an ideal platform to study clustering effects. In order to perform the cell experiments on a larger scale in an improved fashion, the dip-coating process for the nanostructured surfaces was optimized. The improved production design ensures large scale homogenous surfaces with improved geometrical as well as translational order. Comparison of RCJ-P cells on a nanostructured surface with interparticle spacings of 70 nm to homogenous gold surfaces, showed not only a significantly reduced adhesion area, but also significantly smaller PCC thicknesses on the nanostructured surfaces after both 12 and 24 h.

Zusammenfassung

Das mechanisch stark beanspruchte Knorpelgewebe in Gelenken besteht zum überwiegenden Teil aus einer komplexen extrazellulären Matrix (ECM). Chondrozyten, spezialisierte in der Matrix eingebettete Zellen, erneuern diese fortwährend, um deren Abrieb und Verschleiß zu verhindern. Die Zellen werden durch eine mikrometerdicke Perizelluläre Matrix (PCC) geschützt, die ein Überleben und ein Teilen der Zellen trotz der hohen mechanischen Belastung ermöglicht. Die PCC ist von entscheidender Bedeutung für eine Vielzahl weiterer biologischer Prozesse, wie der Motilität, der Zellalterung und der Osteoarthrose.

Auf molekularer Ebene ist die Zusammensetzung und Wechselwirkung der verschiedenen PCC-Komponenten gut verstanden: Der überwiegende Teil der PCC besteht aus Wasser und ist damit mit lichtmikroskopischen Methoden nicht detektierbar. Das Rückgrat der PCC wird aus stark hydratisierten Hyaluronsäurepolymeren und daran angebundenen HA-Bindungsproteinen gebildet.

Informationen über die mesoskopische Struktur der PCC sind allerdings kaum vorhanden. Diese ist jedoch von fundamentaler Bedeutung für das Verständnis der Kraftübertragung aus dem Knorpelgewebe auf die Zellen sowie zur Aufklärung des Mechanismus, der den Zellen eine aktive Anpassung der PCC ermöglicht.

Im Rahmen dieser Arbeit wurden daher neue Methoden zur Visualisierung der PCC etabliert, die eine dreidimensionale Darstellung, sowie die mikromechanische Charakterisierung der PCC lebender Zellen ermöglichen. Diese Methoden erlaubten die Untersuchung der dynamischen Anpassung der PCC bei Zellteilung, Motilität und Phagozytose. Die mesoskopische Struktur der PCC konnte von den erhaltenen Messdaten abgeleitet und durch entsprechende Modellsysteme aus endständig angebundenen HA Molekülen unterstützt werden. Darüber hinaus konnte das Wechselspiel von PCC und ECM mit Hilfe von Adhäsionsstudien auf homogenen sowie nanostrukturierten Oberflächen, welche die ECM-Wechselwirkungen kontrollieren, untersucht werden.

Visualisierung der PCC und ihrer Dynamik

Die dynamische Anpassung der PCC wurde an RCJ-P Zellen, die als gut etabliertes Modellsystem für HA reiche PCCs dienen, wie auch an anderen Zell-Linien und primären Chondrozyten mit nur sehr dünnen PCCs untersucht. Dazu wurde ein neuer HA spezifischer Fluoreszenzmarker verwendet, der aus einem eGFP markierten HA-Bindungsmodul besteht (GFPn). Dieser ermöglichte auch die Beobachtung der dynamischen Anpassung der PCC von sich bewegenden transfizierten RCJ-P Zellen, die fluoreszenzmarkiertes Aktin exprimierten. Die Korrelation zwischen einer starken Aktinfaserbildung an Zellaustülpungen und einer lokalen verringerten GFPn Intensität legt nahe, dass die PCC reorganisiert wird, um eine effektive Zellmotilität zu ermöglichen. Auch während der Zellteilung wird die PCC verändert, wobei sie sich an allen Seiten der Teilungsfurche anreichert. Ebenso erfolgt eine Anpassung der PCC während der Phagozytose: Die PCC verhindert zunächst die aktive Aufnahme von Partikeln mit einem Durchmesser größer als ein Mikrometer. Mit der Zeit erfolgt eine Aufnahme durch die Zelle, wobei die Phagozytoseaktivität einem exponentiellen Zeitverlauf folgt, der von der Größe der Partikel abhängt und durch einen enzymatischen Abbau der PCC beschleunigt werden kann. Um die Aufnahme der Partikel zu ermöglichen, verändert sich die PCC. Dies ist an einer Abnahme der PCC-Dicke in Anwesenheit von Partikeln zu erkennen, die bereits vor einer erkennbaren Aufnahme der Partikel einsetzt.

Charakterisierung der mesoskopischen Struktur der PCC

Um die molekulare Architektur der PCC zu ermitteln, wurde die relative Verteilung des entscheidenden Gerüstbausteins, HA, mit Hilfe von GFPn im Spinning Disk Mikroskop untersucht. Erstmals wurde damit die Bestimmung des HA-Verteilungsprofils in der PCC ermöglicht. Diese zeigt eine zum Rand hin abnehmende HA-Konzentration innerhalb der PCC. Unmittelbar an der Zellmembran steigt die HA Konzentration zunächst über einen Bereich von $1,7 \mu\text{m}$ (st. dev. 0.5) an. Dieser Anstieg konnte mit einer rauen Zellmembran korreliert werden, die auch im Raster-Elektronen-Mikroskop (REM) und im Reflektions-Interferenz-Mikroskop (RICM) erkennbar ist. Der GFPn-Intensitätsabfall ist direkt von der Dicke der PCC abhängig. Die Bestimmung der PCC-Dicke durch eine unabhängige Methode erlaubte die Definition eines relativen Koordinatensystems, mit dessen Hilfe die Profile mehrerer Zellen auf verschiedenen Proben oder mit unterschiedlichen Messmethoden bestimmte Profile verglichen werden können.

Mikromechanische Profile konnten mit Hilfe orts aufgelöster Mikrorheologie erhalten werden. Sie zeigen einen dem HA-Verteilungsprofil entsprechenden abnehmenden Verlauf der Viskoelastizität von der Zellmembran hin zum Rand der PCC. Im Gegensatz zu anderen Messmethoden zur Charakterisierung der PCC wird die mikrorheologische Technik nicht durch die mechanischen Eigenschaften der angrenzenden Zelle beeinflusst. Aufgrund der nicht-invasiven Messmethoden lassen sich die Charakterisierungstechniken an weichen, hydrierten PCCs lebender Zellen einsetzen.

Ausgehend von den Fluoreszenz- und den mikromechanischen PCC-Profilen konnte die mesoskopische Struktur der PCC abgeleitet werden. Diese Struktur lässt sich nicht mit den Konzentrationsprofilen der von Alexander und deGennes postulierten Polymerbürsten oder deren Erweiterung durch Milner, Witten und Cates beschreiben. Bei der PCC handelt es sich im Gegensatz zu den wohl definierten Modellsystemen um ein erheblich komplexeres System, in dem die HA-Moleküle nicht nur endständig, sondern auch an weiteren Punkten entlang der Polymerkette an Membranrezeptoren gebunden sind. Weiterhin wird durch die Anbindung von HA-Bindungsproteinen die Flexibilität lokal beeinflusst. Basierend auf diesen Beobachtungen wurde für die PCC ein HA-Polymerbürsten-Modell vorgeschlagen, welches die experimentellen Konzentrationsverläufe beschreibt: Die HA-Moleküle sind jeweils mindestens zweimal an die Zellmembran angebunden und liegen aufgrund der angebundenen HA-Bindungsmoleküle in gestreckter Form vor.

Adhäsionsstudien zur kontrollierten PCC-Ausbildung

Die Ausbildung der PCC wird wesentlich durch Wechselwirkungen der Zelle mit der ECM des Knorpelgewebes bestimmt. Diese ECM-Wechselwirkungen können mit Hilfe von Adhäsions-Studien, in kontrollierter Form dargestellt werden. Damit ist eine detaillierte Analyse des Einflusses der ECM auf die PCC-Ausbildung möglich: Sowohl die Größe der PCC als auch die Adhäsionsfläche werden durch die ECM beeinflusst. Das Verhältnis von PCC zu Adhäsionsfläche scheint direkt die Proliferationsrate zu bestimmen. Eine verbesserte Kontrolle der adhäsionsvermittelnden Liganden konnte durch nanostrukturierte Oberflächen ermöglicht werden. Um Zellexperimente auf einer entsprechend großen nanostrukturierten Oberfläche durchführen zu können, wurde die Tauchbeschichtung zur Oberflächenherstellung optimiert. Dadurch konnten großflächige homogene Oberflächen mit verbesserter geometrischer und translatorischer Ordnung erzielt werden. RCJ-P Zellen, die auf diesen nanostrukturierten Oberflächen mit einem Goldpartikelabstand von 70 nm wuchsen, zeigten im Vergleich zu homogenen Goldoberflächen, die gleichermaßen funktionalisiert waren, eine signifikant geringere Adhäsionsfläche und eine signifikant dünnere PCC sowohl nach 12 als auch nach 24 h.

Contents

1	Introduction	1
1.1	Biological Relevance of the PCC	2
1.2	Composition of the PCC	4
1.2.1	Hyaluronan	4
1.2.2	Hyaladherins	4
1.2.3	Model System for the PCC	6
1.3	Passive Microrheology (MR)	7
1.3.1	Brownian Motion	7
1.3.2	Viscoelastic Solutions	8
1.3.3	Inhomogeneities	10
1.3.4	Microrheology on Biological Samples	10
2	Visualizing the Dynamic PCC	13
2.1	Particle Exclusion Assay (PEA)	15
2.1.1	PEAs Enable the Indirect Visualization of the PCC	15
2.2	Specific Fluorescent Staining of Hyaluronan	17
2.2.1	Current Status of HA Staining Methods	17
2.2.2	Staining the PCC of Living Cells with GFPn	18
2.2.3	Visibility of Very Thin PCCs with GFPn Stainings	19
2.3	Standard Cell Culture Procedures Influence the Size of the PCC	22
2.4	Dynamics of the PCC	23
2.4.1	The PCC is Rearranged During Motility	23
2.4.2	The PCC Assists Cell Division	24
2.4.3	Phagocytosis through the PCC	26
3	Characterization of the Mesoscopic Architecture of Pericellular Coats	33
3.1	Visualization of the 3D-Structure of the PCC	35
3.1.1	RCJ-P Cells are Enveloped by a Thick PCC on all Non-Adhered Membranes	35
3.2	Mapping the HA Distribution within the PCC	38
3.2.1	HA Distribution Profiles Show Consistent Curve Progressions	39
3.2.2	Short Microvilli Influence the Profile Close to the Cell Membrane	39
3.2.3	Impact of Photobleaching on the Description of the Fluorescent Decrease	41
3.2.4	Analysis of the Decreasing HA Concentration	43
3.2.5	Discussion of Possible Impacts of GFPn Staining on the Results	44
3.3	Micromechanical Profile of the PCC	46

3.3.1	The Viscoelastic Properties of the PCC Change Gradually Towards the Cell Membrane	46
3.3.2	The Different Cells and Different Areas do not Lead to Enlarged Distributions of the Diffusive Exponent	49
3.3.3	The Obtained Microrheological Profile is Meaningful	51
3.3.4	The Loss and Storage Modulus can Only be Calculated with Great Uncertainty	52
3.4	Deducing the Mesoscopic Structure of the PCC	56
3.4.1	Hyaluronan is a Flexible Polymer	56
3.4.2	Linear Flexible Polymers in Solution	57
3.4.3	Organization of Hyaluronan within the PCC	58
3.4.4	A Brush-like Structure could be Observed in Model Systems	60
3.4.5	Polymer Theory for Endgrafted, Monodisperse Polymers	62
3.4.6	Side-On Grafting Leads to Concentration Profiles which are More Closely Related to the Observed Profiles	63
3.5	Correlating the Micromechanical Profile to the HA Distribution Profile	66
3.5.1	Conclusion and Outlook	67
4	Regulating PCC Expression by Controlled Integrin Activation	69
4.1	Integrin Activation Influences Cell Behaviour	71
4.1.1	Advantages of Peptides in Adhesion Studies	71
4.1.2	The PCC can be Controlled with Adhesion Receptors	72
4.1.3	Analyzing Integrin Activation Induced Changes on Chondrocytes	75
4.2	Block-Copolymer Micellar Nanolithography	79
4.3	Quality Control of Nanopatterned Surfaces	83
4.3.1	Particle Size Distribution	83
4.3.2	Long and Short Range Order of Nanostructured Surfaces	83
4.3.3	Homogeneity of the Inter-Particle Spacing Across the Surface	86
4.3.4	Characterization of the Translational Short Range Order	88
4.3.5	Characterization of the Geometrical Short Range Order	89
4.3.6	Implications of the Particle Arrangement for Cell Experiments	89
4.4	Optimization of the Nano-Structured Surfaces for Cell Experiments	91
4.4.1	Variations of the Micellar Solutions Solvent	91
4.5	Unexpected Solution Surface Effects can be Utilized to Control the Interparticle Spacing	92
4.5.1	Confined solution surface leads to linear increasing interparticle distances	93
4.5.2	Trapped Solvent Vapors Influence Interparticle Distances	97
4.5.3	First Cell Experiments on Optimized Surfaces	100
5	Materials and Methods	103
5.1	Imaging Techniques	103
5.1.1	Electron Microscopy	103
5.1.2	Light Microscopy	103
5.1.3	Reflection Interference Contrast Microscopy (RICM)	106
5.1.4	Spinning Disc Microscopy	109
5.2	Cultivating the Different Cells	109
5.2.1	Rat Chondrocyte Cell Line RCJ-P	109
5.2.2	Primary Human Cells (HCH)	110
5.2.3	Transfected HEK Cells (HK2GFP)	110
5.3	Cell Protocols	111

5.3.1	Preparing Cell Samples	111
5.3.2	Particle Exclusion Assay with Erythrocytes	111
5.3.3	Membrane Staining	112
5.3.4	Fixation of Adherent Cells	112
5.3.5	Hyaluronidase Treatment	112
5.3.6	mCherry Actin Transfection of RCJ-P Cells	112
5.3.7	Purification of the eGFP Labelled Link Module GFPn	115
5.4	MR	118
5.4.1	Microrheology Chamber	118
5.4.2	Tracer Particles	118
5.4.3	Microscope Setup	119
5.4.4	Calibration with Solutions of Known Properties	120
5.4.5	MRcell	121
5.5	Surface Preparation	122
5.5.1	Cleansing of Glass Surfaces	122
5.5.2	Fibronectin- and Collagen-Coating of Glass Surfaces	122
5.5.3	Thin Film Coating with a Sputter Coater	123
5.5.4	Nanostructured Surfaces	123

Literature

Abbreviations

AFM	atomic force microscopy
Ar	argon
ATP	adenosin triphosphate
Au	gold
BCA	bicinchoninic acid
BCML	block-copolymer micellar nanolithography
bHABP	biotinylated HA-binding protein
BSA	bovine serum albumin
BSE	back scattered electrons in SEM
CD44	cell membrane receptor specific for hyaluronan
cmc	critical micellar concentration
cn	collagen
DAPI	4',6-diamidino-2-phenylindole for DNA staining
DIC	differential interference contrast microscopy
DiO	lipophilic carbocyanine dye
DMSO	dimethylsulfoxide
DNA	desoxyribonucleic acid
DW-RICM	dual-wavelength RICM
DWS	difussing wave spectroscopy
ECM	extra cellular matrix
EDTA	ethylenediaminetetraacetic acid
eGFP	enhanced green fluorescent protein
ERM	closely related protein family of ezrin, radixin and moesin
ESEM	environmental scanning electron microscope
FACE	fluorophore-assisted carbohydrate electrophoresis
FBS	fetal bovine serum
FITC	fluorescein isothiocyanate
fn	fibronectin
fps	frames per secon
FWHM	full width at half maximum
GAG	glycosaminoglycan
GFP	green fluorescent protein
GFPn	eGFP labeled link module of rat neurocan
GSER	generalized Stokes-Einstein relation
HA	hyaluronan
HA _{dase}	hyaluronidase
HARE	HA receptor for endocytosis
HAS	hyaluronan synthase
HCH	primary human chondrocytes from PromoCell
HEK	human embryonic kidney cells
HeLa	an immortal cell line derived from cervical cancer cells
HEPES	4-(2-hydroxyethyl)-1-piperazineethanesulfonic acid
HIS	histidine
HK2GFP	GFPn expressing HEK cells
LP	long pass
MR	microrheology
MSD	mean squared displacement
Ni-NTA	nickel-nitriloacid
PnVP	poly-n-vinylpyridine (n = 2 or 4)
PAGE	polyacrylamid gel electrophoresis
PBS	phosphate buffered saline

PCC	pericellular coat
PCM	pericellular matrix
PEA	particle exclusion assay
PEG	poly(ethyleneglycol)
PIC	protein inhibitor cocktail
PS	polystyrene
ptMR	particle tracking microrheology
QD	quantum dots
RCJ-P	rat chondrocytes from fetal calvaria
RDF	radial distribution function
REF	rat embryonic fibroblast
RGD	arginine-glycine-aspartic acid
RHAMM	receptor for HA-mediated motility
RICM	reflection interference contrast microscopy
3 λ -RICM	triple-wavelength RICM
SDS	sodium dodecyl sulfate
SE	secondary electrons in SEM
SEM	scanning electron microscopy
SLB	supported lipid bilayer
st. dev.	standard deviation
TCA	trichloroacetic acid
TEM	transmission electron microscopy
UDP	uridine diphosphate
VIS	visible light
WGA	wheat germ agglutinin
WT	wild type

Mathematical Abbreviations

α	diffusive exponent or constant
β	drag coefficient
χ	Huggins parameter
ξ	mesh size
η	viscosity
$[\eta]$	intrinsic viscosity
η_s	viscosity of solvent
η_{sp}	specific viscosity
ψ_{RDF}	short range order determined based on the 1st peak of the RDF
ψ_6	sixfold bond-orientational order parameter
ψ_{V6}	hexagonal Voronoi parameter
ρ	density
ρ_a	areal density
σ	surface tension
σ	grafting density
τ	lag time
A	area
A_s	solution surface area
c	concentration
c_m	micellar concentration
Ca	capillary number
d	absolute distance towards the cell membrane in micrometers
D	diffusion constant

d_{acc}	accessible depth
d_s	interparticle spacing
EI	flexural rigidity
f	focus length
g	standard acceleration of gravity
$g(r)$	radial distribution function
G^*	complex modulus
G'	storage modulus
G''	loss modulus
h	film height
I	intensity
J	creep compliance
k_B	Boltzmann constant
k_H	Huggins constant
L	loading of micelles with gold salt
l_c	contour length
l_p	persistence length
M	molar mass
p	relative position within the PCC
p	phagocytotic rate
R_g	radius of gyration
r_G	center of mass
r_i	distance between monomers in a polymer
R_m	radius of motion of a tracer particle in MR
r_{mean}	center of the track
t	thickness of PCC
T	temperature in Kelvin
$t_{1/2}$	halfmaximal phagocytotic activity
U	retraction velocity
V	volume
vc	Voronoi cell

Chapter 1

Introduction

Biological systems such as cells are a fascinating assembly of a huge variety of chemical reactions. Interference of the different processes, such as enzymatic digestion of proteins on one side and protein translation on the other side, is ensured by compartmentalization with lipid membranes. These membranes inside the cell do not only function as barriers between the different organelles, but also regulate transport processes between the different compartments and serve as a support for many proteins. Membrane bound proteins function as receptors transducing signals between the two sides, or they enhance the transport of specific materials with active or passive transport channels. Membranes also help to accumulate proteins, as for example in mitochondria, where the proteins required for the oxidative phosphorylation and the adenosine triphosphate (ATP) synthase are bound to the inner membrane [1].

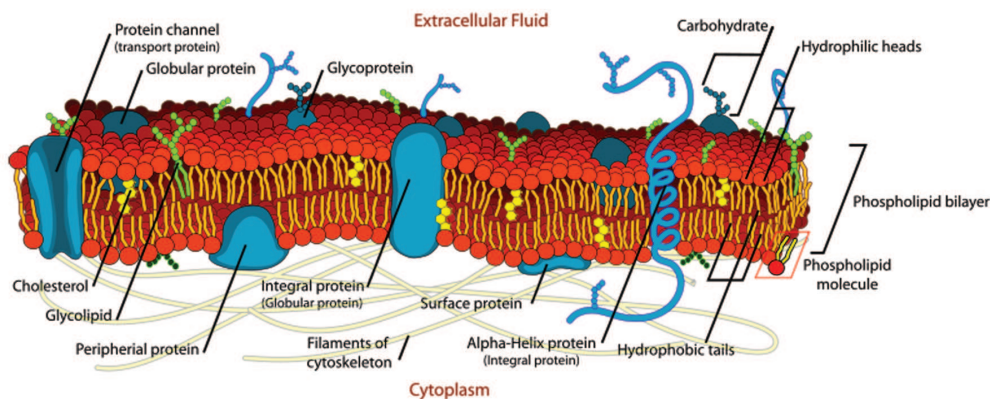


Fig. 1.1 – Schematic drawing of a cell membrane: The outer cell membrane of mammalian cells is a very diverse and dynamic system. The basic structure is given by the phospholipid bilayer consisting of different types of lipids. Incorporated into the bilayer are different proteins that can interact and govern interactions between the cell and its environment. Additionally, short branched carbohydrates cover the outer side of the membrane either covalently linked to proteins or lipids. Image courtesy by *Mariana Ruiz Villarreal*.

The outer cell membrane (fig. 1.1) presents a special lipid membrane, as it governs all interactions between the cell and its environment [1]. It is involved in the transport of materials into and out of the cell, in the communication with other cells and the survey of the cell's environment. Most of these interactions are governed by proteins incorporated into the phospholipid bilayer. Furthermore, they are influenced by the branched and chemically diverse carbohydrates covalently bound to proteins and lipids on the outer side of the cell membrane, sometimes referred to as glycocalix [2, 3].

In contrast to our perception of any living organism, their very basic components, the cells, are very soft objects: They can quickly adjust their shape, enabling for example red blood cells to squeeze through narrow capillaries. The cell's structural integrity is based on its cytoskeleton: An actin network inside the outer cell membrane, the so called actin cortex, stabilizes the cell membrane. Additionally intermediate filaments, microtubules and actin stress fibers strengthen the structure of the cell. Compared to large scale human engineering, these architectural structures are 'soft' in some respect. This is partially due to their small size in at least one dimension. Consequently, they are affected by thermal motion leading to oscillation and undulation of soft sheets and filaments. Thus the small size scale of this composite system helps the cell to adjust its structure dynamically. Especially in extreme situation like cell growth or division [4].

In tissues, cells are embedded in an extracellular matrix (ECM) constituting of components secreted by the cells. This load bearing matrix serves many functions, such as providing support and anchorage for cells, segregating tissues from one another and regulating intercellular communication [1]. Most mammalian cells are additionally enveloped by a pericellular coat (PCC) of non-covalently attached carbohydrates and proteins [5]. The function of this intermediate layer is not fully understood yet, partially due to its ill defined structure.

The PCC is scaffolded by hyaluronan (HA, chapter 1.2.1), a unique polysaccharide. This micrometer long polymer is synthesised directly on the outer cell membrane. In contrast to other glycosaminoglycans, HA is not chemically modified *in vivo*. It serves as a polyvalent template [6] for a multitude of hyaluronan-binding proteins, so-called hyaladherins (chapter 1.2.2). Transmembrane hyaladherins even act as receptors to graft the PCC to the cell membrane and mediate interactions to the cytoskeleton (chapter 1.2.2).

The resulting PCC, also referred to as pericellular matrix (PCM) or glycocalix plays a vital biological role (chapter 1.1). Its size varies considerably depending on the type of tissue: The glycocalix on monocytes is only 10-20 nm thick [7], whereas the thickness of the PCC is about half a micron on endothelial cells [8] and several micrometers on oocytes and chondrocytes [9].

Generally, the structure and the dynamics of the PCC are governed by HA's polyvalent interactions and its polymer physics which can be further modulated by other PCC components. In the following section, first an overview of the biological relevance of the PCC (chapter 1.1) is given and then a detailed description of its composition (chapter 1.2) will follow.

1.1 Biological Relevance of the PCC

The PCC not only forms a passive lubricating layer around the cell, it also plays an important active role in many biological processes [10]. It has been linked to the regulation of cell-cell adhesion [11, 12], migration [13–16] differentiation [17, 18] and proliferation [19, 20]. Hyaluronan also plays an important role in embryogenesis [10] and tumor invasions [21, 22].

The PCC is ubiquitous in mammalian cells and has thus been reported for a mul-

titude of different cell types such as chondrocytes [23, 24], epithelial cells [22, 23], fibrosarcoma cells [25], fibroblasts [18, 26], leukocytes [27], smooth muscle cells [9, 28], and some endothelial cells [27].

The PCC varies in size from a layer of a few nanometer on epithelial cells for example to micrometer thick coats on chondrocytes. Additionally, special HA structures can be observed during inflammation, or in reaction to other various stimuli. Under these circumstances, massive cable-like structures of hyaluronan are observed (fig. 1.2) with unique leukocyte-binding properties [29–32]. These cables often link several cells to each other to form extremely large cables, which have been reported to even span an entire coverslip [9]. These cables are proposed to be a crosslinked form of HA leading to the enhanced mechanical stability of these cables [31].

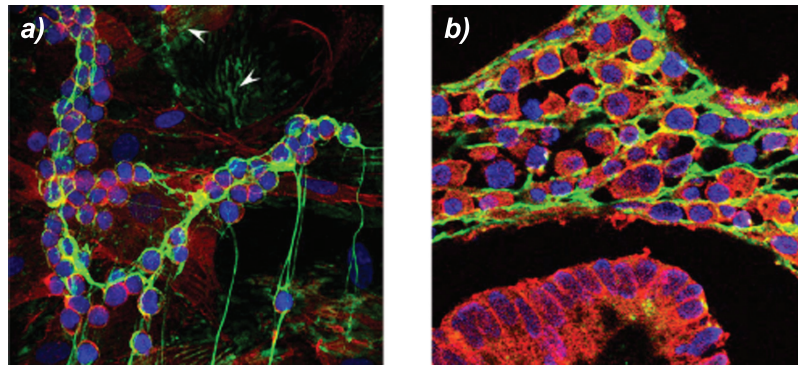


Fig. 1.2 – During inflammation HA cables can be formed: a) HA cables bind monocytes around smooth muscle cells from treated human colon; b) section from an inflamed region of colon from a Crohn's patient. Both samples were stained for HA (green), CD44 (red) and nuclei (blue). Reproduced from fig. 3 and 7 [29].

HA plays an important role in many fundamental biological processes. However, the overall scope of PCC's influences in the different tissues or metastatic cells can not be conceived up to now due to the difficulties in characterization.

1.2 Composition of the PCC

The PCC is a highly hydrated layer composed of HA and different proteins that are able to bind to HA, so called hyaladherins. Often it is not very simple to distinguish the intersection between the PCC and the extracellular matrix (ECM) as the cell produces and interacts with components of both layers. Therefore the PCC might also contain ECM components such as fibronectin and collagen.

1.2.1 Hyaluronan

Hyaluronan was first discovered in 1934 by *Meyer* and *Palmer* in the vitreous of the eye [33]. They named it after the greek *hyaloid* (vitreous) and the detected component uronic acid: hyaluronic acid (hyaluronan). The precise chemical structure was solved twenty years later by *Weissman* and *Meyer* [34, 35]. This chemically simple polysaccharide consists of repeating disaccharides of glucuronic acid and N-acetylglucosamine (fig. 1.3). It can be found in many different parts of the mammalian body, where it also forms the vital backbone of the highly hydrated PCC [9].

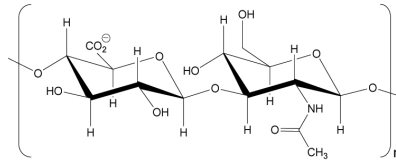


Fig. 1.3 – Chemical structure of hyaluronan (HA): This glycosaminoglycan is unique as it can reach a length of several micrometers, is unbranched and does not get chemically modified *in vivo* as other glycosaminoglycans.

In contrast to all other carbohydrates, hyaluronan is not synthesized in the golgi apparatus of the cell, but by transmembrane proteins incorporated in the outer cell membrane [36]. These HA synthases (HASs) are dual-action glycosyltransferases which catalyze the addition of two different sugars from uridine diphosphate (UDP) linked precursors to the growing HA chain [37]. They catalyse the HA chain elongation at the reducing end in the intracellular space whilst the non-reducing end is extruded through a trans-membrane pore directly into the extracellular space [38,39]. This growth mechanism explains the formation of extremely long polymer chains with contour lengths of several micrometers [40–42]. HA can also stay attached to the synthase. This is one method whereby the HA chain is grafted to the cell membrane (fig. 1.5).

Even though the function of HAS seems to depend on the type of the cell and tissue, certain relations can be assumed. Thus HAS1 maintains a low, basal level of HA, where HAS2 stimulates cell proliferation and angiogenesis [43] and is involved in cell motility [14]. HAS3 on the other hand appears to favor the malignant phenotype [22].

Itano *et al.* showed that the three different hyaluronan synthases produce hyaluronan of different lengths [42], where the total length of hyaluronan under physiological conditions reaches a length of 2-25 μm , corresponding to $10^6 - 10^7$ Da or 2000-25000 disaccharides [40].

1.2.2 Hyaladherins

Hyaluronan serves as an anchorpoint for several different proteins simultaneously. These hyaladherins can be divided into three categories by their functions: The anchoring hyaladherins grafting HA to the cell surface, HA stiffening hyaladherins and HA crosslinking hyaladherins.

In contrast to protein-protein interactions, carbohydrate-protein interactions are mostly mediated by very shallow protein binding grooves. This is also the case for HA binding proteins. Most hyaladherins bind to HA via a link module consisting of about 100 amino acids [44], which are folded very similar to the C-type lectin module [45]. Even though the link module itself is well conserved, some proteins interact with HA additionally over N- and C-terminal extensions or two continuous link modules [45]. The specific interaction of the link module itself is formed with an octameric subunits of HA [46]. Thus one HA molecule could bind up to 3000 hyaladherins if they bind via a single link module and are not sterically hindered by one another.

There are different cell surface receptors known for HA. One of the major receptors for HA is CD44 expressed on a variety of cells in different tissues. Additionally, RHAMM (receptor for HA-mediated mobility) has been identified to bind HA at the membrane [27]. However, RHAMM is also found inside the cell, where it stabilizes spindle formation for example [31]. On specialised endothelial cells in the liver, lymph node and spleen, the HA receptor for endocytosis (HARE) additionally binds HA. It also mediates the uptake of HA with coated pits for the systemic clearance of glycosaminoglycans [Harris2007].

The hyaluronan anchoring proteins not only bind HA, they also trigger cell signalling inside the cell. Thus HA binding of CD44 can result in multiple signalling cascades leading to changes in cell migration, proliferation and activity of gene regulation. CD44 is involved in the Rho/Rack signaling cascade which induces changes in the modifications of cytoskeleton proteins [27]. RHAMM on the other hand is involved in the Ras and the ERK signaling pathways and is associated with the cytoskeleton via this route [10].

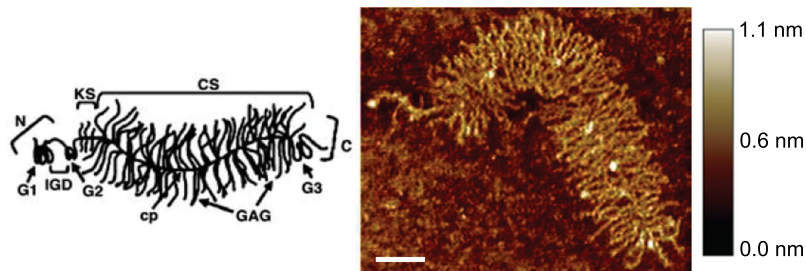


Fig. 1.4 – Aggrecan forms a bottle brush protein: A single aggrecan molecule (schematic - left and AFM image - right) consists of a core protein to which the glycosaminoglycan (GAG) side chains are grafted (cp, core protein; CS, chondroitin sulfate; KS, keratan sulfate; N, N-terminal domain; C, carboxy-terminal domain; G1, globular domain 1; G2, globular domain 2; G3, globular domain 3; and IGD, interglobular domain). Figures reproduced from [47].

A large variety of hyaladherins bind to hyaluronan without anchoring it to the surface or inducing cross-links. Many of these stiffening hyaladherins are tissue specific. Thus neurocan, versican and brevican are mainly found in many tissues, where aggrecan is the prominent hyaladherin found in cartilage. Aggrecan consists of a bottle brush structure (fig. 1.4), in which 100 chondroitin glycosaminoglycan chains and about 60 smaller keratan sulfate oligosaccharides are bound to a core protein of about 130 kDa. With the aid of a link protein, a small hyaladherin, aggrecan associates non-covalently at its G1 domain with high molecular weight HA forming large supramolecular aggregates [48].

Knudson et al. have even been able to form PCCs on fixed chondrocytes *ex vivo* only with hyaluronan and aggrecan [24]. Thus *B. P. Toole* proposed that the structure of the PCC is formed by membrane receptor and HA synthase grafted HA to which proteoglycans like aggrecan are bound to stretch out the hyaluronan (fig. 1.5).

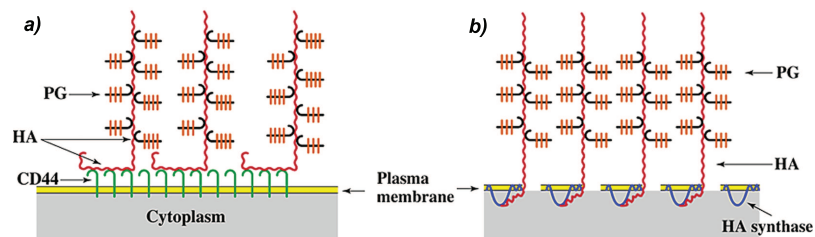


Fig. 1.5 – Possible structure of the PCC: HA is attached to the cell membrane via receptors like CD44 (a) or the HA synthase (b) and proteoglycans (PG) like aggrecan bind to HA. Image courtesy of *B. Toole* as in <http://www.glycoforum.gr.jp/science/hyaluronan/HA08/HA08E.html> and [10].

1.2.3 Model System for the PCC

The most pronounced PCCs can be found on chondrocytes. In their native environment chondrocytes are insulated within the cartilage forming nearly no contacts with other cells or hard tissues [49]. The PCC in combination with the enclosed cell(s) is termed the chondron [49, 50]. This structural entity forms only a fraction of the tissue, but ensures the maintenance of the cartilage to counteract the ongoing abrasion. Therefore, chondrocytes also interface with the cartilage ECM, most importantly with collagen IV and fibronectin [51].

The interplay between the cell, its PCC and the ECM can be studied more closely with adhesion assays on specific substrates. In this way, hyaluronan within the PCC has been identified as an important mediator and modulator in the first interaction steps: hyaluronan coated A6 cells adhere specifically only to the surface of calcium-(*R,R*)-tetratrate tetrahydrate crystals but not to the chiral (*S,S*) counterpart [52]. Additionally, the PCC is reorganized underneath the cell in the early stages of the attachment [53]. These later studies were performed with RCJ-P cells, originated from rat articular cartilage, which serve as a well established model system for extended PCCs [23, 28].

1.3 Passive Microrheology (MR)

The observation of mechanical properties of soft matter is the subject of rheology, the study of flow. If the analysis is performed on smaller length scales important for the possibly inhomogeneous polymer solution or precious sample volumes, various microrheological (MR) tools can be employed [54–57]. These techniques use microscopic probes, which are either actively controlled (active MR) or passively observed (passive MR). The three main subtypes are (1) atomic force microscopy (AFM), (2) active bead manipulation techniques such as magnetic and optical tweezers [58] and (3) passive bead observation methods, such as diffusing wave spectroscopy (DWS) or particle-tracking microrheology (ptMR).

Active microrheological methods are at a disadvantage because they are invasive techniques. The applied force could destroy the structure of fragile soft materials or require long relaxation times for the complete recovery of the sample. In contrast, passive methods are based on the Brownian motion of tracer particles (chapter 1.3.1). The thermal nature of the particle motion ensures that the measured rheological properties are by definition obtained in the linear viscoelastic regime, in which the viscoelastic properties and the microstructure do not change [59].

1.3.1 Brownian Motion

The invention of microscopes enabled the visualization of micrometer sized structures and objects. This led to the fascinating observation, that micrometer sized particles move about in a random, rapid motion in the absence of any apparent force.

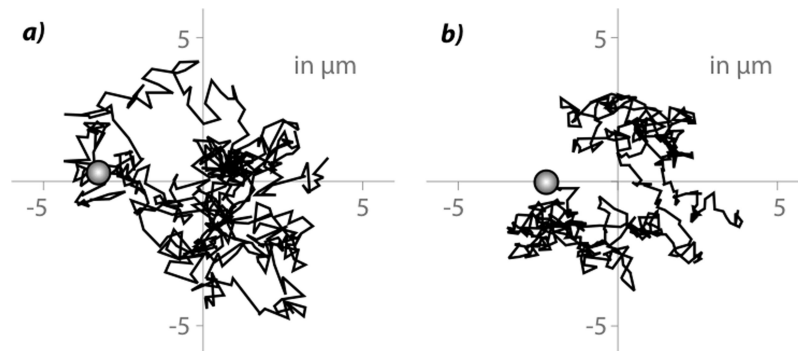


Fig. 1.6 – Micrometer sized particles undergo Brownian motion in viscous solutions: The thermal energy leads to Brownian motion of micrometer sized particles in viscous solutions. The tracks show the typical random walk of $0.75 \mu\text{m}$ polystyrene beads in (a) 20% and (b) 40% glycerin in water solution (start position marked with symbolized bead). The length of the tracks correspond to the motion within 5 s recorded at 100 fps.

The most prominent description of this ‘*rapid oscillatory motion*’ can be found in *Robert Brown’s* papers [60, 61]. He first noticed this motion on pollen grains immersed in water, but then demonstrated this effect also in inorganic matter. Paying careful attention to prevent flow and evaporation he disproved any facile mechanical explanation of the so called Brownian motion [62].

Brownian motion is in fact a result of the thermal energy of the embedding liquid. The thermal energy of the solution leads to the movement of its molecules. Whenever these molecules encounter a suspended particle, they exert a force on this particle resulting in undirected translational and rotational movement of these particles.

Consequently the particles perform a random walk with varying step sizes that are characterized by a Gaussian distribution.

The Brownian motion of polystyrene microspheres (fig. 1.6) shows obvious differences depending on the viscosity of the solution and the diameter of the microsphere: Both a less viscous solution and a smaller particle size lead to faster diffusion. To quantitatively compare the diffusion characteristics of different particles a mathematical description of the diffusion is required. Since the Brownian motion is not a directed, but a random walk, it is characterized only by its step size. Most often the average squared distance x that a particle has moved in a certain lag time τ (the lag time-dependent mean-squared displacement (MSD)) is given:

$$\text{MSD} = \langle \Delta x^2(\tau) \rangle = \langle |x(t - \tau) - x(t)|^2 \rangle_t \quad (1.1)$$

In a purely viscous solution the MSD scales linear with τ and depends on the viscosity of the solution and the shape and size of the particle. *Einstein* and *Smulochowski* both derived independently the relation of the diffusion constant on the thermal energy and the drag coefficient β in 1905. The diffusion coefficient can then be correlated to the MSD.

The diffusion constant for translational motion D is proportional to the thermal energy $k_B T$ and inversely proportional to the drag coefficient β (Einstein relation, 1905):

$$D = \frac{k_B T}{\beta} \quad (1.2)$$

In solutions of low Reynold's numbers the drag coefficient β can be calculated for rigid, spherical object of radius r in a solution with the viscosity η by the Stoke's law (Sir George Gabriel Stokes, 1819-1903):

$$\beta = 6\pi\eta r \quad (1.3)$$

The Stokes-Einstein relation refers to the combination of Stoke's law with the Einstein relation. This calculation of the diffusion coefficient is, as mentioned, only valid for rigid, spherical objects in non-turbulent solutions:

$$D = \frac{k_B T}{6\pi\eta r} \quad (1.4)$$

Correlating the diffusion constant to the experimentally determined MSD in n dimensions allowed *Jean Perrin* to prove *Einstein's* and *Smulochowski's* hypothesis [63]:

$$\text{MSD} = \langle \Delta x^2(\tau) \rangle = 2n \cdot D \cdot \tau \quad (1.5)$$

As the diffusion constant is inversely proportional to the radius of the observed beads, it is important to have very monodisperse microspheres when averaging over several particles. *Perrin* solved this problem in using particles of gutta-percha (natural rubber) that are of a homogenous size of $0.37 \mu\text{m}$ [63].

1.3.2 Viscoelastic Solutions

Ideal fluids, so called Newtonian liquids, are purely viscous. Most real solutions however exhibit additional elastic behavior and are therefore called *viscoelastic*. They are characterized by the complex viscoelastic modulus G^* which consists of the elastic modulus G' and the viscous modulus G'' :

$$G^*(\omega) = G'(\omega) + iG''(\omega) \quad (1.6)$$

Both the viscous and the elastic properties of the complex solution affect the particle's Brownian motion. To characterize this combined effect it is instructive to first understand both extremes. The Brownian motion in a purely viscous fluid was described in the previous section. In a purely elastic material, particles deform the embedding material when they move over a certain distance. This amount of applied energy remains stored in the system. Consequently, the system exerts a force onto the particle, pushing it back to its original equilibrium position. The displacement achievable by the particle is limited in its ability to deform the material which depends on its thermal energy and the elastic modulus G' :

$$\langle \Delta x^2(\tau) \rangle_{\tau \rightarrow \infty} = \frac{2n \cdot k_B T}{6\pi r G'} \quad (1.7)$$

The Brownian motion of particles in a viscoelastic solution reflects both the viscous and the elastic contribution of the material. The complex viscous and elastic behavior results in a frequency dependent step size of the particles. Thus the MSD does not scale linear as in viscous solutions, but follows a scaling law with the diffusive exponent α :

$$\text{MSD} = \langle \Delta x^2(\tau) \rangle = 2n \cdot D \cdot \tau^\alpha \quad (1.8)$$

This formula still represents the purely viscous solution for $\alpha = 1$, but also includes subdiffusive motion for $0 < \alpha < 1$, observed in viscoelastic material, superdiffusive motion for $\alpha > 1$, found in active transport processes, and local constrains for $\alpha = 0$.

Maxwell Model

In the mechanical circuit representation viscoelastic fluids are described by the Maxwell model (figure 1.7): A linear combination of a spring and a dashpot. The elastic spring

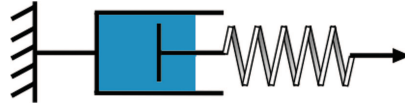


Fig. 1.7 – The Maxwell model of viscoelastic solutions is a linear combination of a dashpot with a spring. The damping factor of the dashpot represents the viscosity and the spring constant the elasticity of the viscoelastic solution.

corresponds to the elastic deformation. Its spring constant is proportional to $G'r$. After deformation of the spring the energy remains stored within the system. Therefore the elastic modulus G' is also called the storage modulus. The dashpot introduces the viscous behavior of the solution. Its damping factor corresponds to the viscosity of the solution. In the viscous dashpot the energy of the applied force is dissipated. The viscous modulus G'' is therefore termed the loss modulus. The thermal force applied to the system will cause an effect on both the elastic spring as well as the viscous dashpot.

Generalized Stokes-Einstein relation (GSER)

The MSD exactly resembles the viscoelastic properties of the probed solution. If the solutions' mechanical properties are changed, e.g. through free-radical photopolymerization, these changes can most exactly be followed by comparison of the respective MSD [64]. To compare the microrheological results to literature values or bulk rheometer results it would be favorable to convert the MSD into a standard rheological measure. It can be directly converted into the creep compliance $J(\tau)$ [65] which is independent of the bead's diameter r and therefore allows to compare MSD values obtained with differently sized particles:

$$\langle \Delta x^2(\tau) \rangle = \frac{k_B T}{\pi r} J(\tau) \quad (1.9)$$

In the biophysical and soft-matter community, in which the microrheology was developed the loss and storage moduli are most often used to describe viscoelastic material. Since the Stokes-Einstein relation is not valid for viscoelastic solutions, a generalized Stokes-Einstein relation (GSER) has been formulated for the motion of spherical particles in homogeneous, incompressible viscoelastic fluids [66,67]. It relates the time dependent MSD to the frequency dependent loss G'' and storage G' moduli [68,69]:

$$G'(\omega) = G(\omega) \cos[\pi\alpha(1/\tau)/2] \quad (1.10)$$

$$G''(\omega) = G(\omega) \sin[\pi\alpha(1/\tau)/2] \quad (1.11)$$

$$G(\omega) = k_B T / [\pi r \langle MSD(1/\tau) \Gamma[1 + \alpha(1/\tau)] \rangle] \quad (1.12)$$

1.3.3 Inhomogeneities

One great advantage of microrheology is the small sample size which is required for the experimental setup. Moreover, inhomogeneities can be measured, which is especially true for passive microrheology. In passive microrheology no artefacts can be introduced through applied forces and the results are therefore always within the linear viscoelastic regime.

The measured MSD depends on the size of the probe. If the microspheres are smaller than the typical meshsize ξ of a given network ($r < \xi$), they can diffuse through the meshes and will be influenced less by the elastic net. If the mesh sizes vary considerably, the bead might get trapped in an area surrounded by smaller meshes ($r \approx \xi$) and if the bead is larger than the mesh size ($r > \xi$) bulk properties will be measured. Caging effects can be detected in the x,y-trajectories of the particle motion (fig. 1.8) as shown by *Wong et al.* [70].

Performing the same set of measurements with different sizes of beads should lead to the anticipated linear dependence on the bead radius, if the bead is larger than the mesh size.

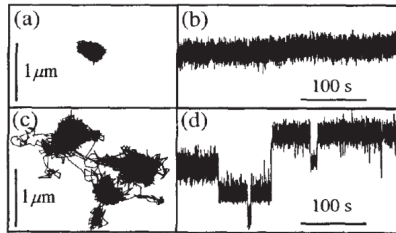


Fig. 1.8 – a) shows a caged bead, c) transitions between different cages. The one-dimensional trajectories (b and d) show the transitions even more obviously. Figure reproduced from fig. 2 in [70].

1.3.4 Microrheology on Biological Samples

In recent years, especially passive particle tracking microrheology has proven very helpful for the study of biological systems. In the beginning mainly actin solutions with different concentrations, length and complements were studied [65,71,72]. Until then, many other biomimetic systems, like high concentrated DNA solutions mimicking the

nucleus [73] or cell extracted intermediate filaments [74] and aggrecan-hyaluronan systems have been successfully studied. The technique has even been applied inside living cells [75].

Chapter 2

Visualizing the Dynamic PCC

The pericellular coat (PCC) consists mainly of water. Only a very low fraction is formed of highly hydrated hyaluronan (HA) and often also hydrated hyaladherins. Thus it remains invisible in all light microscopy techniques. The PCC's indirect visualization can be achieved in a particle exclusion assay (PEA), in which particles form a closed packed layer on the surface excluding the area of the cell and its PCC. Only recently, specific HA staining methods have been developed, which enable the visualization of the PCC on living cells.

The successful purification of GFPn (an eGFP labeled hyaluronan-binding link module) enables a detailed study of the molecular architecture of the PCC. It binds specifically to HA and does not induce changes in the structure of the PCC. Thus this method is ideally suited to analyze the distribution of HA within the PCC and to study very thin PCCs, invisible in a PEA.

Observation of RCJ-P cells with PEA or GFPn staining clearly shows, that the PCC can be adjusted dynamically. Correlation of strong actin stress fibers on cell protrusions and GFPn stained PCCs indicate, that the PCC is rearranged during motility, where exploring protrusions are surrounded by significantly smaller PCCs. HA also plays an important role in proliferation, where it is accumulated at the cleavage furrow to ease the separation of the two new formed cells. If the cells are surrounded by particles larger than $3\ \mu\text{m}$, the PCC is dynamically adjusted to enable their uptake. This time dependent process is related to the size of the particles and can be accelerated by removal of the PCC.

2.1 Particle Exclusion Assay (PEA)

Light microscopy is a well suited method to visualize cell membranes due to the lipid's diffraction of light. The refractive index of the cell membrane differs from the surrounding media and the cytosol. Improved visualization of cells can thus be achieved by phase contrast or differential interference contrast (DIC) microscopy. However, the tremendously high degree of hydration and in-sufficient accumulation of any proteins or lipids anywhere within the pericellular coat (PCC) neither leads to diffraction nor to refraction of light. Therefore, the PCC remains invisible in all bright field microscopy techniques.

Even though the PCC cannot be observed with standard microscopy techniques, it can be visualized indirectly. Large particles, like red blood cells (erythrocytes) are not able to penetrate the PCC. If they are added in large amounts to the cell sample, they form a uniform monolayer on the surface. Around each cell a halo can be observed occupied by the excluded volume of the PCC (fig. 2.1). This visualization method is thus called a particle exclusion assay (PEA).

The introduction of the PEA in 1968 triggered the detailed investigation of the PCC. PEAs proved that mammalian cells were surrounded by a pericellular 'zone' even *in vitro* [5] and showed that the PCC can be reconstituted on fixed cells with hyaluronan and aggrecan [24]. Recently, a PEA based on silica particles was successfully applied to show that RCJ-P cells are enveloped by a PCC on all non-adherent membranes, including the apical side of the cell [28].

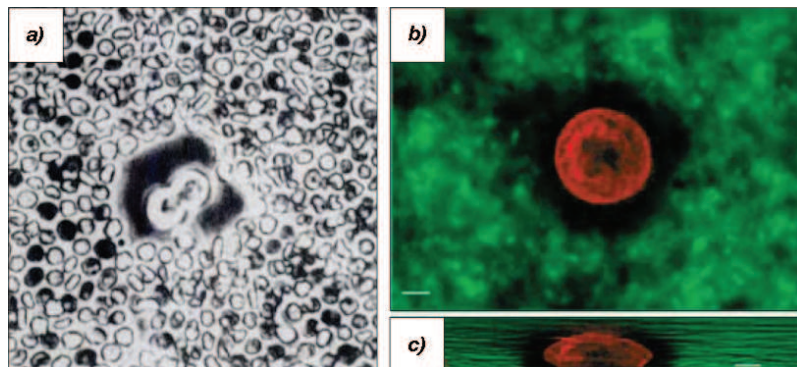


Fig. 2.1 – Particle exclusion assays (PEA) with: (a) fixed erythrocytes on embryonic chick chondrocytes, adapted from [24]. b) PEA with $0.4 \mu\text{m}$ FITC labeled silica beads on rhodamine labeled RCJ-P chondrocytes, adapted from [28]. c) Deconvoluted and reconstituted image along the z axes of (b). The scale bars correspond to $5 \mu\text{m}$.

2.1.1 PEAs Enable the Indirect Visualization of the PCC

Traditionally only erythrocytes are employed in PEAs even though they can generally be performed with any micrometer sized particle large enough to be excluded by the PCC. However, non-passivated beads are immediately coated by serum proteins and can subsequently be taken up by the cells (see chapter 2.4.3). Additionally, particles with a diameter of less than $5 \mu\text{m}$ are able to diffuse into the PCC. About 10 min after the beads have settled on the surface, the clear detection of the coat's edge on adhered cells is obscured. Another problem posed by this type of PEA is electrostatic fixation of beads at the glass surface. This method is therefore not suited to record time series of moving cells or the dynamics of the PCC.

Erythrocytes on the other hand are excluded nicely by the volume taken up by the cell and its PCC. They are not phagocytosed by healthy cells even over time periods of several hours and do not bind to the glass surface. Therefore, they are very well suited to characterize the pericellular coat (fig. 2.2).

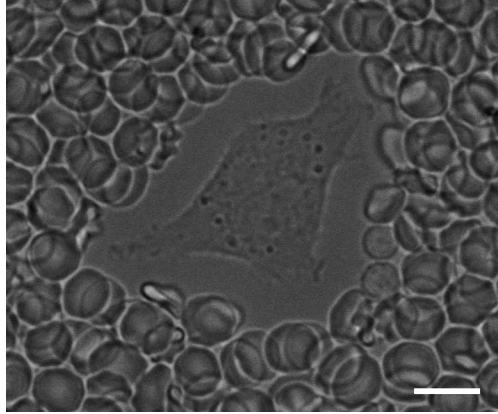


Fig. 2.2 – Red blood cells are ideally suited to visualize the PCC by PEA: The erythrocytes were added to adhered RCJ-P cells forming a monolayer around the PCC, in which the single blood cells are able to move around freely. The cell and its PCC are imaged in bright field microscopy, scale bar corresponds to 10 μm .

A three dimensional characterization of the PCC can be achieved with a multilayer of red blood cells, partially resting on top of the coat. In standard bright field microscopy the thickness of the coat can be estimated by the visibility of these erythrocytes appearing further out of focus. The exact three dimensional shape can be retrieved with fluorescently stained red blood cells imaged in confocal microscopy (chapter 3.1).

2.2 Specific Fluorescent Staining of Hyaluronan

Analysis of the PCC's molecular architecture requires the visualization of its component in their native conformation. As the indirect PEA proves the destruction of the highly hydrous coats after most fixation steps, experiments on living cells seem most promising. Therefore an HA specific fluorescent marker applicable to living cells is required to gain further insights into the internal structure, the dynamics and the three dimensional organization of the coat. In order to study the distribution of HA by fluorescent labeling, the dye's interaction with HA should not change the fragile structure of the PCC. Thus the marker must not induce cross-links between different HA chains and has to be small enough to prevent stretching of the HA chains (compare chapter 1.2.2).

Based on the work by *Zhang et al.* [76], I developed a purification method for GFPn (chapter 5.3.7) and controlled its specificity and possible impacts on the thickness of the PCC (chapter 2.2.2). Subsequently, we compared the PCC of different cell types (chapter 2.2.3) and analyzed the distribution of hyaluronan within the PCC of RCJ-P cells (chapter 3).

2.2.1 Current Status of HA Staining Methods

One method for the fluorescent staining of the PCC has been successfully applied by *Cohen et al.* to visualize the role of the PCC during initial adhesion [23]. They first incubated the cells with biotinylated hyaluronan-binding protein (bHABP) and subsequently added streptavidin-conjugated quantum dots (QD). One draw-back of this method is the relatively high concentration of applied bHABP (5 mg/ml) that might change the structure of the coat. This effect is possibly enhanced by the addition of QDs which induce crosslinks, if one QD is bound to several hyaluronan chains.

A totally different approach was taken by *Evanko et al.* [19]. They labelled HA first with a fluorescent dye which enabled to follow its interaction and uptake by the cell.

Very recently, a new specific HA labeling probe has been introduced by the group of *M. Tamm* (University of Kuopio, Finland) based on the unspecific attachment of activated AlexaFluor594 to the hyaluronan binding complex [21]. This probe does not require the addition of fluorescently labeled streptavidin molecules, which also tend to induce cross-linking with its four biotin binding sites. Thus this probe is also ideally suited to study the distribution of HA. The statistic linkage to the dye might however lead to its attachment in or close to the HA-binding pocket resulting in a reduced HA affinity of some probe molecules.

The link module eGFP fusion protein (abbreviated as GFPn) used in this thesis has been introduced by *Zhang et al.* in 2004 [76]. It consists of the neurocan link module labeled specifically with the enhanced green fluorescent protein (eGFP, [77]). GFPn thus binds specifically to a hexameric or octameric subunit of hyaluronan [76]. *Zhang et al.* proved the applicability of GFPn in affinity histochemical stainings of mouse eye sections. They were also able to take time-lapse movies of single cells to which the unpurified GFPn had been added. These cells showed the formation of distinct fluorescent patches on the outside of the cell membrane which were redistributed over time.

Construction of the eGFP Labeled Link Module GFPn

GFPn consists of three parts: the hyaluronan binding domain, a fluorescent marker and a purification tag (fig. 2.3) [76]. The sequence of the hyaluronan binding domain is taken from the link module of the hyaladherin neurocan, corresponding to the primary

structure of aspartic acid 23 to histidine 359 of neurocan. On the histidine side an eGFP serves as fluorescent marker with a bright fluorescent peak at 510 nm. Six histidines (his), bound via a linker to the aspartic acid end of the link module, form a His-tag which enables the affinity chromatography based purification.

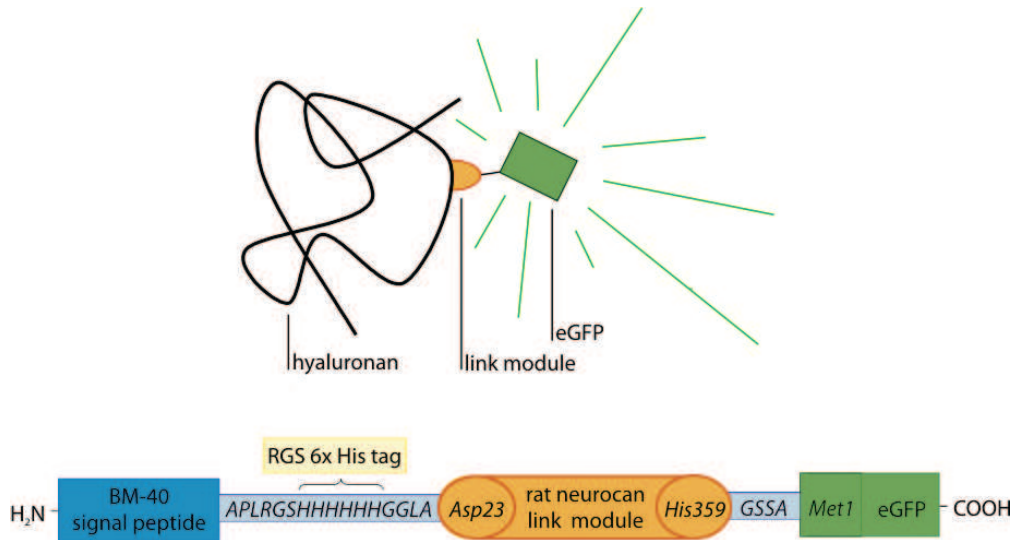


Fig. 2.3 – GFPn binds specifically to a hyaluronan subunit with the hyaluronan binding link module (orange). It further consists of the eGFP (green) attached to the histidine (his) end of the link module and the 6x His-tag (light orange) bound to the aspartic acid (Asp) end, used for purification. The BM-40 signal peptide (dark blue) directs the GFPn to the secretory pathway and is removed before the secretion.

The GFPn is produced in mammalian cells to ensure proper posttranscriptional modifications. *Zhang et al.* therefore constructed an episomal expression plasmid that was successfully introduced into HEK 293 EBNA cells. The BM-40 signal peptide attached to the his tag, directs the protein towards the secretory pathway and ensures its secretion into the media before it is removed by the cell.

2.2.2 Staining the PCC of Living Cells with GFPn

Hyaluronan within the PCC of RCJ-P cells is successfully stained by addition of GFPn to the growth media in an approximate dilution of 1:100. The GFPn is accumulated close to the cells leading to fluorescent halos around the cells corresponding to the excluded areas in particle exclusion assays (fig 2.4).

Specificity of GFPn to hyaluronan was tested by hyaluronidase treatment of the cell prior to the GFPn incubation. This enzyme digests hyaluronan and thus removes the coat without further harming the cells. As expected, no fluorescent staining was observed after such a treatment.

One hour after incubation with GFPn containing growth media, a small rim of fluorescence could be seen around the cells and the PEA also suggests a backgrowth of the PCC. However, if the cells were first incubated with GFPn and hyaluronidase was added afterwards, the coat could not be removed. Considering, that the GFPn binds to all accessible hyaluronan parts it would be consistent, that it thus protects the hyaluronan from enzymatic digestion.

In order to quantify the structural changes induced by the GFPn attachment we

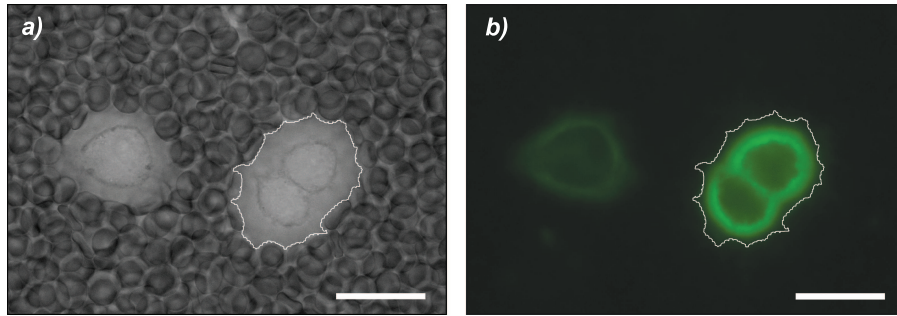


Fig. 2.4 – The PCC of living RCJ-P cells can be stained with GFPn. a) The extend of fluorescent staining observed on a fluorescent microscope corresponds well to the excluded area of the particle exclusion assay (b). The scale bars correspond to 10 μm .

measured the PCC in the absence and presence of GFPn and found no significant differences on cells that had been adhering to glass surfaces for 6 and 12 h.

2.2.3 Visibility of Very Thin PCCs with GFPn Stainings

The fluorescent staining of hyaluronan should be much more sensitive to PCCs than a PEA. Thus it is ideally suited to study the PCC of different cell types, whose PCC size ranges from a few micrometers to very thin layers of below one micrometer.

Primary human chondrocytes from the hip

The observed primary human chondrocytes (HCH) did not seem to possess a PCC, as no halo was visible in PEA experiments 6 h after seeding. However even 30 min after seeding specific fluorescent staining could be observed on most HCH cells (fig. 2.5). On many cells the PCC was not as homogenous as on the RCJ-P cells, but showed interesting, dynamic structures, that were often only visible at the rim of the cell without extending outwards (fig. 2.6).

Primary cells that have been allowed to adhere for longer times to the glass surfaces often form long filopodia of up to 100 μm , which are detected best in GFPn stained images, as they are covered with HA (fig. 2.7).

PCC on other cell lines

Chondrocytes are by far not the only type of cells reported to be enveloped by a HA-rich coat (compare chapter 1.1). For comparative measurements I tested other cell lines for HA-rich PCCs. None of the tested cell lines seemed to have any PCC in the PEA. However GFPn staining revealed HA-rich coats of different sizes, that were not visible after hyaluronidase treatment (table 2.1).

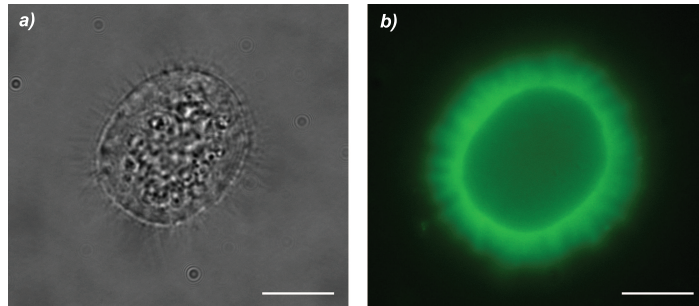


Fig. 2.5 – Primary human chondrocytes (HCH) sometimes show pronounced PCCs: a) Small filopodia are recognizable in bright field microscopy. b) GFPn staining shows the presence of hyaluronan even 30 min after splitting in standard fluorescent microscopy. The scale bars correspond to 10 μm .

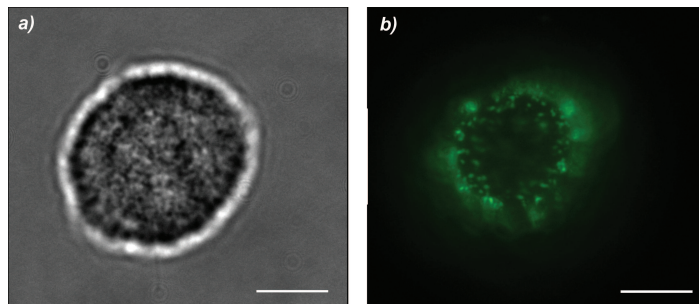


Fig. 2.6 – HCH cells often show a dynamic structure especially on very thin PCCs. a) Bright field image 30 min after seeding. b) Corresponding image in standard fluorescent microscopy. The scale bars correspond to 10 μm .

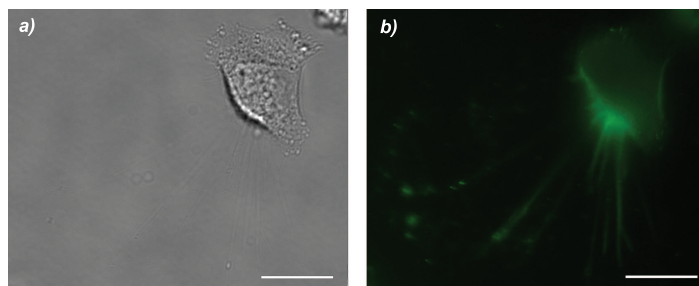


Fig. 2.7 – After 6 h of adhesion, HCH cell often form long filopodia, which are covered with hyaluronan, as they are colocalized with the GFPn staining. The scale bars of the bright field image (a) and the fluorescent image (b) correspond to 20 μm .

Table 2.1 – Other cell lines also have a hyaluronan-rich PCC: I tested different other cell lines after an adhesion time of 6 h with GFPn in standard fluorescent microscopy, whereas the cells listed below, showed some specific staining.

cell type	short description	observed staining
HeLa	an immortal cell line derived from cervical cancer cells taken from <i>Henrietta Lacks</i>	small inhomogenous fluorescent rim
2F9	neuronal cells	fluorescent rim on some cells
REF 52 WT	rat embryo fibroblasts; most common cells of the connective tissue	strong staining of a thin layer around the cell

2.3 Standard Cell Culture Procedures Influence the Size of the PCC

The pericellular coat may be influenced by trypsination of the cells, adhesion times or flow, e.g. arising during washing procedures. Before any further measurements of the PCC can be performed these effects need to be well characterized.

RCJ-P cells are an adherend cell line. In order to detach them from the culture fasks, they are incubated in a trypsin solution. This serine protease is originally found in the digestive system, where it breaks down proteins. Its protease activity is also employed in standard in cell culture techniques. As trypsin digests extracellular proteins and transmembrane proteins unspecifically, it is no surprise, that the PCC is significantly altered after trypsination with PCC's ranging from a not detectable thickness to values of several micrometers. The cells start to regrow their PCCs right after seeding on fresh surfaces. Four hours later the average thickness of the PCC in the sample is constant, if cells are allowed to adhere to untreated glass surfaces. Therefore most experiments were performed at least 6 h after seeding.

The same effect can also be observed after hyaluronidase treatment. If the media is replaced after the described treatment the PCC is grown back within 4 h, whereas the first halos in PEAs can be observed 1 h after the treatment. If hyaluronidase is left in the solution, the PCC starts to grow back after three hours, possibly due to inactivation of hyaluronidase by this time.

Another maior concern is flow induced changes, which might occur during rinsing procedures. Therefore the PCC has been measured in a special flow cell in which the solution is flushed with media at a rate of about 10 mm/s over 5 min. A comparison of the PEA before and after the experiment showed the same PCC thickness, thus rinsing does not affect the PCC.

Cell culture conditions significantly affect the size of the PCC. Especially the composition (batch) and amount of fetal bovine serum (FBS) dramatically affects the size of the PCC. Additionally, the type of media has an impact on the cell size, which is not as pronounced, but visible in the comparative measurement of the same cell batch 5.5 h after seeding (table 5.1).

Table 2.2 – PCC thickness averaged over 50 cells after 5.5 h. The difference to the CO₂ independent medium was sagnificant, as tested by a student t-test.

media	PCC thickness
α -MEM	6.3 ± 1.1
α -MEM with 0.25 M HEPES	6.4 ± 2.1
CO ₂ independent medium	5.7 ± 1.3

2.4 Dynamics of the PCC

The thickness of the PCC, as determined in the PEA, does not show absolute uniformity around the cell. Large alterations can especially be observed on cell protrusions. Similarly, cell protrusions are often partially hidden in PEA images due to their thinner coats (fig. 2.8). These altered PCC sizes on cell protrusions might be linked to the motion of the cell (chapter 2.4.3).

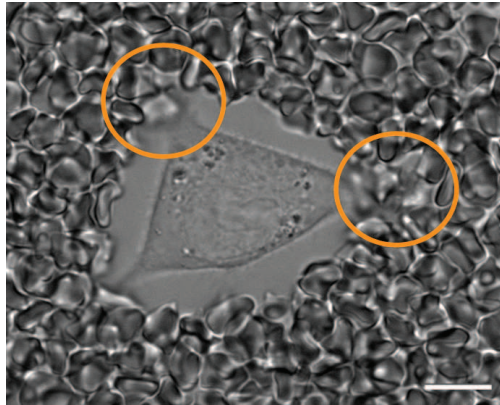


Fig. 2.8 – Cell protrusions are often partially hidden in PEA experiments due to their thin coat. The thickness of the coat varies on different areas of the cell. Often it appears thinner on membrane protrusions as seen in this bright field image (orange circles) on this cell 6 h after seeding. The scale bar corresponds to 10 μm .

Observation of RCJ-P cells with PEA or GFPn staining over time clearly shows, that the PCC is no static structure. It can be adjusted dynamically during processes like cell division, motility or phagocytosis. All of these processes are tightly linked to the dynamics of the cytoskeleton, especially the actin network.

Therefore we transfected RCJ-P cells with mCherry labeled actin to visualize the correlation of actin stress fibers, or contractile ring formation with the morphology of the PCC. Transfected cells produce labeled actin in addition to their normal actin. Both monomers are incorporated into the actin structures of the cell, such as the stress fibers and the actin cortex leading to a fluorescent labeling of all actin structures (chapter 2.4.1). Correlation of strong stress fiber formation on cell protrusions and GFPn stained PCCs indicate, that the PCC is rearranged during motility, where exploring protrusions are surrounded by significantly smaller PCCs (chapter 2.4.1). During division the PCC is accumulated in the cleavage furrow (chapter 2.4.2) and during phagocytosis the PCC is dynamically adjusted in a time and particle size dependent process to enable the uptake of particles larger than one micrometer (chapter 2.4.3).

2.4.1 The PCC is Rearranged During Motility

The successfully transfected RCJ-P cells were co-stained with GFPn allowing the visualization of the actin cytoskeleton and the PCC simultaneously. The pericellular coat shows a non-homogenous staining increasing towards the cell membrane with different thicknesses around the cell (fig. 2.9 - see chapter 3). The actin staining nicely shows extending adherent protrusions that hover above the surface. The strong stress fiber formation at cell protrusions indicates strong adhesion to the surface in these specific areas. The regions with stress fibers are often correlated with very thin or invisible PCCs. Often these protrusions are moving around in the time scale of minutes or are

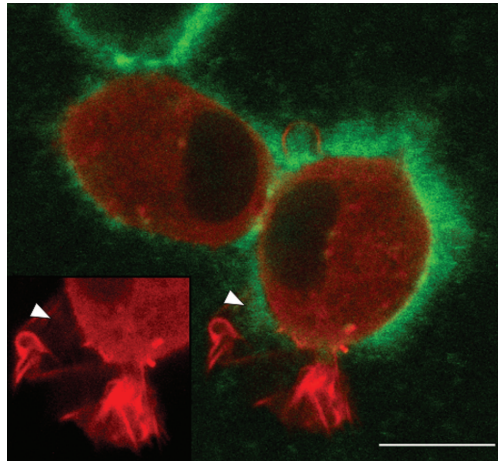


Fig. 2.9 – Strong stress fiber formation at cell protrusions are often not enveloped by the PCC: Confocal image of RCJ-P cells transfected with mCherry actin (red) and GFPn marked PCC (green) about 6 h after transfer to new media. The third cell partially seen at the top has not been successfully transfected, therefore only the PCC is visible. The PCC coat varies in thickness and intensity without surrounding the cell completely. Arrow: As observed, especially when compared to the actin staining in the inset, the cell extends an adhering arm from above resting on a cushion of the PCC.

found on the leading edge of the cell in the direction in which the complete cell is moving. Long protrusions partially hovering above the surface often seem to lie on a PCC cushion, as the coat extends beneath these arms up to the area where the stress fiber formation is observed (compare fig. 2.10). This is especially true in cells which lack of time to adhere (up to about 4 hours). Sometimes also a stronger expression of the PCC on the site opposite of the stress fiber formation can be observed (compare fig. 2.9). These observations indicate, a cell controlled decrease of the PCC to explore the environment and to adhere to the surface, whereas an increase of the PCC aids the detachment from the surface.

In order to follow the movement of a cell a better fluorescent staining in means of sustainability over longer periods of time is needed. It is also important to be able to visualize all cells present which is not the case with transfected cells, since transfection rates of 100% are never achieved (compare fig. 2.9 and 2.10). The shape of a cell is closely related to the actin structure within. Thus staining the membrane instead of the actin cytoskeleton still leads to the same information about the general cell morphology.

2.4.2 The PCC Assists Cell Division

Hyaluronan plays an important role during cell division, influencing the detachment from the surface as well as the division process itself [22]. Thus increased HA levels have been observed on dividing cells correlating with a maximum level of HAS isoenzyme activity [78]. However, this does not necessarily lead to enlarged PCC, as HA is also taken up by the cell to assist cell division inside the cell [31]. Intracellular HA has been detected in nucleoli and the nuclear periphery. During mitosis, it tends to accumulate at the mitotic spindle together with the HA receptor RHAMM [79]. Furthermore, an increased PCC promotes cell rounding and detachment on fibroblasts [20] and smooth muscle cells [19] and can even lead to anchorage independent growth in culture of HAS

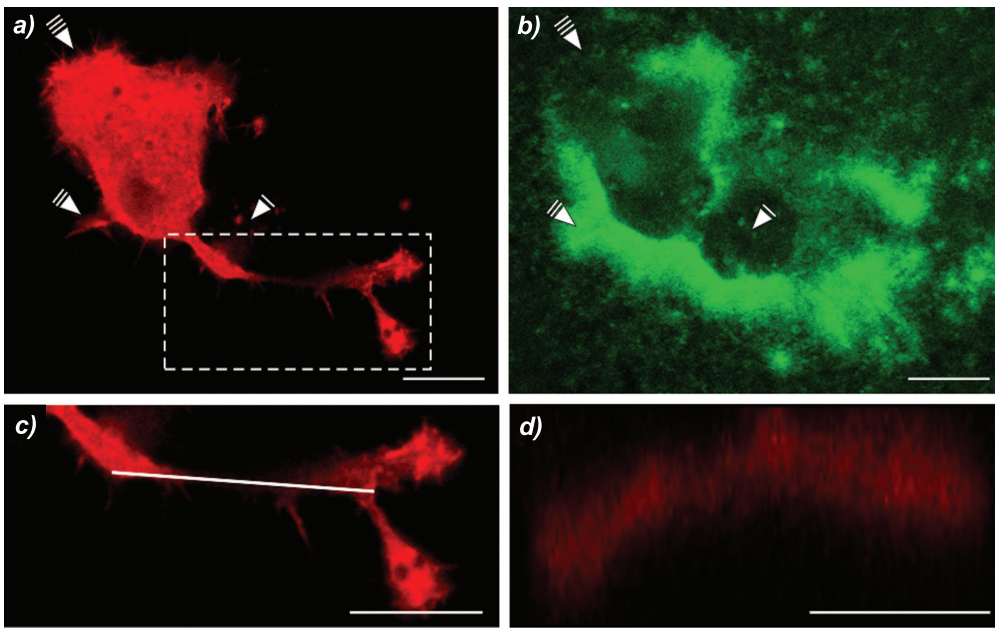


Fig. 2.10 – Colocalization of actin and the PCC: Confocal images of RCJ-P cells transfected with mCherry actin (red, a) and GFPn marked PCC (green, b) about 6 h after transfer to fresh media. In this image one cell is nicely transfected, whereas the other (at arrow 1) does not produce fluorescent actin. The PCC of the transfected cell varies in thickness and intensity and does not surround the cell completely (b). A potential retracting adhesion arm (arrow 2) is surrounded by the pericellular coat while the possible leading edge (arrow 3) is devoid of PCC. c) Close up of the bottom arm outlined in (a). d) Reconstituted image along the white line in (c). For over 10 μm this arm is not adhered to the surface but rests on a pericellular cushion. The complete height of the reconstituted image (d) corresponds to 8.6 μm . The scale bars correspond to 10 μm .

overexpressing fibrosarcoma cells [11]. However, the increase of the PCC during rounding of the cells is hard to judge, as the cell also changes its shape considerably. Thus the overall surface of a round shaped cell is smaller than of an adhered cell. If the cell membrane is not taken up simultaneously, it forms a ruffled structure. Consistently, an increase of microvilli on the surface of dividing cells was observed (fig. 2.11). Counterintuitively, the formation of such microvilli does not require a lot of force due to the fluid-like structure of lipid membranes [80]. Condensed surfaces like that might also lead to a denser packing of the PCC resulting in an enlarged PCC.

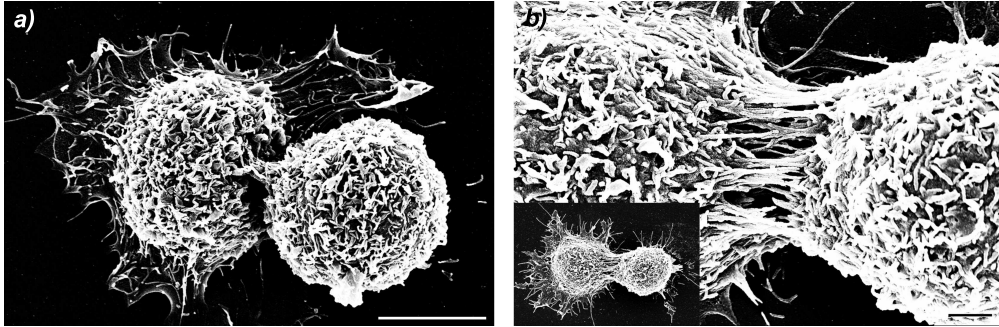


Fig. 2.11 – The cleavage furrow separates the two daughter cells during division: The contractile ring is pulled tight until the cells are pinched off. The scale bar in these SEM images correspond to $10\ \mu\text{m}$ in (a) and $1\ \mu\text{m}$ in (b).

In order to study the arrangement of HA within the PCC during division more closely, GFPn stained RCJ-P cells were observed. As the GFPn dye cannot penetrate the cell membrane, no internal HA were marked. Time series observed in standard fluorescent microscopy indicate an accumulation of HA at the cleavage furrow (fig. 2.12).

At this stage, termed cytokinesis, the chromosomes were already separated into the two future daughter cells and a contractile ring of actin stress fibers containing myosin was established at the prior metaphase plate [1]. The contractile ring was then narrowed down until the cells are pinched off from one another.

The accumulation of PCC can be observed most prominently when the cell has taken on an hourglass structure. At this time point the PCC was accumulated in the cleavage furrow and surrounded it completely (fig. 2.13).

HA might be accumulated in the cleavage furrow through its cell surface receptors. The cytoplasmic domain of the HA receptor CD44 (chapter 1.2.2) interacts with actin-associated ERM proteins (ezrin, radixin, moesin), which have been shown to accumulate in the cleavage furrow as well [81]. These proteins have additionally been linked to the formation of microvilli [82], which might also be involved in the formation of the PCC.

Even though the chromosomes have already been separated at this stage of the division process, the cleavage furrow presents a fragile structure (fig. 2.11), which might be protected by an increased PCC. The PCC could also aid the separation of the two freshly formed cells or serve both purposes simultaneously.

2.4.3 Phagocytosis through the PCC

The PCC forms a natural barrier during phagocytosis. The cells are thus able to initially hinder particles larger than $1\ \mu\text{m}$ from entering the PCC (fig. 2.14) as utilized in the PEA. However, cells do eventually take up particles larger than $1\ \mu\text{m}$ and thus need to change the structure of the PCC. In the following section the characterization of the

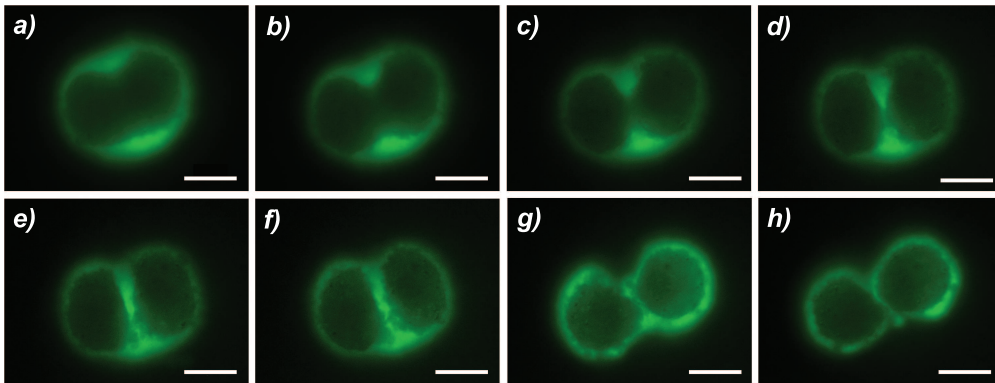


Fig. 2.12 – The PCC is accumulated in the cleavage furrow during division: The GFPn staining of a dividing cell in standard fluorescent microscopy. Images (a) to (e) were taken every 2 min, (e) to (g) after 10 min each. The scale bars correspond to 10 μm .

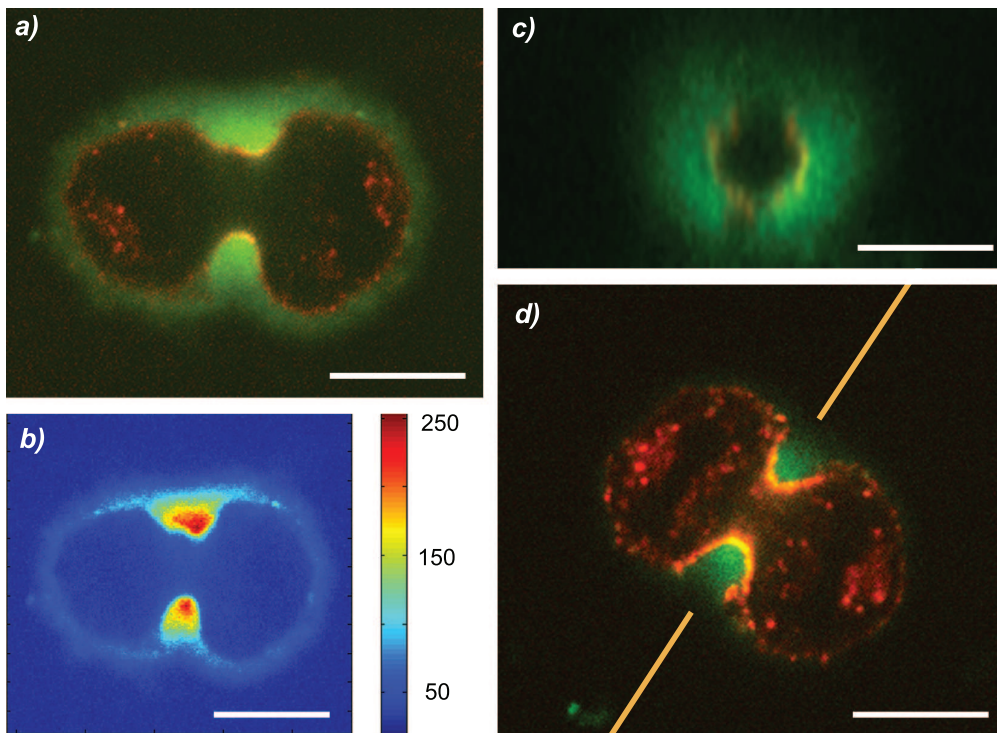


Fig. 2.13 – The PCC is accumulated in the cleavage furrow during division: a) The confocal cut demonstrates the accumulation of PCC in the cleavage furrow. The concentration of HA is dramatically increased in close proximity to the cell membrane within the cleavage furrow: b) false color intensity image of (a). c) The reconstruction of the membrane section with the contractile ring along the orange line of (d), shows that the PCC envelopes the cleavage furrow on all sides. The scale bars correspond to 5 μm .

phagocytotic activity in the presence of different sizes of particles on RCJ-P cells with and without a PCC and the identification of the changes in PCC size (in collaboration with Tabea A. Munding, University Heidelberg and Max-Planck-Institute, Stuttgart) is being presented.

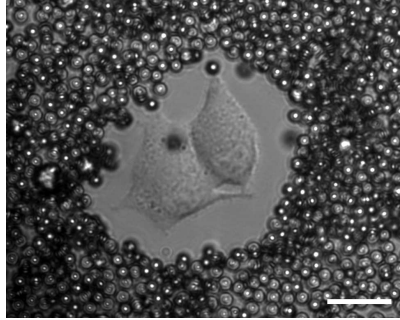


Fig. 2.14 – Particles larger than one micron are initially excluded by the PCC: Here $3.0 \mu\text{m}$ PS beads were added to adhered cells. The image was taken right after settling of the particles. Dark spots within the PCC/cell area are caused by out of focus beads above the cell and its coat. The scale bar corresponds to $20 \mu\text{m}$.

Phagocytotic Rate

In order to characterize the phagocytotic rate of RCJ-P cells, a test series with different sized polystyrene beads ($3.0 \mu\text{m}$, $4.5 \mu\text{m}$ and $6.0 \mu\text{m}$) over time was performed. About the same amount of non-agglomerated beads was added to samples with adhered cells. Subsequently, the number of beads taken up by the cells was counted every hour for at least 60 cells. Phagocytosed beads were discriminated from other beads close to the cell by careful shaking of the sample. As the function of the PCC is no longer important, once a stable cell-bead contact has been established, we counted all stationary beads as taken up.

Interestingly, the cells gathered beads actively moving them with long filopodia without necessarily taking them up. Additionally, beads were caught within the PCC as observed in a simultaneously performed PEA (fig. 2.15). Moreover, the cells did not necessarily tend to phagocytose the beads over a time course of several hours. Both observations indicate that the phagocytotic rate was not limited by the availability of beads in close proximity to the cells.

The phagocytotic rate strongly depends on the size of the presented beads (fig. 2.16a): RCJ-P cells start to phagocytose smaller particles faster than larger ones. Also more cells seem to actively take up smaller particles. The speed of phagocytosis can be determined by an exponential fit characterized by the plateau value p and the time constant t :

$$y = p(1 - e^{-x/t}) \quad (2.1)$$

The plateau value, corresponding to the overall percentage of phagocytotic cells, shows no clear relation to the size of the beads, that were taken up (fig. 2.16). The time constant on the other hand depends on the size of the phagocytosed particles in a linear fashion (fig. 2.16b and table 2.3). Three micron particles are taken up seven times faster than $6.0 \mu\text{m}$ beads and four times faster than $4.5 \mu\text{m}$ beads. The repeated experiments with $6.0 \mu\text{m}$ beads showed a reproducible time constant.

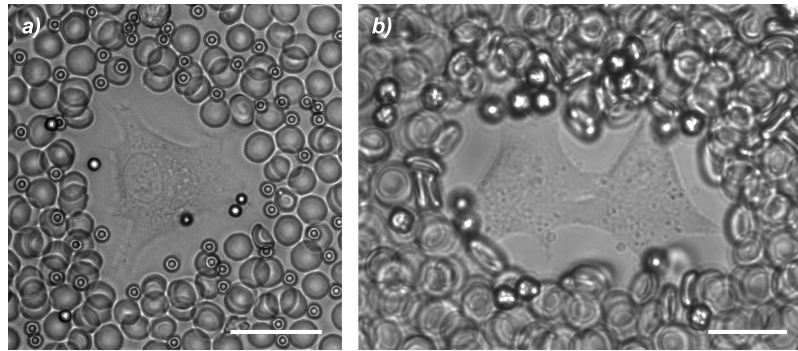


Fig. 2.15 – Gathering of beads around RCJ-P cells: The PEA shows that beads are in close proximity to the cell and even within the PCC. In this example taken 3 h after addition of $3.0 \mu\text{m}$ (a) and $4.5 \mu\text{m}$ beads (b) no beads had been taken up.

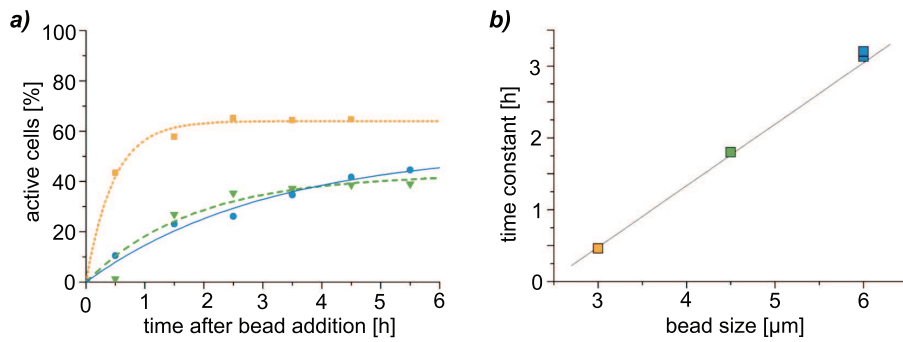


Fig. 2.16 – Phagocytotic activity of RCJ-P cells in the presence of $3.0 \mu\text{m}$ (orange, dotted), $4.5 \mu\text{m}$ (green, dashed) and $6.0 \mu\text{m}$ (blue, solid) beads: a) Percentage of phagocytotic active cells with kinetic fit from eq. 2.4.3. b) The time constant t depends linearly on the size of the uptaken bead.

Table 2.3 – Kinetics of phagocytosis of RCJ-P cells

bead size	p	t [h]	$t_{1/2}$ [h]	t [min]	$t_{1/2}$ [min]
3.00	0.64	0.46	0.32	28	20
4.50	0.43	1.80	1.25	108	75
6.00	0.46	3.13	2.17	188	130
6.00	0.32	3.20	2.22	192	133

The time point at which the halfmaximal phagocytotic activity is reached is ideally suited to compare the different experiments. This characteristic time $t_{1/2}$ is defined as

$$t_{1/2} = t \cdot \ln 2 \quad (2.2)$$

Thus, the differences caused by the size of phagocytosed beads can be compared at the same characteristic phagocytotic activity (table 2.3).

The phagocytotic activity at $t_{1/2}$ is not only the same concerning the fraction of active cells, but also in terms of the number of beads taken up. While the distribution of phagocytotic active cells with a certain number of up-taken beads is very different for the different sizes of beads after 90 min (fig. 2.17a), it is more comparable at $t_{1/2}$ (fig. 2.17b).

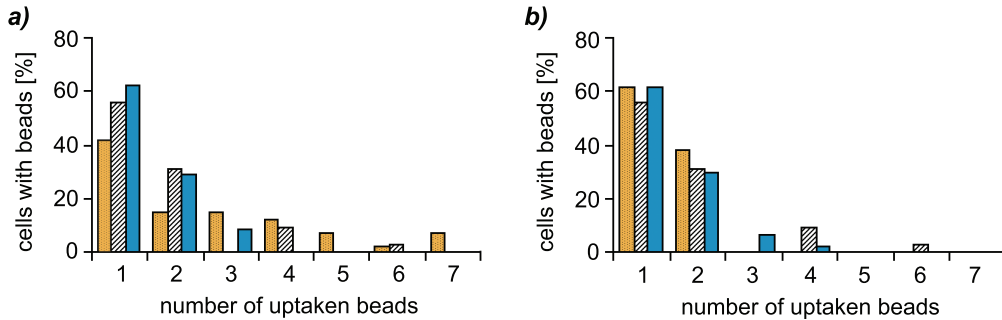


Fig. 2.17 – Number of beads taken up by phagocytotic active cells in the presence of 3.0 μm (orange, dotted), 4.5 μm (green, striped) and 6.0 μm (blue, solid) carboxylated polystyrene beads. a) The histograms show no comparability after 90 min, b) but similar distributions at $t_{1/2}$.

Influence of the PCC

The impact of the PCC on the phagocytotic rate was determined in a similar assay, where the cells had been treated with hyaluronidase before beads were added. Therefore the adhered cells were incubated in 200 μl of a 0.5 mg/ml hyaluronidase solution (HAdase) for 5 min. This treatment results in a complete removal of the coat. Living cells regrow their PCC after this treatment after approximately 3 h. The phagocytosis experiment was therefore performed within this time window.

The phagocytosis rate is significantly increased by the removal of the PCC, as evident by the calculated time constants (table 2.4). All time constants decreased by at least a factor of two (last column in table 2.4) leading to values for $t_{1/2}$ below one hour for all sizes of tested beads.

Even though the phagocytotic rate is increased significantly upon removal of the PCC, the time rate is still strongly dependent on the bead size (fig. 2.19).

Apart from the complete removal of the PCC (achieved by HAdase2) which results in a 2.3 times lower time constant for 4.5 μm beads, the PCC can also be partially removed (as achieved by HAdase1). This partial reduction is hard to quantify, even though it is interesting to see that the observed time constant lies between the full and the removed coat (table 2.5).

Dynamic Adjustment of the PCC

As large particles are the first to be excluded by the PCC and later taken up by the cell, the structure of the PCC is most likely changed during the process. This is also

Table 2.4 – Phagocytotic rate of cells with enzymatic (e) digested PCCs. Therefore, the cells were treated with hyaluronidase. The phagocytotic rate was determined within the time window in which the PCC is not regrown.

bead size	p_e	t_e [h]	$t_{e_{1/2}}$ [h]	t_e [min]	t_e/t
3.00	1.00	0.22	0.15	9	2.09
4.50	0.92	0.79	0.56	34	2.28
4.50	0.76	0.79	0.56	34	2.28
6.00	0.63	1.35	0.94	56	2.32

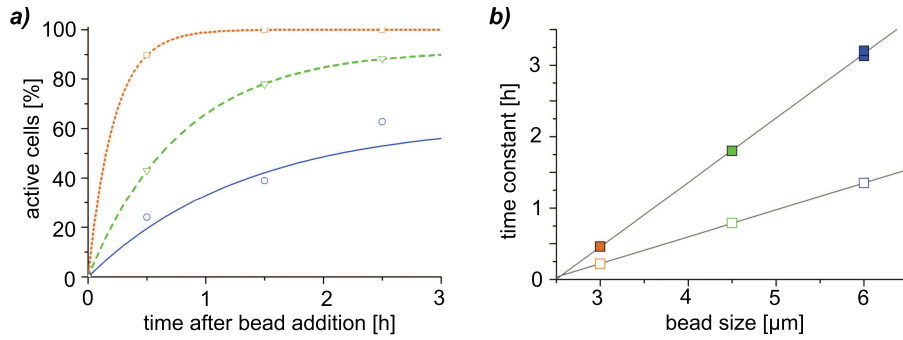


Fig. 2.18 – Phagocytotic activity of hyaluronidase treated RCJ-P cells in the presence of 3.0 μm (orange, dotted), 4.5 μm (green, dashed) and 6.0 μm (blue, solid) carboxylated polystyrene beads: a) Percentage of phagocytotic active cells with kinetic fit from eq. 2.4.3. b) The time constant t depends linearly on the size of the taken-up beads for hyaluronidase treated cells (empty symbols) and non-treated cells (colored symbols).

Table 2.5 – Phagocytotic rate in the presence of 4.5 μm beads on hyaluronidase (HAdase) treated cells, which causes partial (HAdase1) and complete removal (HAdase2) of the PCC.

	p_e	t_e	$t_{e_{1/2}}$ [h]	t_e [min]
HAdase1	0.74	1.45	1.01	61
HAdase2	0.76	0.79	0.56	34
w/o	0.43	1.80	1.44	86

indicated by the PEA. After $t_{1/2}$ and $2t_{1/2}$ PEAs were performed with freshly added erythrocytes at these time points to measure the extend of the PCC without further influence.

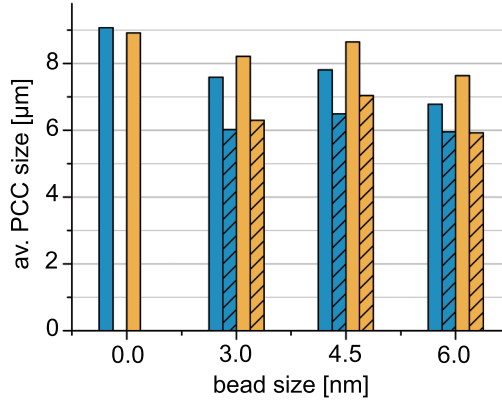


Fig. 2.19 – The PCC is dynamically adjusted in the presence of phagocytosable particles: RCJ-P cells diminish their PCC thickness in a non-locally defined way. In the presence of beads the PCC is significantly smaller after $t_{1/2}$ (blue) and still smaller after $2t_{1/2}$ (orange). This is true for cells without beads taken up (solid bars) and even more for cells after uptake of beads (dashed bars). PCC sizes were measured on four randomly chosen positions around the cell.

The thickness of the PCC measured in these assays after bead addition was significantly reduced for cells that had not taken up particles in comparison to the control without bead addition (fig. 2.19). The size was significantly smaller at both time points, whereas the PCC had been reduced even more at $2t_{1/2}$ compared to $t_{1/2}$. If the cell had taken up at least one particle the size of the PCC was further reduced compared to the cells without taken-up beads in the same samples. The size of the PCC in these cases did not change significantly between $2t_{1/2}$ and $t_{1/2}$.

The change in size of the PCC is not necessarily correlated with a decrease in HA content, but might also be affected by a modified PCC structure. This could lead to a softer PCC, which might not exclude erythrocytes as effectively. The polystyrene particles complicate the direct visualization of the HA in the PCC, as the GFPn adsorbs more strongly to the particles than to the coat. Passivated particles are also not coated with serum proteins, which probably change the uptake of the beads completely. Thus a different technique to characterize the micromechanical properties of the PCC is required.

Chapter 3

Characterization of the Mesoscopic Architecture of Pericellular Coats

The pericellular coat (PCC) has an important impact on all interactions of chondrocytes with their environment. It influences the diffusion rate of biomolecules in close proximity to the cell and governs the force transduction especially important for chondrocytes living in the load bearing cartilage. On the other hand, the cell is able to dynamically adjust its coat during division, motility and phagocytosis as shown in the last chapter. Thus the PCC's underlying structure needs to be adaptable to fulfill all of these requirements.

The molecular picture indicates that the PCC is based on long membrane grafted HA molecules decorated with hyaluronan (HA) binding proteins of different structures and functions. In order to obtain a more detailed spatial picture of the PCC's molecular architecture and its mechanical properties, two independent but complementary techniques for position-resolved analysis of the highly hydrated PCC of RCJ-P cells are being presented. Neither technique affects the living cells to which they are grafted. The HA distribution profile shows an increasing concentration throughout the PCC towards the cell membrane. The corresponding micromechanical map as explored by microrheology shows a gradient of increasing stiffness towards the cell membrane, i.e. enabling a non-linear increase of the repulsiveness of the PCC towards objects approaching the cell membrane. In analogy to this, the HA distribution profiles show a corresponding increasing concentration towards the cell membrane.

The obtained profiles indicate that the structure of HA is far more complex than expected from a pure endgrafted polymer brush. This correlates with the complex structure of the PCC in which the HA is also attached within the chain and its physical properties are modified by HA binding proteins. A HA brush stretched out by aggrecan and HA synthase is proposed, in which HA is bound at least twice to the cell surface. Such a scenario would be consistent with the observed HA distribution profile and the known molecular interaction potentials.

3.1 Visualization of the 3D-Structure of the PCC

Many vital biological processes such as adhesion [23], proliferation, motility or embryogenesis [10] depend on the cell's interaction with its environment. As the outer cell membrane of many mammalian cells is covered by the PCC, it will have a significant impact on any of these interactions. Additionally, it might pose a barrier decreasing the sensitivity of the cell or the diffusion rate of biomolecules. It could also protect the cell during division and prevent cell compression in general [83].

All of these possible functions depend on the composition of the PCC and the molecular architecture governing its viscoelasticity and force transduction. Moreover, some of the PCC components are prone to change with age, or disease: The molecular structure of the HA binding protein aggrecan, most prominent in cartilage, changes for example with age [84, 85] or in osteoarthritis [86]. These changes not only affect the properties of the specific component characterized after purification of the studied protein, but might actually alter the whole mesoscopic organization of the PCC. So far, analysis of the PCC has been very difficult due to its high water content rendering it invisible in most microscopy techniques. Even though new visualization techniques and new fluorescent dyes (see chapter 3.1.1 and 2.2) have been introduced in the last years, no information of the internal structure of the PCC is available so far.

In this part of the work, the characterization of the mesoscopic structure of the PCC on living cells by a combination of a fluorescence and a rheological technique is described. The three dimensional analysis of the PCC's general morphology reveals a thick PCC on all non-adhered membranes (chapter 3.1). Such an extended matrix can be explained by three theoretical models (chapter 3.4.3): The PCC could either consist of a multilayer, be supported by long microvilli, or is being formed by a 'brush-like' structure of HA molecules. Our experiments indicate that the multilayer and microvilli based structures are unlikely explanations for the PCC of chondrocytes (chapter 3.4.3).

Further evidence and a closer look at the molecular architecture of the HA molecules within the PCC can be obtained by the first hyaluronan distribution profiles within a PCC (chapter 3.1.1) and the corresponding micromechanical map of the PCC (chapter 3.3).

3.1.1 RCJ-P Cells are Enveloped by a Thick PCC on all Non-Adhered Membranes

Initial results by *Cohen et al.* based on the environmental scanning electron microscope (ESEM) and the bead based PEA of freshly split cells suggest, that the PCC is present on all non-adhered membranes [28], where they observed thinner coats on the apical sides of the cell. Especially the PEA could be biased by the ability of small fluorescent polystyrene (PS) particles to diffuse into the PCC within the time required for them to settle around the cell (see chapter 2.1). Instead, I characterized the thickness of the PCC on adhered RCJ-P cells with an erythrocyte based 3D-PEA (see chapter ??). Additionally, confocal images of GFPn stained cells illustrate the PCC around the cell.

So far, I employed normal fluorescent microscopy to prove that GFPn selectively stains the PCC. High-resolution images micrometers above the surface with reduced out-of-focus light and a small depth of field can be collected by confocal microscopy. Additionally, these sharply defined optical sections can be reconstituted to three dimensional images. This method has been used in figure 3.1 to demonstrate, that adhered cells are surrounded by a PCC on all non-adhered sides.

Consistent with these results, we could also prove the presence of the PCC on all non-adhered sides of the cell by 3D-PEAs. The beads are eventually able to diffuse into the PCC (chapter 2.4.3), and therefore performed the 3D-PEA not with fluorescent beads [28], but with fluorescently marked red blood cells (chapter 2.1). The red blood

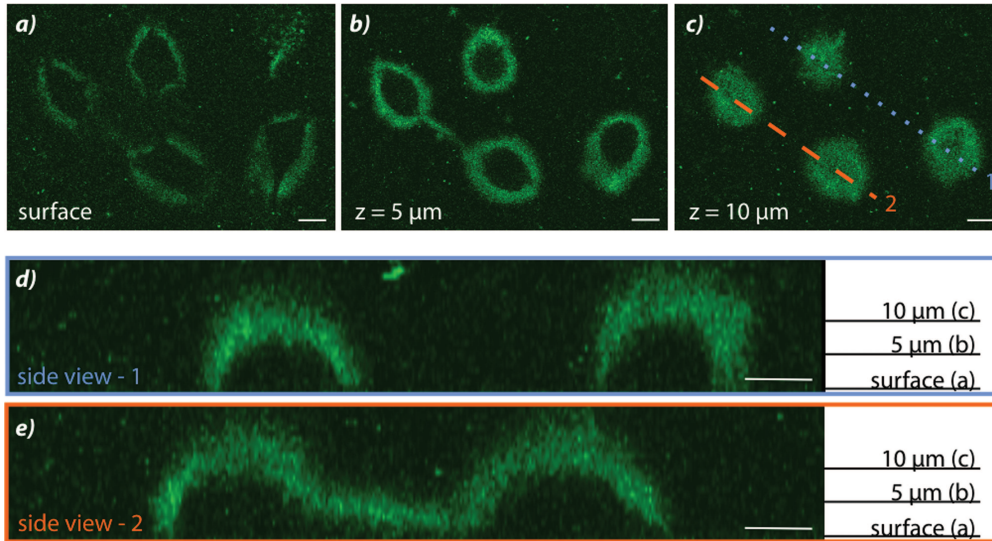


Fig. 3.1 – RCJ-P cells are surrounded by their PCC on all non-adhered membranes: Confocal spinning disk images of GFPn stained RCJ-P cells after 24 h. Images of adhered cells were taken at different heights above the surface. The reconstituted images along the blue dotted line (d) and the dashed orange line (e) were performed on 25 images. All scale bars (in x, y and z) correspond to $10 \mu\text{m}$.

cells are able to move around freely, and their position changes within the time required to image a z-stack of confocal images (fig 3.2). Thus the shape of the red blood cells are not recognizable in the reconstituted images, while the size of the PCC is clearly detectable (fig 3.2).

Comparison of the GFPn stained PCC and the PEA leads to apparently smaller PCCs in the fluorescent staining method. This deviance has also been observed in the 2D PEA with standard fluorescent microscopy (chapter 2.1). It might be caused by an uneven distribution of HA within the coat. Contrary to the polystyrene bead based PEA by as *Cohen et al.* [28], a thinner PCC on the apical side of the cells could not be observed, even 24h after seeding the cells on the glass substrate.

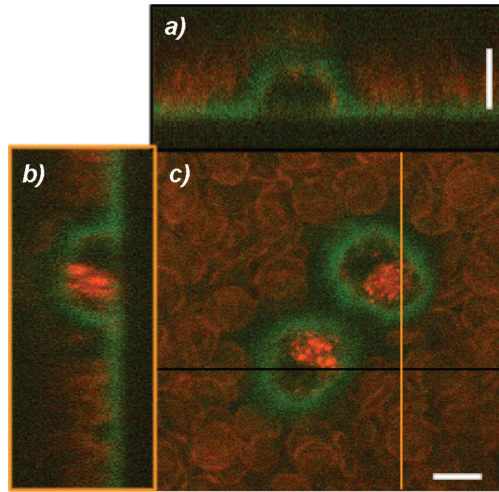


Fig. 3.2 – The thickness of the PCC on the apical side of the cell is comparable to the one on other non adhered membranes: The PCC is visible in the GFPn staining (green) and the 3D PEA with DiI stained erythrocytes (red) on all non-adhered membranes around the cell. The shape of the erythrocytes is not discernible in the reconstruction of the z-stack along the black (a) and orange (b) line in image (c), but allows to determine the thickness of the PCC which varies between 3 and 8 μm . The scale bars correspond to 10 μm .

Under the same FBS conditions (15 %) the thickness typically varies from cell to cell and takes in values of 3 to over 8 μm regarding a singular cell. The average PCC size in the following experimental set for the analysis of the hyaluronan distribution was 5.6 μm with a standard deviation of 1.6 μm .

The variations of the PCC thickness on different areas of the cell, their possible relation to functional processes and dynamic changes (chapter ??) should be reflected by the structure of the coat. Depending on its molecular architecture the cell might be able to adjust the size dynamically without any need to degrade or to synthesize HA. Therefore the characterization of the distribution of HA within the PCC was performed in the first place.

3.2 Mapping the HA Distribution within the PCC

The HA distribution in the PCC was investigated by using neurocan-GFP (GFPn, see chapter 2.2) after proving that it specifically labels HA and does not lead to structural changes of the PCC (see chapter 2.2.2). As the cells produce a stable PCC 4h after seeding on glass cover slides (chapter 2.3), the structure of the coat was analyzed 6 h and 24 h after seeding. The PCC thickness does not vary between the apical and other non adhered membrane parts (see chapter 3.1.1), thus specific studies of the PCC can be carried out at one distinct height. In order to prevent interactions or adsorption to the glass surface all other experiments were carried out $4\ \mu\text{m}$ above the glass slide, corresponding roughly to half the cell height. Well defined thin slices in the z-direction of roughly $1\ \mu\text{m}$ could be obtained with spinning disk microscopy leading to considerable less projection errors and better defined positioning crucial for mapping the hyaluronan distribution.

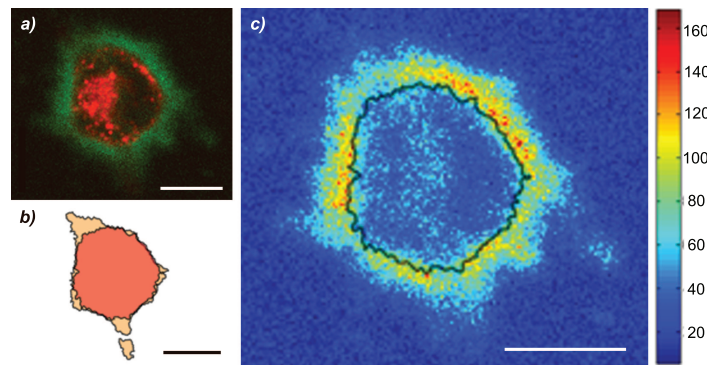


Fig. 3.3 – The distribution of hyaluronan around a cell can be visualized with false color images: Spinning disk images of WGA555 (red) stained cell membrane and GFPn (green) stained hyaluronan are taken $4\ \mu\text{m}$ above the glass slide (a) and at the surface. The shape of the cell is subsequently detected with a self-written Matlab program (b), where the light orange depicts the cell membrane at the surface and the dark orange $4\ \mu\text{m}$ above the surface. After binning, the false color image (c) was calculated with Matlab. The black line depicts the cell membrane. All scale bars correspond to $10\ \mu\text{m}$.

The concentration of hyaluronan varies on different areas of a cell and on different positions within the PCC. Therefore, first the shape of the cell was identified based on the fluorescent staining of the cell membrane with a WGA dye (fig. 3.3b). Thin membrane protrusions on the surface not visible $4\ \mu\text{m}$ above the glass slide can thus be identified. The corresponding areas are subsequently excluded from the analysis. The intensity of the GFPn staining within the PCC is difficult to judge by a mere fluorescent image (fig. 3.3a). Thus, the corresponding false color images representing the intensity distribution of GFPn around the cell was calculated (fig. 3.3c). These images indicate a decreasing hyaluronan concentration throughout the PCC depending on the proximity to the cell membrane.

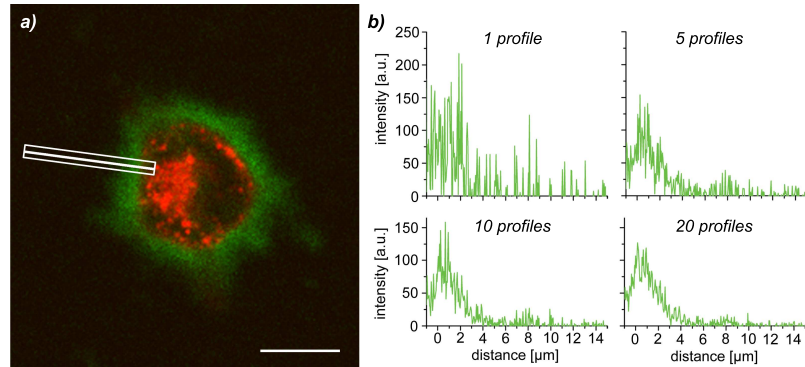


Fig. 3.4 – Averaging over several profiles enables the characterization of the hyaluronan distribution within the PCC: a) All profiles were calculated perpendicular to the cell membrane at the white line, and averaged over different width - the box represents a width of 20 pixels. The average noise was calculated over the outer 50 pixels on all four sides of the image. The signal-to-noise ratio is significantly reduced if the profiles were averaged not only over one (b), or five (c), but 10 (d) or 20 (e) profiles.

To analyze this radial distribution profile, I calculate the intensity profiles of GFPn labeled HA perpendicular to the cell membrane. The relative low concentration of hyaluronan leads to low fluorescent intensity of the GFPn signal resulting in a high signal to noise ratio in the obtained data. Meaningful characterization of the distribution profiles are thus only accessible after averaging the intensities of several parallel adjacent profiles. The center profile is therefore aligned to be perpendicular to the cell membrane. Depending on the number of summed profiles the curve progression is improved, but the resolution is eventually decreased, as profiles further away might be affected by different curvatures of the membrane (fig. 3.4). Depending on the employed magnification, a different number of profiles lead to sufficiently good curves. For the calculated profiles, the number of profiles corresponding to about $1 \mu\text{m}$, which matches the field of depth of the z-resolution, were taken into account.

3.2.1 Hyaluronan Distribution Profiles Show Consistent Curve Progressions

The hyaluronan distribution within the PCC has been characterized by the prior described GFPn intensity profiles. These profiles follow the same curve progression independent of the cell or the position around the cell (fig. 3.5): First a linear increase in intensity is observed over $1.7 \mu\text{m}$ with a standard deviation of $0.5 \mu\text{m}$ up to about the edge of the cell membrane, which has been set to zero. Subsequently, the intensity decreases towards the edge of the PCC. The thickness of the PCC as determined in the PEA corresponds roughly to the loss of GFPn signal intensity.

3.2.2 Short Microvilli Influence the Profile Close to the Cell Membrane

The overlay of the GFPn intensity profiles with the membrane staining shows an initial overlap at the cell edge over $1.7 \mu\text{m}$ (st. dev. 0.5) indicated by an increasing GFPn concentration up to the cell edge at $d = 0$. As this overlap is equally present on all sites

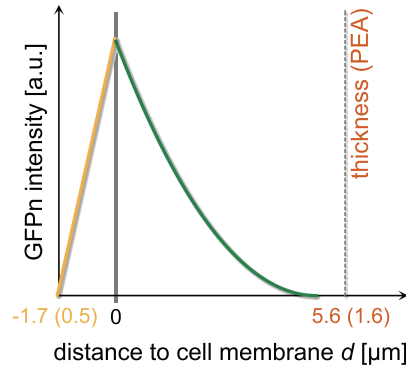


Fig. 3.5 – The GFPn profiles follow a reproducible curve progression: First a linear increase (orange) in intensity is observed up to about the edge of the cell membrane, which has been set to zero. Subsequently, the intensity decreases towards the edge of the PCC (green). The thickness of the PCC as determined in the PEA corresponds roughly to the loss of signal in GFPn intensity.

of the cell, it is probably not caused by drift of the spinning disk, but rather intrinsic to the interaction between cell surface and PCC.

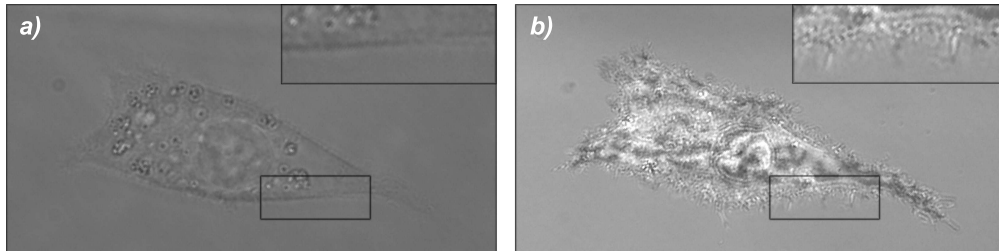


Fig. 3.6 – RICM images show the roughness of the cell membrane and especially the small microvilli at the edge of the cell membrane (a) which are invisible in standard bright field microscopy (b). The microvilli on the edges are very dynamic moving around extremely quickly. The length of the cutout corresponds to 5 μm .

The membranes of RCJ-P cells are covered with small microvilli, thin membrane protrusions, as visualized in by reflective interference contrast microscopy (RICM) close to the glass cover slide (see chapter 5.1.3). On the edges of the cell membrane small, very thin protrusions are visible with very high dynamics, moving around constantly (fig. 3.6). Their patterned appearance in RICM suggests, that most of these protrusions are not sliding along the glass cover slide, but rather move in all three dimensions. However, RICM does not lead to information far away from the sample surface and does not give evidence for the presence of microvilli at the remaining part of the cell membrane.

Additional evidence of microvilli-like structures can be obtained with electron microscopy. To observe the cells in the scanning electron microscope (SEM), they have to be fixed, dried and coated with a conductive layer. All of these steps, especially the drying of the cells, might induce artefacts such as microvilli-like structures. Interestingly, the cell membrane of cells with intact PCCs after fixation (fig. 3.7a) matches the structure of cell membranes on cells treated with hyaluronidase before fixation

(fig. 3.7b).

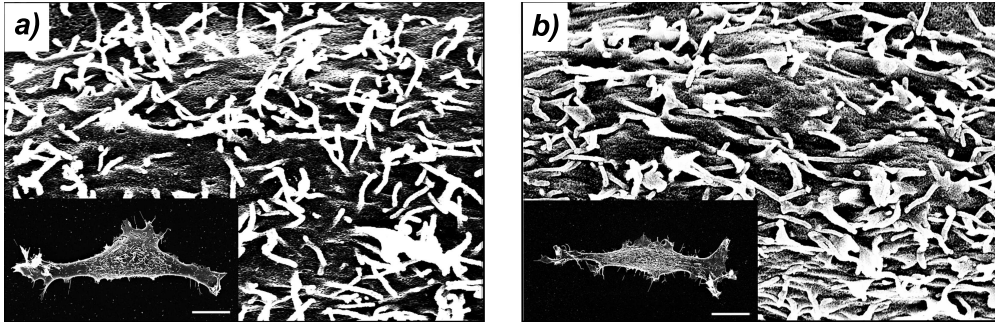


Fig. 3.7 – The cell membrane seems to be covered with small protrusions in SEM images. In order to visualize cells with this technique they were first fixed with glutaraldehyde and then transferred to increasingly higher ethanol concentrations. After critical point drying they were coated with a thin gold layer. Interestingly the cell surface of cells with intact PCCs after fixation (a) correspond to the structure of cell membranes on cells treated with hyaluronidase before fixation (b). The scale bar of the inset and the width of the image correspond to 10 μm .

The microvilli are not visible in spinning disk microscopy images of living cells. However if the cells have been fixed with 1 % glutaraldehyde before visualization, small microvilli can be observed on the cell membrane. The simultaneously performed 3D-PEA demonstrates, that the membrane protrusions do not span the complete PCC and careful image analysis revealed only few longer microvilli. Even though they are present on all non-adhered sites of a cell they are not discernible in life cell microscopy as they are probably highly motile changing faster than the image acquisition time, as already suggested by the RICM images.

Such microvilli explain the roughness of the membrane edge which colocalizes with GFPn labeled HA. Thus the thickness of the microvilli layer can be determined as the width of the overlay of GFPn and membrane dye equal to 1.7 μm (st. dev. 0.5). As the edge of the membrane has been defined as the 'outer edge' of the microvilli layer, these membrane protrusions will not influence further measurements.

3.2.3 Impact of Photobleaching on the Description of the Fluorescent Decrease

The GFPn signal is considerably reduced over time as it is easily photobleached by stray light or during image acquisition. Hence the effect of photobleaching on the observed fluorescent gradients was carefully examined. A series of images was taken at one position with the usual experimental setup. As expected, the overall intensity of the profile summed over 10 pixels decreased with time (fig. 3.8).

The relative bleaching caused by the acquisition of one image can be calculated with an exponential formula:

$$\lambda(t_0, t) = \left(\frac{A(t)}{A(t_0)} \right)^{\frac{1}{N}} - 1 \quad (3.1)$$

where $N = t - t_0$ denotes the number of images taken between t_0 and t and $A(t)$ corresponds to the fluorescent intensity at the corresponding image. If the percentage of fluorescence loss between the 3rd and the 51st image taken is considered, about 1 % of fluorescent molecules are bleached in each image acquisition step.

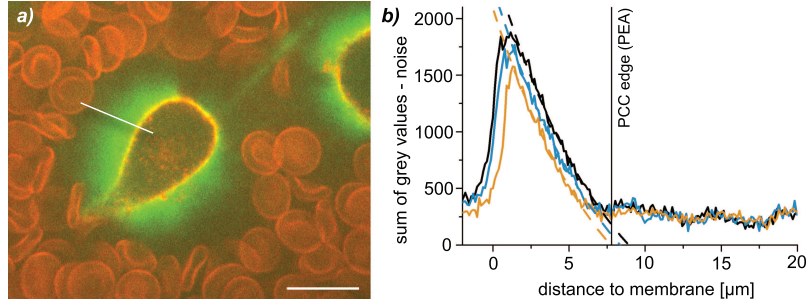


Fig. 3.8 – Photobleaching of GFPn stained hyaluronan: a) The fluorescent intensity along the white line averaged over 10 pixel (white box) decreases over the whole profile (b) from the 3rd (black line) to the 27th (blue line) and 51st (orange line) image. The cell (a) was imaged with WGA555 stained cell membrane (red), the DiI stained red blood cells (red) and the GFPn stained hyaluronan (green) 24 h after seeding. The relative bleaching caused by the acquisition of one image was thus calculated to be about 1%. The exponential fits were performed between 0.8 and 5 with a decay constant equal to the PEA determined PCC thickness. The scale bar corresponds to 100 μm .

Additionally, GFPn fluorescence decreases over time around cells, probably through radical reactions with metabolic cell products. Therefore long term experiments can not be performed with this method in order to study the change of the PCC's structure of the same cells. Within the experimental time frame this effect accounts for less than 1 % in 15 min. Thus bleaching of GFPn molecules can be ignored within a standard experimental setup.

If images of different samples or on differently bleached areas of one sample are compared to one another, it is instructive to know how far the shape of the profile changes. As the signal is reduced by a factor of p through photobleaching, the effective profile needs to be divided by this factor. For an exponential fit, the decay constant is thus unaffected by the bleaching.

In contrast, the decay constant of the exponential fit of the different bleached profiles fitted from $d = 0.8$ to $d = 5$ decreases with higher photobleaching (table 3.1). The fits are strongly dependent on the chosen data range and thus largely affected by the noise in the tail region.

Table 3.1 – The decrease of GFPn intensity can be more precisely described by the slope than the exponential decay constant: Exponential fits following equation $y = A \cdot e^{-x/t}$ were performed between $0.8 < d < 5$. The slope m is not considerably affected by bleaching. Linear fits of the form $y = A - mx$ were performed between $0.8 < d < 5$.

	3	15	27	39	51
t	3.79	3.70	3.56	3.03	2.57
m	123	121	188	125	138

The curves can also all be fitted with an exponential where t was set equal to the thickness of the PCC as determined in the PEA (here $t = 7.8 \mu\text{m}$). The fit works very well as evident by an R^2 -value of 0.988 for all curves (fig. 3.8).

The slope of a linear fit on the other hand should depend more strongly on the amount of bleaching. The slopes determined for the bleached profiles are however all in the same size regime (table 3.1). Thus indicating, that the slope may be a suitable parameter to compare cells with the exact same experimental setup.

3.2.4 Analysis of the Decreasing HA Concentration

One would expect a decreasing HA concentration on round cells with larger distances to the cell membrane due to the radially increasing volume. However, the decrease in GFPn intensity within the PCC proved to be independent of the membrane curvature. The decreasing GFPn intensities can also be observed on straight membrane sections (fig. 3.9).

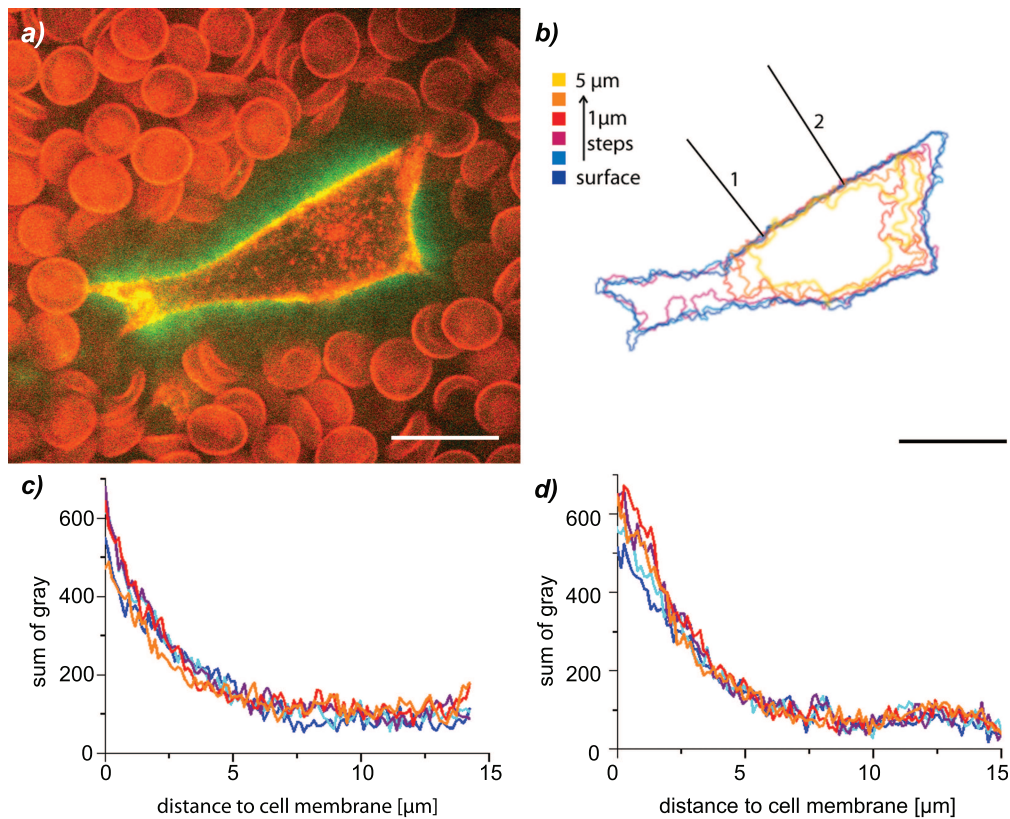


Fig. 3.9 – The GFPn intensity profile is comparable at different cell heights:
a) The cell membrane was stained with WGA555 (red), the hyaluronan with GFPn (green) and the erythrocytes with DiI (red). The image was taken at the surface of the glass slide. b) The height profile indicates that the cell membrane is very flat like a wall at the positions 1 and 2 where the profiles (c) and (d) were calculated. The scale bars correspond to 10 μm.

The coat thickness t was measured by PEAs. For each profile, the absolute position d was set to zero at the cell membrane as measured from the fluorescent intensity peak of WGA555. The distance towards the PCC edge was subsequently given in μm with typical PCC thicknesses ranging from 3 to 8 μm. In order to relate the decreasing HA concentration towards the PCC edge to the coat thickness t , the spatial variation of the GFPn intensity profiles 4 μm above the glass surface were analyzed. Therefore,

we performed a linear fit to several intensity profiles, $I(d) = md + I(0)$, where m is the slope, I is the intensity and d is the distance to the membrane in μm . Fitting an exponential decay to the data failed due to the high noise ratio at low fluorescence intensity away from the cell membrane. The slopes of one sample measured with identical settings, show an inverse correlation to the PCC thickness t (fig. 3.10a):

$$m = st^{-1} \quad (3.2)$$

The parameter s was determined by the average maximum GFPn intensity. The correlation of the intensity gradient to the PCC thickness underlines that normalization by the thickness t yields uniform profiles.

$$p = d/t \quad (3.3)$$

Thus a relative coordinate system (fig. 4.4) was defined, where the edge of the PCC was set to one. The cell membrane was set to zero, determined by the sharp drop in intensity of the membrane dye WGA555. The absolute position d can easily be related to the relative position p by equation 3.2.4.

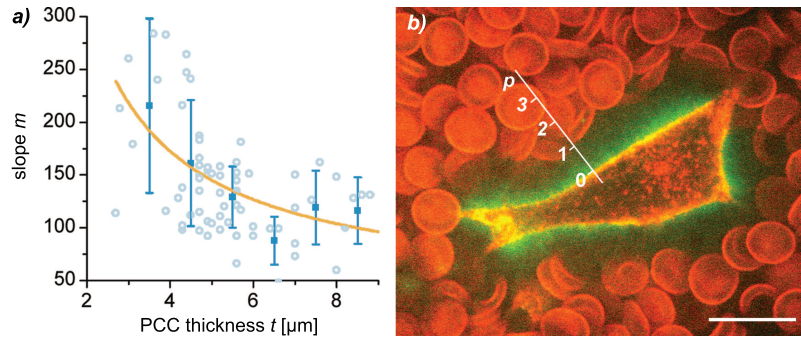


Fig. 3.10 – The relative coordinate system is defined by a fluorescent PEA and the fluorescently stained cell membrane. a) The relation between the slope of the decreasing GFPn intensity and the PEA determined thickness underlines that normalization of the measurement values by the thickness t yields uniform profiles. b) The drop in membrane dye WGA555 intensity is set to zero and the edge of the PCC determined by the DiI stained erythrocytes is set to one. This relates the absolute distance d to the relative position p following eq. 3.2.4.

Definition of the coordinate system in such an independent fashion enables the comparison of the PCC's structure mapped with different techniques or on different cells. Several profiles of a single cell can thus be averaged to obtain a curve, which can subsequently be compared to other cells. The maximal GFPn intensity showed no relation to the thickness of the PCC. Hence, the averaged curves can be normalized by their maximal intensity and the curve progression of the HA distribution can be compared between different samples and even different batches of GFPn or different image acquisition settings (fig. 3.11).

3.2.5 Discussion of Possible Impacts of GFPn Staining on the Results

Labeling cells with GFPn successfully stained the hyaluronan within the PCC. This treatment did not harm the living cells and did not seem to alter the PCC since no change in thickness was observed as measured by PEA. However, any interactions of

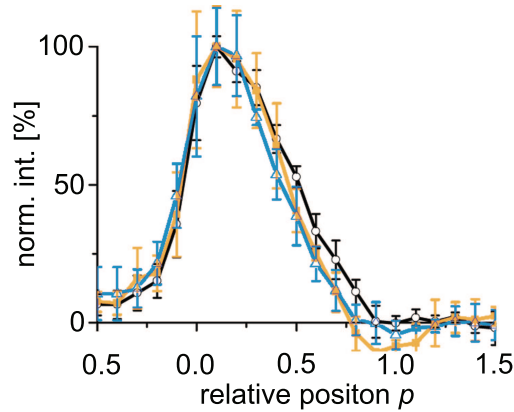


Fig. 3.11 – The relative HA distribution is very similar on different cells: The distribution profiles were obtained by averaging over five different profiles around each cell and subsequent normalization. The profiles of cell 1 (black circles), cell 2 (orange squares) and cell 3 (blue triangles) show similar shapes.

the cell with HA might be influenced by the GFPn attachment, possibly leading to a modified take-up of hyaluronan or a modified cell response. To minimize such long-term effects, we performed all fluorescence experiments right after GFPn addition.

Additionally, small parts of HA might be blocked by other hyaluronan binding proteins. The GFPn intensity can therefore not be correlated to an absolute HA concentration. The experimental setup would consequently benefit tremendously from a simultaneous visualization of hyaladherins or at least the most prominent hyaladherin, aggrecan. However, so far the available antibodies are not applicable on living cells.

GFPn staining outside of cells is subjected to a high photobleaching rate, readily observed in standard fluorescent and confocal laser scanning microscopy. This effect is considerably reduced in spinning disk microscopy which yields reproducible intensity profiles within one sample at the same settings. Normalization and a relative coordinate system based on the PEA determined thickness further enable comparison of HA distribution profiles from different experiments. The definition of such an independent relative coordinate system further allows to compare the acquired HA distribution profiles to the micromechanical map introduced in the next chapters.

3.3 Micromechanical Profile of the PCC

Chondrocytes live in a mechanically challenging environment. In order to understand, their adaptation to these special conditions, it is important to measure the physical properties of the cell and the enveloping PCC and to analyze their reaction to mechanical strain.

The reaction of chondrocytes to mechanical strain can be observed with a strain apparatus: The first system applied an uniaxial compressive load to chondrosarcoma cells seeded in agarose gels [87]. They used this system to analyze the shape changes induced by mechanical stress. A simultaneously developed strain apparatus by the group of *Prof. Bader* (University of London) showed, that the extent of the matrix decreases cell deformation [88]. They could further show, that compressive strain on chondrocytes influences intracellular Ca^{2+} signaling [89], whereas both static and cyclic stretching leads to a rearrangement of their actin cytoskeleton [90]. Adhered synoviocytes even increase their HA secretion after short static stretching [91].

The physical properties of the PCC can be measured by micropipet aspiration [92]. In this setup, a cell is sucked into a pipette either completely or only partially depending on the diameter of the micropipet and the applied pressure. The deformation of the cell is then correlated to its Young's modulus. In order to measure the properties of the PCC, a complex analysis of the results is required to decouple the influence of the simultaneously measured cell body [93]. In addition to the Young's modulus, the Poisson ratio has also been determined by this technique [94].

Atomic force microscopy offers the advantage to measure the viscoelasticity of the PCC at different regions of a cell [95–97]. However, this technique also requires a complex analysis based for example on the Hertzian model or a finite element analysis [96].

The obtained averaged Young's moduli of the PCC yield valuable information for a better understanding of stress conduction within the cartilage [98] or disease related changes, indicating for example a mechanical difference between arthritic and normal human chondrocytes [93].

However, the presented techniques have two drawbacks in common: they do not yield information on the structure of the PCC perpendicular to the cell surface and they require a complex analysis to decouple the mechanical properties of the PCC from the simultaneously measured cell body. Thus it has not been possible to measure the density profile of the PCC. Such a micromechanical profile could help to understand the construction of the PCC, which in turn is essential in understanding how the molecular interactions of hyaluronan and their binding proteins [40, 44] can govern the microscopic dynamics of the PCC and its interplay between the cell and the extracellular environment.

Therefore a technique capable of measuring the mechanical profile of such a soft material in a position dependent manner was required. Even though passive particle tracking microrheology (chapter 1.3) has barely been used to map mechanical properties, it is intrinsically capable of doing so. The available analysis software was adjusted to measure the viscoelastic properties of the PCC in a position dependent manner. Thereby the tendency of small particles such as polystyrene spheres to diffuse into the PCC was utilized (chapter 2.4.3). Thus I obtained the first micromechanical profile of the PCC on living cells.

3.3.1 The Viscoelastic Properties of the PCC Change Gradually Towards the Cell Membrane

I mapped the micromechanical properties of the PCC by spatially resolving the Brownian motion of $0.45 \mu\text{m}$ tracer particles (fig. 3.12). The position of each tracer particle

was mapped (with respect to the membrane and the edge of the PCC in terms of its relative position) and analyzed its diffusive motion. The center of the track, r_{mean} , is

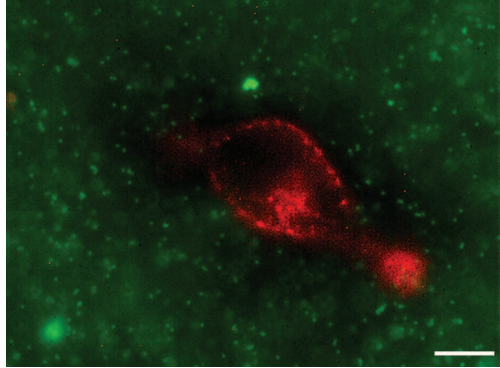


Fig. 3.12 – The micromechanical profile of the PCC is obtained by observing the Brownian motion of tracer particles in a spatially resolved manner. The $0.45 \mu\text{m}$ polystyrene beads (green) diffuse into the PCC around the cell (membrane labeled red by WGA555). The scale bar corresponds to $5 \mu\text{m}$.

calculated as the mean of all N positions r_k within the track:

$$r_{mean} = \frac{1}{N} \sum_{k=1}^N r_k \quad (3.4)$$

The distance of the track from the cell surface is then defined by the shortest line connecting the center of the track with the cell surface.

Typically, particles move about their mean position to an extent characterized by the average radius of motion R_m , which is $0.45 \mu\text{m}$ (st. dev. $0.24 \mu\text{m}$ - see chapter 3.3.3 for more details).

$$R_m^2 = \frac{1}{N} \sum_{k=1}^N (r_k - r_{mean})^2 \quad (3.5)$$

Examination of the trajectories revealed continuous diffusion without trapping events (compare chapter 1.3.3). The free diffusion of particles into and out of the PCC over longer periods of time confirms that they are not bound to PCC components. This was further validated by control microrheology experiments in HA solutions, which yielded results consistent with literature values (chapter 3.4.1).

The motion of the $0.45 \mu\text{m}$ polystyrene beads was imaged $4 \mu\text{m}$ above the surface to prevent artefacts induced by interactions of the particles or the PCC with the glass slide. After each experiment the cell membrane was imaged in fluorescent mode at the glass surface and at the measurement height. Additionally, a PEA was performed after each set of experiments.

The fluorescent staining of the PCC with GFPn and the PEAs suggest an inhomogenous amount of PCC on cell protrusions (compare ??). Therefore these areas are excluded during analysis.

The diffusion of tracer particles in a viscoelastic solution (compare chapter 1.3.2) can be characterized by the mean squared displacement (MSD) in a certain lag time τ . This can further be related to the diffusion constant D in 2 dimensions with the diffusive exponent α :

$$MSD(\tau) = 4 \cdot D \cdot \tau^\alpha \quad (3.6)$$

For complex solutions, exhibiting both viscous and elastic behavior, both contributions are reflected by the thermal motion of Brownian particles [66]. As the response of

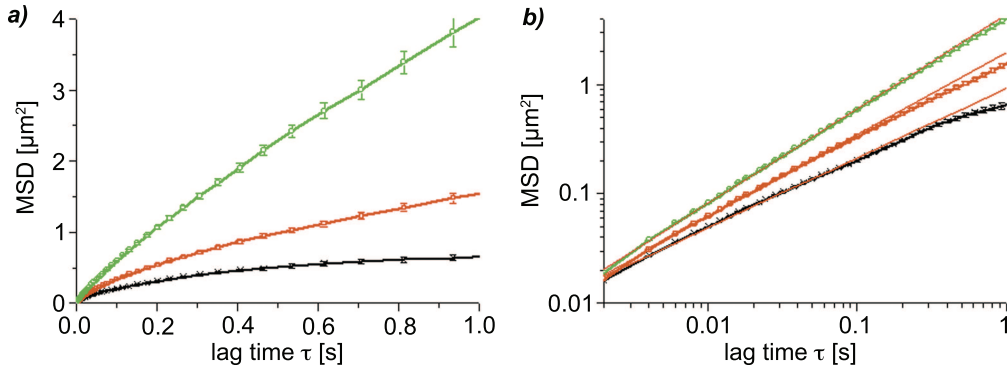


Fig. 3.13 – The MSD(0.01s) were calculated over a certain relative position between 1.0 and 0.7 (green), or 0.7-0.4 (red) or 0.4-0.1 (black).

complex materials are typically frequency dependent, the MSD of these materials does not evolve linearly with time. Therefore the diffusive exponent α has been introduced. The diffusive exponent, α , is related to the ratio of elastic and viscous contributions of the solution such that $\alpha = 1$ in purely viscous and $\alpha = 0$ in purely elastic solutions, whereas $\alpha = 0.5$ at the gel point [59] and $\alpha > 1$ for superdiffusion in active processes.

Inside the cell coat, variation of the viscoelasticity is indicated by slower motion of tracer particles and their correspondingly smaller MSDs as they approach the cell surface. To characterize this decrease, the obtained tracks are first sorted according to their distance to the cell membrane and the MSD is calculated for all tracks in a certain distance group (e.g. all tracks whose relative position within the PCC lies between 1.0 and 0.7). These averaged MSD curves clearly indicate a decrease in viscosity towards the edge of the PCC (fig. 3.13a) related to the smaller MSD values observed at a relative position of 0.4 - 0.1 compared to 0.7 - 1.0. The diffusive exponent α , corresponding to the log-log slope of the MSD, also deviates from purely viscous diffusion inside the PCC (fig. 3.13b).

In order to calculate the accurate viscoelastic properties of the embedding solution, the MSD and the diffusive exponent at a certain lag time τ can be related to the viscous loss modulus G'' and the elastic storage modulus G' [68,69] following equation 1.12. Since, this algebraic expansion only works in mainly viscous or mainly elastic regimes, the analysis was based on the original diffusive exponent and MSD first values. A profile of the decreasing stiffness of the PCC can be obtained by plotting the MSD value at a specific lag time against the entire range of relative positions (fig. 3.14). Similarly, the diffusive exponent decreases linearly towards the cell membrane, illustrating the increasing elasticity of the PCC up to the gel point (fig. 3.15).

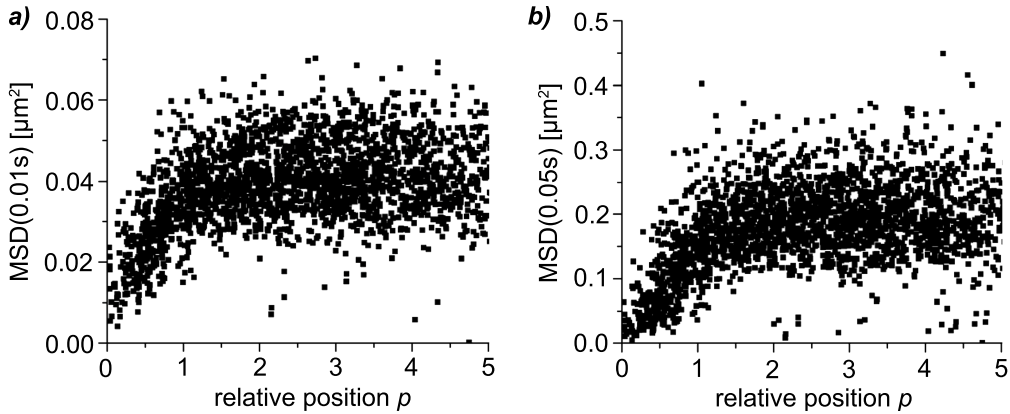


Fig. 3.14 – The MSD decreases towards the cell membrane. Each black dot represents the MSD value of one tracer at a lag time of 0.01 s (a) and of 0.05 s (b).

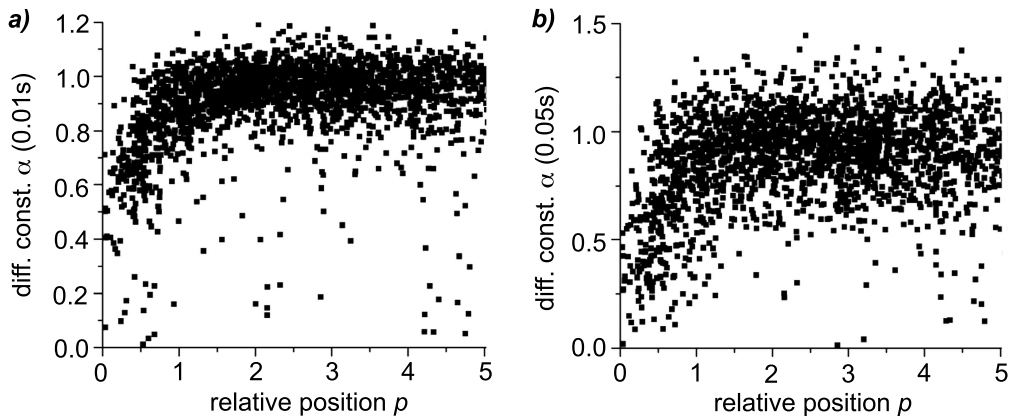


Fig. 3.15 – The diffusive constant decreases towards the cell membrane. Each black dot represents the diffusive constant of one tracer at a lag time of $\tau = 0.01$ s (a) and of 0.05 s (b).

3.3.2 The Different Cells and Different Areas do not Lead to Enlarged Distributions of the Diffusive Exponent

The micromechanical profile of the PCC is based on different areas of a cell over 11 cells. The fluorescent analysis of the HA distribution within the PCC indicates a constant distribution profile over multiple cells in a relative coordinate system. Variations induced by different cells or different areas of a cell on the micromechanical map can be checked by two methods. First, the diffusive exponent of different cells was compared and then its distribution over the whole range of relative positions was analyzed.

To quantify the correlation of the different data sets, the data of the nine cells with more than 20 tracers within the PCC were compared. First their similarity in pure media was calculated, where each dataset was averaged between a relative position of 2 and 4. The standard deviation (0.017) showed less than a 2% divergence from the overall average of 0.964.

As α decreases linearly within the PCC all datasets were individually fitted to $y = A + Bx$ at a relative position between zero and one. The average slope corresponds to 0.463 ± 0.025 , determined by the linear fit with a slope of zero through all slopes with their respective standard deviations (fig. 3.16). This corresponds to a deviation of

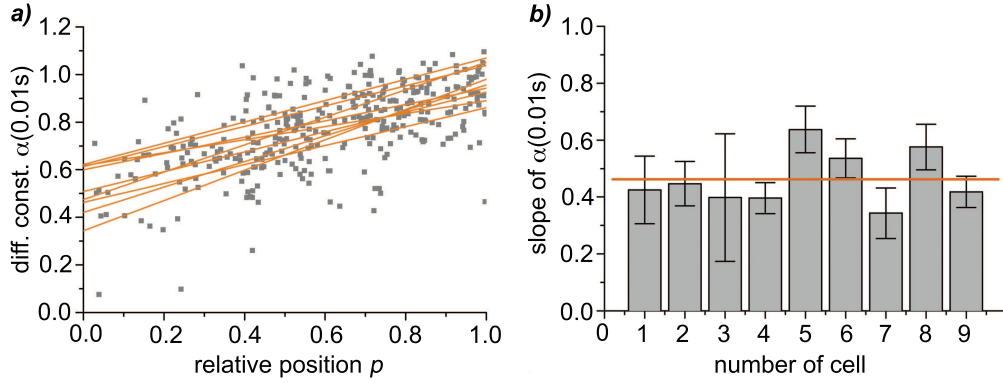


Fig. 3.16 – The increase of the diffusive constant of different cells is comparable: a) The linear fit through the diffusive constant of the single cells (orange lines) and especially their slope (b) overlap with a standard deviation of only 5.4%.

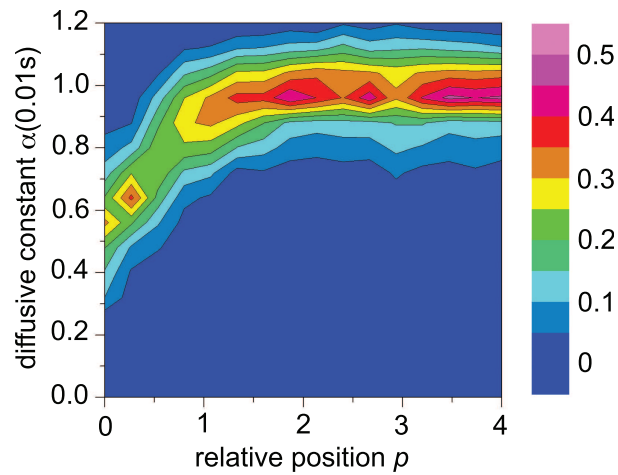


Fig. 3.17 – The distribution of alpha is not increased within the PCC. The distribution at the different positions is broadened by the statistical thermal noise. As the width of the distribution in media is comparable to that within the PCC, it is not enlarged by differences between cells and different areas of the PCC.

the slopes of 5.4%. If the same calculation is carried out in terms of absolute distances, the average value of the slope is 0.085 ± 0.008 corresponding to a deviation of 8.7%.

Additionally, I analyzed the distribution of the diffusive exponent in a density plot (fig. 3.17). The distribution at the different positions is broadened by the statistical thermal noise. The distribution is especially large due to the very low viscosity of water leading to large radii of motion. The width of the distribution in media, measured perpendicular to the main axis, is comparable to that within the PCC. Thus neither the different cells nor the different areas enlarge the distribution of the diffusive exponent.

3.3.3 The Obtained Microrheological Profile is Meaningful

Passive particle tracking microrheology is an ideal technique for studying the material properties of soft materials. For its successful application three criteria have to be fulfilled: 1) the thermal motion of the particles has to be visualized. This depends on the softness of the material, which should not constrict particles too much and the equipment used. The vigorous motion of particles in very viscous solutions such as water or the PCC requires a high speed camera to obtain enough statistics before they move out of the field of focus. 2) The tracers have to be homogeneously distributed within the sample without altering it. Therefore, we allowed particles to diffuse into the PCC, thus neither the cell nor the PCC is perturbed. As particles diffuse all the way to the cell on non-repetitive tracks, no large scale structures seem to be present on the time scale of observation. This also indicates that the hyaluronan is not cross-linked to form a net with a mesh size lower than the particle diameter of 450 nm. 3) For microrheology the particle diameter has to be sufficiently larger than the correlation length of the polymer solution [54]. If the polymers are not cross linked, this length depends on the concentration and length of polymers and is also referred to as mesh size. On the other hand, if the particles are a lot smaller than the mesh size, they will not probe the polymer properties but just the properties of the solvent. We therefore employed rather large beads with a diameter of 450 nm. However to double check, the MR experiments should be repeated with differently sized beads.

Microrheology experiments are intrinsically extremely sensitive to any kind of distortion affecting the particle motion. The sample was therefore equilibrated for 15 min prior to the start of the experiment and particles far away from the cell always served as controls to check for flow within the sample. Motion of the cell close by seemed to play no important role, as no changes in the viscoelastic properties were observed on living, hyaluronidase treated cells. As no motor proteins have been reported inside the PCC, active processes such as those present inside the cells do not have to be considered here.

In the following section the critical issues in MR experiments are double-checked: Control measurements on PCC devoid cells show no decrease of the MSD or the diffusive exponent. The viscosity of the solution far away from any cell is purely viscous. Our image acquisition rate is high enough to ensure good statistics and the radius of motion is small enough to resolve changes within the PCC.

PCC Devoid Cells Show No Changes in the Viscoelastic Properties Close to the Cell

The measurements of the PCC are intrinsically carried out in close proximity to the cell membrane. This vicinity to a wall-like structure could affect the Brownian motion by hydrodynamic wall effects. Theoretically the diffusive exponent should not be affected by wall effects, as hydrodynamic interactions should only lead to a reduced amplitude of the Brownian motion. Thus the MSD could be affected in the very close proximity to the cell. As a control, measurements on PCC devoid cells were performed. These

cells had been treated with hyaluronidase first, which specifically removes the PCC and does not alter the cells otherwise. No change of the diffusive exponent nor the MSD values could be observed near those cells (fig. 3.18). Thus, hydrodynamic wall effects do not influence the measurements.

The Solution Far Away from the Cell is Purely Viscous

The MSD at a lag time of 0.01 s in media was averaged over a relative position between 2 and 4 leading to $MSD(0.01s)_{media} = 6.35 \cdot 10^{-2} \pm 1.41 \cdot 10^{-2} \mu m^2$. Together with the averaged value of the diffusive exponent α at this lag time and position, $\alpha(0.01s)_{media} = 0.964 \pm 0.017$, the values for the storage modulus G' and the loss modulus G'' can be calculated with the algebraic expansion introduced by *Mason et al.* [68, 69]: $G'(100Hz)_{media} = 4.1 \cdot 10^{-3} Pa$ and $G''(100Hz)_{media} = 7.25 \cdot 10^{-2} Pa$.

As the storage modulus is more than a decade smaller than the loss modulus it can be neglected. The slope of G'' equals the viscosity. For a purely viscous solution $G''(0 Hz) = 0 Pa$ and thus the viscosity at a relative position of 2 to 4 follows to be $7.25 \cdot 10^{-4} Pa \cdot s$, which corresponds well to the expected $6.9 \cdot 10^{-4} Pa \cdot s$ for water at 37°C.

The High Speed Camera Images Traces of Sufficient Length

One difficulty in measuring aqueous solutions, lies in the short time window in which particles stay within the field of view. They do not only move fast in x/y, but also in z leading to relatively short trajectories. Image acquisition with a high-speed camera enabled to set the minimal length of each track to 650 frames, thus ensuring good enough statistics. To prove that the small deviation in the diffusive exponent from 1 is not caused by short trajectories we also calculated the weighted slope α_w

$$\alpha_w(\omega, p) = \frac{\sum_i n_i \alpha(\omega, p)_i}{\sum_i n_i} \quad (3.7)$$

where n corresponds to the number of tracks for each track i within the relative position p . The weighted tracks were averaged over a relative position of 0.1 and correspond very well to the values for alpha averaged over the same position (fig. 3.19a). The averaged weighted MSD was calculated accordingly and also corresponds to the weighted MSD. This indicates, that the chosen minimal particle track length is sufficient.

The Radius of Motion is Small Enough to Resolve Changes Within the PCC

The area covered by a particle within a certain time window also depends on the viscoelasticity of the solution. Thus the radius of motion does not depend much on the length of the tracks, but changes significantly within the PCC (fig. 3.20). Where the tracer particle show an average radius of motion of $0.76 \mu m$ in media, it is reduced to $0.26 \mu m$ at a relative position of 0.1 ± 0.05 . The average radius of motion increases exponentially within the PCC.

3.3.4 The Loss and Storage Modulus can Only be Calculated with Great Uncertainty

The mean-squared displacement characterizing the Brownian motion of single particles can be employed to calculate the viscoelastic properties of the solution in terms of their loss and storage moduli. They can be calculated from an assembly of particles at a

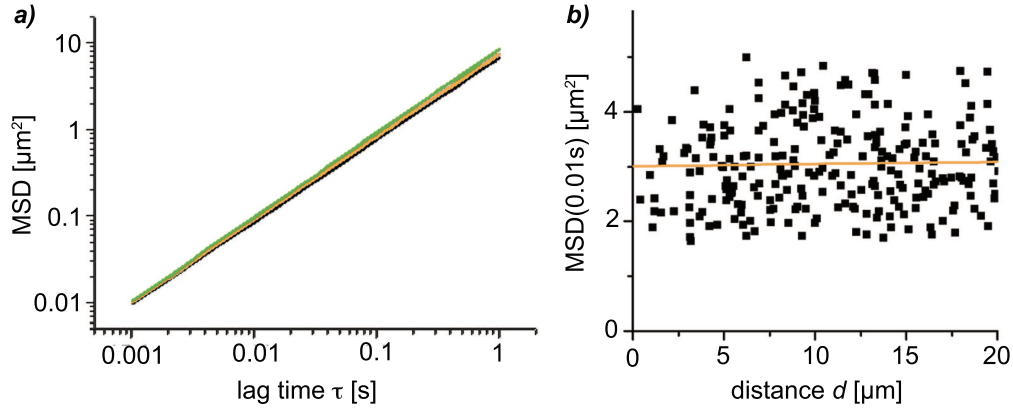


Fig. 3.18 – The Brownian motion of the tracer particles is not affected by a cell in close proximity: a) The diffusive exponent, given by the double logarithmic slope of the MSD, corresponds to purely diffusive motion averaged over particles of $d = 7 - 5 \mu\text{m}$ ($\alpha = 0.97$), $d = 5 - 3 \mu\text{m}$ ($\alpha = 0.95$) and $d = 3 - 1 \mu\text{m}$ ($\alpha = 0.95$) from 5 different cells on 3 different samples. b) The values of the MSD at a lag time of 0.01 s is also not affected by the close proximity of the cell.

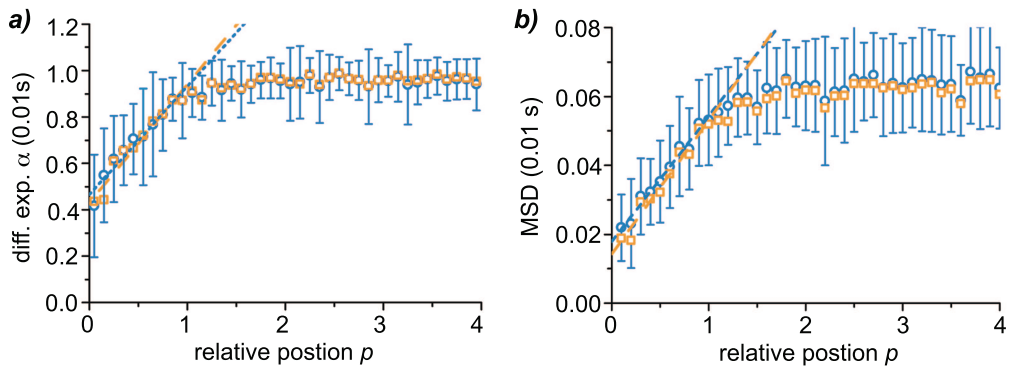


Fig. 3.19 – The weighted data corresponds well to the non-weighted: The diffusive exponent shows the same curve progression for weighted (orange, squares) and averaged (blue circles) diffusive exponents (a) and MSDs (b), where the error bars depict the standard deviation of the averages. The linear fit performed between $0 < p < 1$, also overlap nicely: a) $y_w = 0.43 + 0.51x$ compared to $y_a = 0.47 + 0.47x$; b) $y_w = 0.014 + 0.039x$ and $y_a = 0.018 + 0.036x$.

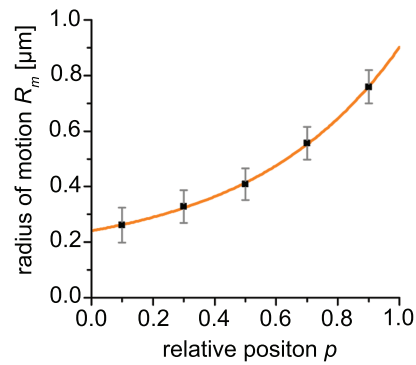


Fig. 3.20 – Beads move less in closer proximity to the cell according to the increasing viscoelasticity, the radius of motion decreases exponentially towards the cell. The orange line depicts the exponential fit: $y = 0.15 + 009e^{0.48x}$.

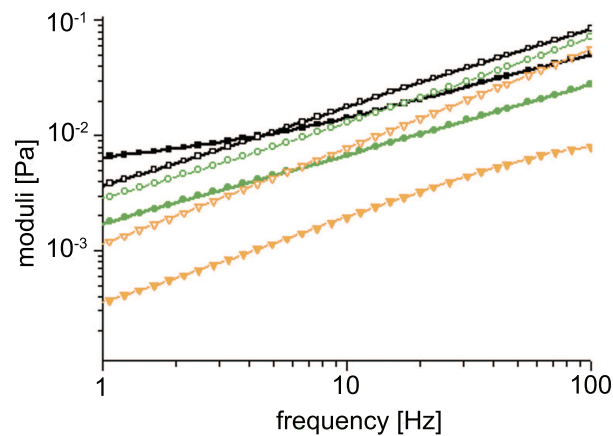


Fig. 3.21 – Loss and storage moduli are decreased within the PCC: The calculated moduli are subject to a conversion error of up to 15%. Empty symbols represent the loss modulus G'' and filled symbols the storage modulus G' at a relative position of 0.1-0.4 (black), 0.4-0.7 (green) and 0.7-1.0 (orange).

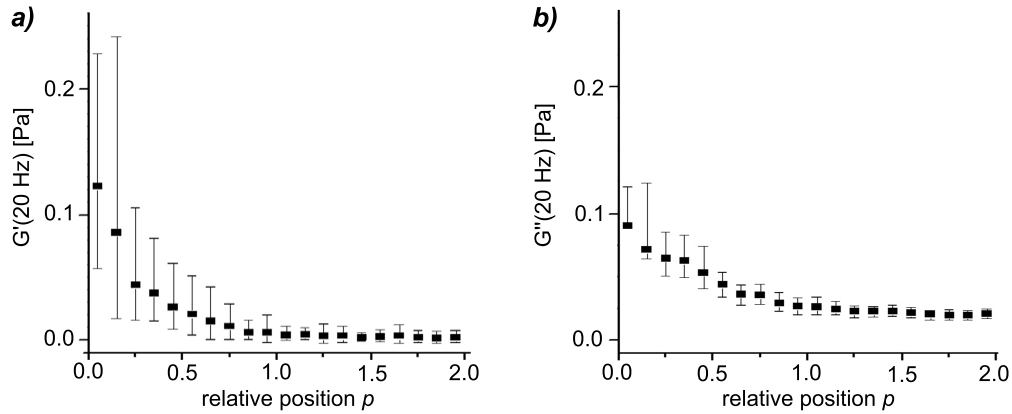


Fig. 3.22 – The Loss and storage moduli can only be calculated with a high uncertainty: The presented error bars are based only on the standard deviation of MSD and alpha, not considering the additional conversion error of up to 15%.

certain range of relative positions (fig. 3.21). The obtained loss and storage moduli decrease within the PCC. A crossover of the storage and loss module can only be observed for the position range very close to the cell membrane, between a relative position of 0.1 and 0.4.

For a given lag time the MSD value and the diffusive exponent were averaged over all particles with the same relative position. Using the algebraic expansion, the G moduli over the whole position range can be calculated (fig. 3.22). The error of the obtained moduli depends on the standard deviation of this averaging and is additionally subject to a conversion error of up to 15% [69]. The values of the storage and loss moduli are thus not as reliable as the original values of the MSD and the diffusion exponent.

3.4 Deducing the Mesoscopic Structure of the PCC

Fluorescent analysis of the HA distribution and microrheological mapping revealed a homogenous structure of the PCC. The PCC profiles show a decreasing hyaluronan distribution and 'softer' micromechanical properties towards the fringes of the PCC. The force required to push through the PCC towards the cell is thus non-linearly increasing for objects larger than the mesh size of the PCC. Correspondingly, the force transduction between the cartilage and the embedded chondrocyte will be affected by this gradient of increasing viscoelasticity.

Additionally, the observed profiles can be related to the structure of the PCC based on general scaling principles of polymer physics first introduced by *Pierre-Gilles de Gennes*. Therefore, first the required polymer theories are summarized and then they are related to the properties of hyaluronan in order to deduce a possible molecular structure of the PCC based on the observed profiles.

3.4.1 Hyaluronan is a Flexible Polymer

Hyaluronan is a linear polysaccharide that consists of up to 25000 disaccharides (chapter ??). From a polymer physics point of view, hyaluronan is a linear polymer of up to 25000 monomers. The number of monomers is directly related to the overall length of the polymer, if it was fully stretched out. The distance between the ends in such an extended conformation is referred to as the contour length l_c . However, in solution this fully stretched conformation is highly unlikely. Instead the polymer forms a random coil. The space occupied by one coiled polymer is characterized by a sphere. The radius of the sphere is defined as the radius of gyration R_g , which corresponds to the mean square of the distance between the monomers r_i and the center of mass r_G [99].

$$R_g^2 = \frac{1}{N+1} \sum_{i=0}^N \langle (r_i - r_G)^2 \rangle \quad (3.8)$$

The dimension of polymer coils in solution is generally governed by the polymer's solubility in the given solvent, possible intermolecular interactions and the flexibility of the polymer. In the excess of salt, HA's polymer properties are analogous to uncharged polymers in good solvent [100]. It is a highly hydrophilic polymer, which does not form stable intermolecular interactions [100]. Thus, in hydrous buffer solutions, HA adopts a random coil formation governed by its flexibility.

The flexibility of a polymer is characterized by two parameters: the persistence length l_p and the stretched out end-to-end contour length l_c . The persistence length basically describes how much a polymer changes its shape due to thermal forces. Thus it can be expressed by the flexural rigidity EI of the polymer divided by the thermal force $k_B T$ to which it is exposed:

$$l_p = \frac{EI}{k_B T} \quad (3.9)$$

The persistence length can also be defined by the length of a filament 'over which thermal bending becomes appreciable' [101], such that the time average bending decreases exponentially as the arc length s increases [101]:

$$\langle \cos[\Delta\theta_{3D}(s)] \rangle = e^{-s/l_p} \quad (3.10)$$

The overall flexibility of a polymer is categorized into three classes defined by the relation of persistence l_p to contour l_c length: rigid polymers are not bend through thermal forces, with $l_p \ll l_c$, in contrast to flexible polymers, with $l_p \gg l_c$, which

are constantly changing their coiled structure. Many biological polymers, such as actin fibers, fall into the third category of semiflexible polymers with $l_p \sim l_c$.

The reported persistence length of HA varies between 4.5 nm measured with optical tweezers [102] over 7.5 or 6.8 nm determined by size-exclusion chromatography [103] up to 8.7 nm based on small angle neutron scattering [104]. Interestingly the persistence length corresponds roughly to the unit length bound by one hyaladherin link-module. In any case, the persistence length is considerably smaller than the contour length of the long HA chains in the PCC. The HA molecules within the PCC can thus be modeled as a linear flexible polymer in good solvents.

3.4.2 Linear Flexible Polymers in Solution

Another characteristic classification of polymer solution is based on their concentration (fig. 3.23). In dilute solutions, the individual polymer chains do not overlap and the viscosity of the solution is ideally directly proportional to the polymer concentration. The concentration at which the solution volume is filled by polymer coils is termed the

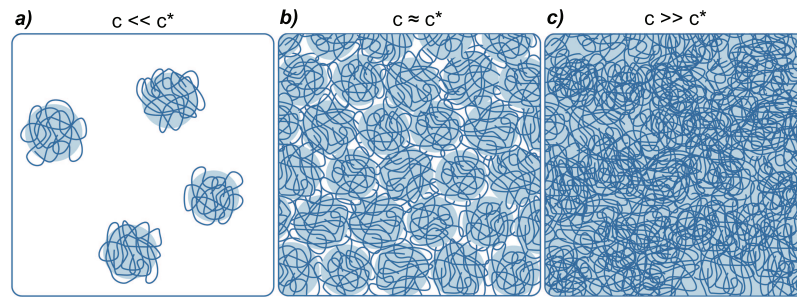


Fig. 3.23 – The three concentration regimes defined for flexible polymers in solution: a) The polymer chains of the individual coils do not overlap in dilute solutions. b) They start to entangle at the overlap concentration c^* in the semi-dilute solution and c) form a concentrated solution at even higher polymer concentrations.

critical overlap concentration c^* :

$$c^*(4\pi/3R_g^3) = M/N_A \quad (3.11)$$

where M/N_A is the mass of each chain, with N_A being the Avogadro's number.

Above this concentration the coils overlap with one another forming a semi-dilute solution in which the polymers start to be entangled. The mobility of the polymer chains is greatly reduced compared to dilute solutions and the thermodynamic properties differ considerably from those of an ideal solution extrapolated to the same concentration [99]. Solutions with even higher concentrations are termed concentrated solutions.

The viscosity of a given dilute polymer solution η can be decoupled from the viscosity of the solvent η_s in dependence of the polymer concentration c by the specific viscosity η_{sp} :

$$\eta_{sp}(c) = \frac{\eta(c) - \eta_s}{\eta_s} \quad (3.12)$$

and can be related to the concentration of the polymer by the Huggins constant k_H and the intrinsic viscosity $[\eta]$ of the polymer:

$$\eta_{sp}(c) = \frac{\eta(c) - \eta_s}{\eta_s} = [\eta]c + k_H([\eta]c)^2 + k_H^2/2!([\eta]c)^3 + (k_H)^3/3!([\eta]c)^4 \quad (3.13)$$

This relation works for homogenous well-behaved dilute HA solutions at very low shear rates with a Huggins constant of 0.34, where the specific viscosity scales with $c^{1.1 \pm 0.2}$ [100].

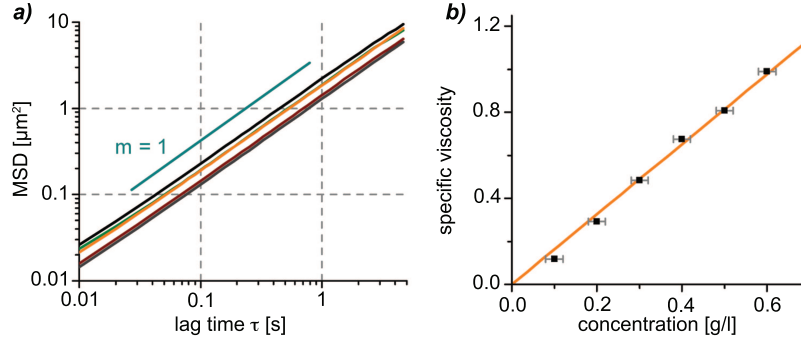


Fig. 3.24 – The specific viscosity of HA scales linearly with the concentration: a) the MSD in HA solution in buffer with a molecular weight of 990 kDa shows a purely viscous behavior up to 0.6 mg/ml. b) The specific viscosity scales linearly with the concentration with an intrinsic viscosity of $1700 \text{ cm}^3/\text{g}$ corresponding to the slope of the orange fit.

The intrinsic viscosity of a polymer can be determined as the slope of the specific viscosity as a function of c :

$$[\eta] \equiv \lim_{c \rightarrow 0} \frac{\eta_{sp}}{c} \quad (3.14)$$

which is related to the length of the HA chain via the Mark-Houwink-Sakurada equation:

$$[\eta] = K(M/(g/mol))^\alpha \quad (3.15)$$

where K is a constant of the unit of l/g and α is called a Mark-Houwink-Sakurada exponent [99]. The constants of high molecular weight hyaluronan have been determined experimentally with $K = 0.029$ and $\alpha = 0.80$ [105]. The expected intrinsic viscosity of HA with a molecular weight of 990 kDa should accordingly be $1815 \text{ cm}^3/\text{g}$. Accordingly, I observed a linear relation between the concentration of monodisperse HA in a dilute buffer solutions and its specific viscosity with an intrinsic viscosity of $1700 \text{ cm}^3/\text{g}$ for 990 kDa HA in control microrheology experiments (fig. 3.24).

3.4.3 Organization of Hyaluronan within the PCC

A key question regarding HA-rich PCC concerns the origin of their extended matrices with thickness' of several micrometers. Although hyaluronan can have extremely long contour lengths of several micrometers, it will form a random coil in solution. The globular conformation adapted by HA molecules in hydrous buffer solution is characterized by its radius of gyration (eq. 3.4.1). It depends on the length of the polymer, which is given by the degree of polymerization i corresponding to the number of monomers in each polymer. If all polymers in solution have a single molecular weight they are monodisperse. However, polymers, especially carbohydrates like HA, are usually polydisperse. Even the largest HA molecule has a radius of gyration in the submicron range (fig. 3.25) related to its molar mass M by [103]:

$$R_g = 2.75 \cdot 10^{-2} \cdot M^{0.596} = [nm] \quad (3.16)$$

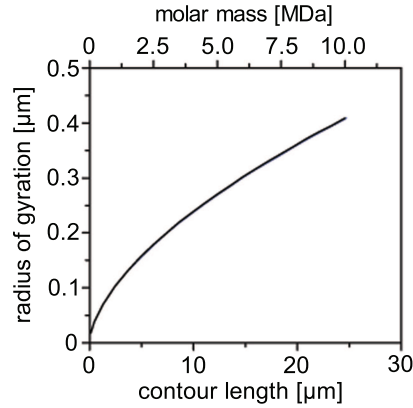


Fig. 3.25 – Correlation of contour length and radius of gyration: Even very large HA molecules of several micrometers in length are coiled up with radii of gyration in the submicron range. The correlation is given by equation 3.16.

The attachment of hyaluronan in their random coil formation to a flat cell membrane would therefore not lead to extended PCCs of several micrometers.

In the literature, three different models have been proposed to explain the formation of PCCs with a thickness of several micrometers: (1) The PCC might consist of multiple layers of crosslinked or entangled hyaluronan [28, 106], or (2) the cell membrane might be extremely rough due to many microvilli [21, 107]. These long membrane protrusions could in turn be enveloped by thinner PCC layers. (3) Most often '*some kind of brush-formation of the hyaluronan chains*' [9] is assumed. Also possible, would be some combination of these mechanisms.

The PCC on Chondrocytes must be Formed by a HA-'Brush'

At first, evidence confirming the multilayer theory was collected: The PCC as part of the cell is a dynamic system that changes with parameter of time. The molecular structure might therefore also be a time dependent process. New hyaluronan could be synthesized constantly leading to entangled HA within the PCC which slowly diffuses into the extra cellular space due to osmotic pressure. As it is highly unlikely that HA is able to diffuse back through the PCC towards the cell, HA contained in the media can not be degraded. If this picture was correct an increasing amount of HA should be present in the supernatant of the growing cells. As the RCJ-P cells grow exponentially with generation doubling times of about 6 h, the concentration should not increase accordingly with time. However, fluorophore-assisted carbohydrate electrophoresis (FACE) measurements performed in cooperation with *Prof. Sleeman*, Forschungszentrum Karlsruhe, show very low concentrations of free hyaluronan in solution, which do not increase significantly over time (table 3.2).

Hence, a multilayer of hyaluronan would need to be stabilized by some kind of cross-links. This can generally be achieved by crosslinking hyaladherins (chapter 1.2.2), which have been identified in the coat enveloping oocytes for example [108] or during inflammation processes (chapter 1.1), but not in the PCC of chondrocytes. Therefore, we expect all hyaluronan within the PCC on RCJ-P cells to be directly attached to the cell membrane forming a grafted polymer layer.

Recent experimental data by *Kulti et al.* show a significant increase of microvillis on cells overexpressing hyaluronan synthase leading to 'hedgehog' cells [107]. They have also successfully shown a higher percentage of microvillis on cells with extended

Table 3.2 – **Free HA concentration** in supernatant of cell culture flask measured with FACE by *Melanie Roth* (Forschungszentrum Karlsruhe, *Prof. Sleeman*):

time [h] after seeding in culture flask	HA conc. [$\mu\text{g}/\text{ml}$] determined with FACE
24	13
24	17
48	17
48	17
72	27
72	27

PCCs [21]. Thus implicating an important impact of the PCC on the structure of the cell membrane or vice versa.

In summary, only small microvilli have been observed (chapter 3.2.2) that would not suffice for the formation of extended PCCs, but might enhance its stability or its growth by an enlarged attachment surface. The multi layer model seems to be unlikely for this special kind of cells, while it plays an important role for the coat of other cell types such as oocytes. As the radius of gyration of hyaluronan is a lot smaller than the observed PCC thickness, some kind of 'brush-like' grafted polymer structure is expected. A brush-like formation implies a scenario in which grafted HA polymers are stretched out to a considerably larger extend than their native radius of gyration. Stretching of polymer chains leads to a loss of entropy, which needs to be balanced in order to obtain stretched HA molecules. The first and most commonly proposed model is that the grafting density of HA on the cell surface is high enough so the HA molecules are stretched out away from the membrane considerably more than their native radius of gyration due to the energy gained during the attachment. We were able to demonstrate this possibility on model systems of the PCC (chapter 3.4.4). Even higher grafting densities could be accessible by forceful extrusion of new HA chains into the preformed brush. Thus it has been suggested that hyaluronan synthases within the cell membrane extruding new chains into the PCC might facilitate stretching of the chains [?]. Recent theoretical work [109] showed that impressive molecular extension of HA may occur even with small numbers of attached proteins, which change the local stiffness of the hyaluronan chain at their binding site. Such stretching could also lead to a brush-like structure of HA at the cell surface or at least facilitate its formation.

3.4.4 A Brush-like Structure could be Observed in Model Systems

Ralf P. Richter, University of Heidelberg, developed a model system of the PCC based on end-grafted hyaluronan molecules [110]. First, he formed a streptavidin monolayer to which biotinylated HA molecules were bound (fig. 3.26). The streptavidin layer consists of a supported lipid bilayer (SLB) [111] doped with biotinylated lipids on glass or mica surfaces. Different concentrations of streptavidin can subsequently be bound to this biotinylated SLB. The employed hyaluronan molecules are biotinylated specifically at one end. Thus they are strongly bound to the surface, where the binding energy should be sufficient to form a polymer brush with stretched out HA molecules.

In order to measure the height of these thin hydrated HA films, we set up a special reflection interference contrast microscope (RICM), that simultaneously measures

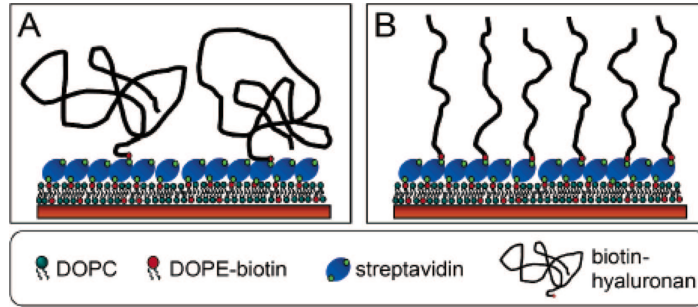


Fig. 3.26 – Model systems of the PCC with grafted HA: First supported lipid membranes with dioleoylphosphatidylcholine (DOPC) lipids and biotinylated dioleoylphosphatidylethanolamine (DOPE) lipids are formed on glass and mica surfaces. After addition of streptavidin, brushes can be formed with biotinylated HA. Adapted from fig. 1 [110].

the interference for three different wavelengths (3λ -RICM, chapter 5.1.3). Spherical polystyrene beads ($20\ \mu\text{m}$ diameter) were placed on top of the formed films. The interference pattern of these beads in RICM depends on their distance to the underlying glass slide. However, standard RICM setups only lead to relative distances dependent on the employed wavelength. The absolute distance can be determined for thin films by correlating the relative distance of the same particle measured with two different wavelengths [112]. The simultaneous visualization of the interference pattern of one particle at three different wavelength enables the precise determination of even thicker surface layers (fig. 3.27).

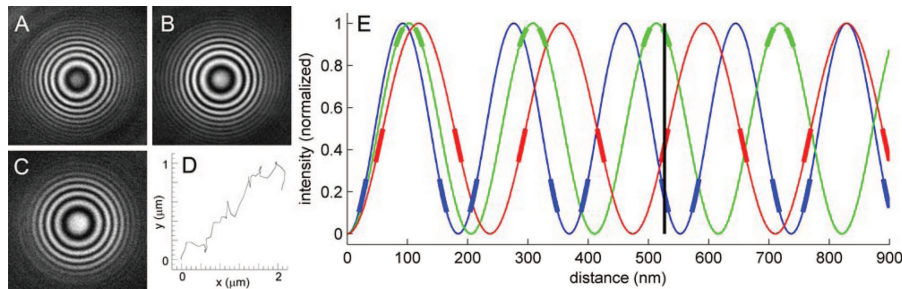


Fig. 3.27 – Determination of HA film heights with 3λ -RICM: The relative height of films adsorbed to glass surfaces can be determined with reflection interference microscopy (RICM) of polystyrene beads. Comparison of the interference pattern of the same bead imaged at 490 nm (A), 546 nm (B) and 630 nm (C) enables an absolute height determination. (D) The beads are not bound to the film as evident by the in-plane motion over 25 s. (E) The normalized intensity in the center of the bead changes sinusoidal with the distance to the glass surface. The expected normalized intensities depend on the wavelength (thin lines in blue (490 nm), green (546 nm) and red (630 nm)). The absolute film height corresponds to the unique overlay (black vertical line at 510 nm) of all three possible distances (bold curve segments). Adapted from supplemental information to [110].

HA of different lengths formed films with thickness considerably larger than their native radii of gyration (table 3.3). Thus we were able to show that hyaluronan

molecules can form an extended brush if they are grafted to the surface by a strong bond.

Table 3.3 – End-grafted HA can form extended films: The observed film thickness t_{HA} is considerably larger than their native radii of gyration R_g , but smaller than their contour length l_c .

	M_w [kDa]	l_c [nm]	R_g [nm]	t_{HA} [nm]
HA50	58	155	15	140 ± 10
HA1000	1028	2891	88	580 ± 20

This effect was especially evident for short HA molecules. The equilibrium structure of larger molecules is experimentally not accessible, as the long chains need to diffuse through the formed layer in order to attach to the substrate. In contrast to this scenario, the HA is synthesized into the PCC by hyaluronan synthases on cell membranes.

3.4.5 Polymer Theory for Endgrafted, Monodisperse Polymers

If HA was attached at one end only to the membrane, this can be described by the polymer theory for end-grafted flexible polymers in good solvents [113]. The buffer in which the HA is observed, not only serves as a good solvent for the hydrophilic HA, it also effectively neutralizes the charged HA. HA can thus be modeled as a neutral flexible polymer as discussed before. Since HA does not bind to the cell membrane, but only to specific receptors further interactions can be neglected. This scenario corresponds to end-grafted polymers bond to specific binding sites on a grafting layer with a neglectable net attraction as used in the Alexander - de Gennes's grafting theory [113]. The density of binding sites is termed the grafting density σ . In equilibrium, this parameter determines the number of polymers bound to a certain area.

If only few polymers are bound to a given surface with distances much larger than their radius of gyration, the polymer are attached to the surface in their native coiled form. At higher concentrations the coils will start to touch each other and thus completely cover the surface with coils of polymers. The grafting density for this 'mushroom' structure is directly related to the radius of gyration, as the distance between the grafting point equals the diameter of one coil, equal to $2R_g$. With gyration radii in the submicron range, such a mushroom structure would not lead to extended PCCs as observed on chondrocytes.

At larger grafting densities, the chains start to overlap. Thus they are stretched out and form a polymer brush. Independent of the chemical structure of the polymer, all flexible polymers in good solvent follow the same scaling laws. The scaling concept introduced by *Alexander* [114] treats the chains as linear arrays of N' blobs (fig. 3.28). The number of blobs in a given polymer is related to the number of monomers N in each blob n_{blob} by $N' = N/n_{blob}$. The number of monomers in a blob is related to the screening length ξ , which is related to the average distance between grafting points in the Alexander-deGennes model, leading to $\xi = \sigma^{1/2}$.

This yields a scaling law relating the brush height h to the grafting density σ and the length of the polymer:

$$h \propto \sigma^{(1/\nu-1)/2} N \approx \sigma^{1/3} N \quad (3.17)$$

Realistically, this structure is much too regular, and entropy favors a non-uniform blob picture. This is modeled by an increasing blob size, taking into account that polymers turn backwards with chain ends anywhere within the brush. According to the

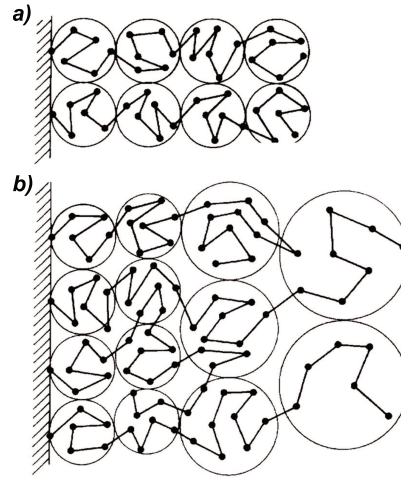


Fig. 3.28 – Polymer brushes scale with the height of the layer: a) Blob model of polymer brushes with constant blob sizes following the *Alexander-deGennes* model. b) Parabolic density profile of polymer brushes with blobs of increasing size following the *Witten-Milner-Cates* theory. Images courtesy of *Prof. Binder* as in [113].

Witten-Milner-Cates theory a parabolic concentration profile should be observed within the polymer brush [115].

$$\phi(z) = \phi(0)[1 - (z/h)^2] \quad (3.18)$$

Generally, HA is able to form polymer brushes, as some stretching of hyaluronan molecules has been seen in the model systems described in chapter 3.4.4. In these systems biotinylated HA was allowed to bind to streptavidin on biotinylated supported lipid membranes forming an end-grafted polymer brush.

Correlating this polymer theory to the PCC shows similar features of the HA bound to the cell membrane: Hyaluronan is synthesized directly on the cell surface by transmembrane HA synthases (chapter 1.2.1), which can bind the end of the HA chain and thus attach it to the cell surface. If the HA concentration was high enough, it would stretch out to form a brush. As HA loses entropic energy as it is stretched out, energy is required to pack the HA chains densely. This energy could be provided by the binding energy to the grafting points, e.g. the binding affinity of HA synthases. Additionally, HA synthases extruding the chains into the PCC could produce the required extrusion force [?] to facilitate stretching of the chains. Such an end-grafted HA-brush might be formed in the hedgehog cells induced by overexpression of HA synthase2 [?]. Additionally, hyaladherins might play a vital role in such a brush-formation, as especially aggrecan has been proposed to stretch HA [109].

3.4.6 Side-On Grafting Leads to Concentration Profiles which are More Closely Related to the Observed Profiles

Grafting of polymers at the middle of the chain is highly unlikely in most polymer physics scenarios, where either the full polymer is adsorbed at an interface or build-up on the surface by e.g. radical chain reactions [116]. However, HA is not only attached at its end to hyaluronan synthases (fig. 3.29a, b). It is also attached to the membrane by different receptors, such as CD44 binding within the HA chain (fig. 3.29c).

The side-on attachment effectively leads to an end-grafted polymer-brush with an extreme polydispersity. If all HA molecules were attached only to one HA receptors anywhere within the chain, a continuous size distribution would be observed, which

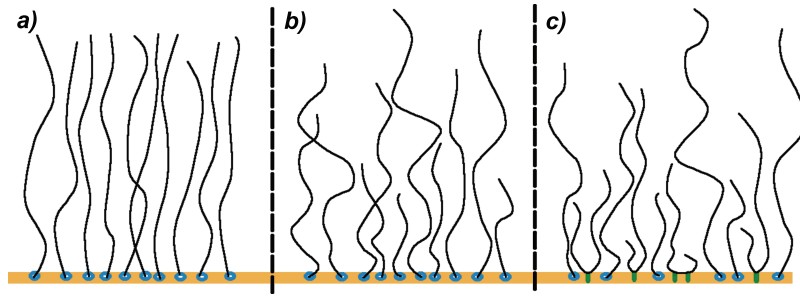


Fig. 3.29 – HA does not form a simple polymer brush: a) If the grafting density is high enough, flexible polymers form polymer brushes, which can be described by polymer physics theories. b) In contrast to these theories, HA is not monodisperse in size and c) side on attachment leads to an additional polydispersity.

would lead to a linear decreasing concentration profile if constant blob sizes were assumed following the *Alexander-deGenne* model (fig. 3.30).

If the HA molecules interact with more than one receptor or are additionally attached at a synthase the concentration profile follows a more complex function, that can not be described with a linear or an exponential fit (fig. 3.31).

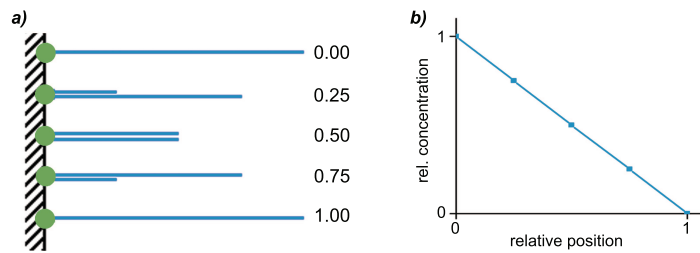


Fig. 3.30 – Single side on attachment of HA chains leads to a linear gradient if the blob size is kept constant following the Alexander-deGennes model.

Possible Scenarios for Brush-Formations of HA-Chains

The PCC formation is further complicated by HA-binding proteins attaching to the HA chain after HA has been synthesized at the cell membrane and extruded into the PCC. If the emerging HA was immediately bound to its receptors, the first chains should interact with as many receptors as possible tightly covering the surface and blocking the receptors for subsequently synthesised HA (fig. 3.32b). However, if hyaladherins like aggrecan bind to the emerging chains, before they attach to a receptor, the chain would be stiffened [109] and unable for some length to bind to a receptor. The ability of HA to bind to a receptor in this scenario would depend on the presence of hyaladherins and receptors, which might both be regulated by the cell as well as on the presence of other HA chains. This would underline the need of hyaladherins like aggrecan or versican not only for reconstituted but even more for freshly formed pericellular matrices. However, so far it has not been possible to label aggrecan on the PCC of living cells without significant alterations of the PCC.

If hyaluronan in the PCC was covered homogeneously with hyaladherins like aggrecan, where their attachment ensures further stretching of the chains [109], the HA distribution could still be described by the same models. The only difference would

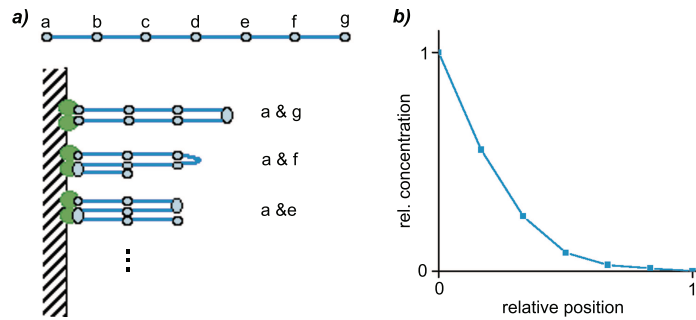


Fig. 3.31 – Multiple HA grafting points lead to faster decreasing concentration profiles. The profile was calculated numerically by assuming seven possible grafting points (termed a-g) and calculating the length of each chain part. Thus the first example grafted at point a and g would lead to a length of 0.5 of both chain parts. The profile corresponds to the histogram of obtained chain lengths.

be found in the stiffness of the hyaluronan, which would ease the brush formation (fig. 3.32a).

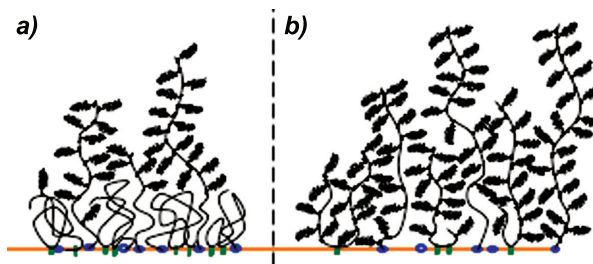


Fig. 3.32 – Aggrecan is an ubiquitous hyaladherin in cartilage which could stretch out HA to form a brush-like structure. a) If HA was synthesized (blue dots) in the presence of many HA receptors (green elipsoids) on the surface without stiffening hyaladherins, a dense HA layer might be formed close to the cell membrane through which less bound HA molecules are extruded decorated with aggrecan molecules. b) The distribution profile of homogeneously aggrecan labeled HA should correspond to the scenario described above.

In conclusion, the observed HA distribution profiles and the micromechanical map of the PCC could be explained by multiple side on attachment of hyaluronan forming a brush on the cell surface. Where the entropic energy required for the brush formation could be provided by the binding energy to HA receptors, possibly in a polyvalent fashion and the HA synthase. Additional energy could be provided by the extrusion forces of the synthases and HA stretching of hyaladherins.

3.5 Correlating the Micromechanical Profile to the HA Distribution Profile

The measured profiles can be compared with a relative coordinate system. This has been realized by the previously introduced relative position, determined by a third independent technique, the particle exclusion assay.

The GFPn intensity should be directly related to the HA concentration, or to be more precise, to the concentration of HA units required to bind one GFPn molecule. In solution, an increasing concentration of HA leads to an increase in viscoelasticities. Similarly, the HA concentration within the PCC should be related to its viscoelasticity. The probing time scale of our experiments corresponds to the Rouse model of polymers. In a semidilute solution the modulus G on this time scale is directly proportional to the concentration c . This relation has been shown to hold true for hyaluronan and aggrecan solutions over a wide range [105,117]. However, above the critical concentration, in the entanglement regime, the modulus scales no longer with c , but with $c^{1.5}$ [118].

In order to determine the relation between the concentration and the viscoelasticity, $1/\text{MSD}$ can be plotted in the same relative coordinate system as the GFPn intensity (fig. 3.33).

Except for the MSD values very close to the cell membrane, the micromechanical map corresponds very well to the hyaluronan distribution. Close to the cell membrane, the diffusive exponent approaches the value of the gel point at which the polymers are entangled (compare chapter 3.3.1). Whether this entanglement is caused by grafting the polymers to a surface or related to a concentration above the critical entanglement concentration, it will in both cases influence the scaling of the MSD, which might rather scale with $c^{1.5}$ close to the cell membrane.

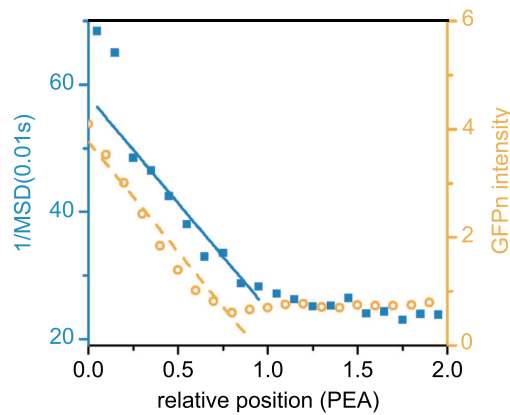


Fig. 3.33 – The polymer concentration is inversely related to the MSD: The profile of the GFPn intensity correlates with the $1/\text{MSD}$. The different profiles can be compared via the relative position via defined by the PEA.

Comparison of the measurements close to the PCC edge shows slight deviations. The GFPn indicates a smaller PCC compared to the PEA. This can be explained by the resolution limit prohibiting the distinction between the small amounts of GFPn on the PCC fringe against the noise level. The GFPn staining therefore does not yield information about the edge of the PCC. Micro-rheology measurements on the other hand are very sensitive to slight variations in viscoelasticity. They seem to indicate a somewhat larger PCC than the PEA. The PEA defines the edge of the PCC by the ability of red blood cells to approach the cell. They are stopped at a distance where the PCC forms an impenetrable barrier to them. Due to the gradient nature of this

barrier the red blood cells might be able to penetrate or squeeze the outer fringes of the PCC. This PEA defined edge will be reproducible, but somewhat smaller than that measurable by the more sensitive passive microrheology technique.

Comparison of the GFPn intensity with $1/\text{MSD}$ shows that both data sets can be fitted linearly or by an exponentially decreasing function. Generally, such density profiles of grafted polymers can be related to their structure, whereas the molecular architecture of the PCC will be defined by HA's polymer physics, its grafting mode and modifications by hyaluronan binding proteins.

The experimental results discussed earlier in this chapter showed, that the PCC is based on some kind of 'brush formation' of the HA chain, implying grafted HA polymers which are stretched out to considerably more than their native radius of gyration. The different models for the organization of HA molecules predicted by polymer physics, their expected distribution profiles and the relation to the experimentally observed profiles are discussed in this section.

However, our observed density decrease, if fitted linearly or exponentially, does not follow the predicted parabolic concentration profile for monodisperse, end-grafted polymers [115]. In contrast to these theories, the biological organization of hyaluronan molecules within the PCC is far more complex. HA is most likely not monodisperse as hyaluronan synthases produce hyaluronan with a certain length range (chapter 1.2.1). They are not just attached at the end of the chain, as surface receptors such as CD44 bind HA anywhere within the chain (chapter 1.2.2). Additionally, as mentioned above, hyaluronan-binding proteins might change HA's polymer properties. Thus it is truly remarkable that such a dynamic system shows reproducible profiles within our observation time window.

3.5.1 Conclusion and Outlook

Two independent techniques for characterizing the pericellular coat on living cells were presented. Hyaluronan distribution profiles were obtainable with GFPn in spinning disk microscopy. The micromechanical structure was measured unobtrusively with passive particle-tracking microrheology. The two profiles can be correlated by defining the relative position of the PCC via PEA, a third independent method. Thus it can be shown that the two profiles agree very well with one another. The hyaluronan concentration gradient and mechanical properties observed might play an unconsidered role in the mechanical interactions with the extra-cellular matrix or other cells. Theoretical models have provided evidence of dramatic effects on the local stress-strain and fluid flow environment of chondrocytes [83]. It would be interesting to see, if these predictions were influenced by a density gradient in contrast to homogeneous mechanical properties. As both techniques are independent of the changes in the cell's mechanics, they present the tools so far lacking for comparison of PCCs, as required for understanding the effects of drugs or hyaluronan-binding-proteins on the PCC as well as the alterations in osteoarthritic or aged cells.

Chapter 4

Regulating PCC Expression by Controlled Integrin Activation

Naturally, chondrocytes are embedded with their pericellular coat (PCC) in the extracellular matrix (ECM) of the articular cartilage. Changes of its composition and integrity are a central feature in most forms of arthritis. Additionally, the ECM plays an active role in many cell processes. Thus interactions with both the PCC and the ECM are of vital importance for chondrocytes. One of the most important ECM-receptors located in the outer membrane of chondrocytes is integrin. Many types of integrins can be activated by a short RGD sequence located in fibronectin, collagen and many other ECM components alike.

The cross-talk between the ECM and the PCC on chondrocytes can be studied in adhesion experiments on differently coated substrates. Activation of integrins influences the adhesion area of cells, as well as the size of the PCC. Interestingly, they are not related, but their ratio is directly related to the growth rate. In order to control the integrin activation more precisely than by different ECM protein coatings of the substrate, adhesive nanostructured surfaces are employed. The density of presented integrin activating RGD ligands can be controlled by the spacing of quasi-hexagonally arranged gold anchorpoints on an otherwise inert background.

Preliminary experiments on these adhesive nanostructured surfaces showed significant differences of adhesion area, motility and PCC size on surfaces with different spacings. However, so far the spacing was varied over large ranges by the choice of the polymer. This approach also changes the size of the gold particle which could influence the interaction potential. Within this work, two different approaches are explored, which enable the variation of the interparticle spacing over a wide range with the same polymer. Additionally, the technique was improved to ensure homogenous nanostructured surfaces over large areas after establishing the required protocols to measure and compare the geometrical and translational order over large areas.

4.1 Integrin Activation Influences Cell Behaviour

Articular cartilage consist of the extracellular matrix (ECM) and the embedded chondrocytes with their PCCs. Thus the physical properties of cartilage are mainly goverend by the ECM, maintained by the chondrocytes. Changes of the ECM's composition and integrity are a central feature in most forms of arthritis [119]. They will not only induce mechanical changes, but may also affect the chondrocytes, as the ECM plays an active role in regulating cell behavior. ECM controlled cell activities include for example cell migration and proliferation, but also processes important for morphogenesis, cell survival or repair [120]. Changes in the ECM in osteoarthritic cells lead to enlarged PCCs [121] and reduced proliferation rates [122]; or the changes in the ECM, the PCC and the proliferation rate could all be unrelated symptoms.

The ECM is not scaffolded by carbohydrates, but consists of different proteins, namely fibronectin, laminin or collagen. This difference is reflected by the different types of transmembrane receptors responsible for the interaction either with the PCC or the ECM. Interactions with the PCC are mediated by HA specific carbohydrate-protein receptors like CD44 (chapter ??). Whereas, all of the ECM components interact via specific protein-protein receptors, mainly integrins. These transmembrane proteins consist of two non-covalently associated subunits. So far 18 so called α -subunits and 8 β -subunits have been identified, adding up to different heterodimers with different ligand specificities [1, 123].

4.1.1 Advantages of Peptides in Adhesion Studies

The cross-talk between the ECM and the PCC can be analyzed with adhesion studies on surfaces coated with ECM components. The surfaces employed in such adhesion studies can be functionalized either with whole proteins or peptides. Where proteins offer the full range of possible interaction sites, they have the disadvantage, that they are stochastically arranged during the immobilization process and thus only partially accessible. Proteins are also harder to employ in medical scenarios as they need to be purified from organism, which can cause undesired immune responses or increase infection risks. Alternatively, peptides presenting a specific recognition motif can be immobilized specifically. They can also selectively address one particular type of cell adhesion receptors.

Whereas linear peptides are slowly degraded even *in vivo* [124, 125] cyclic derivatives exhibit excellent long time stability [125–127] and are thus preferable.

RGD (arginin-glycine-aspartate) was the first peptide sequence found to promote cell-adhesion [128]. It has proven to serve as a useful tool to stimulate cell adhesion on various materials in different applications and variations since then [129]. RGD interacts specifically with integrins and is not only one of the adhesion sites in fibronectin (fig. 4.3) [130], but also in many other ECM proteins, including vitronectin, bibrinogen, collagen, laminin, osteopontin, tenascin and others [131]. About 12 integrins have been shown to bind to ECM molecules in a RGD dependent manner [131].

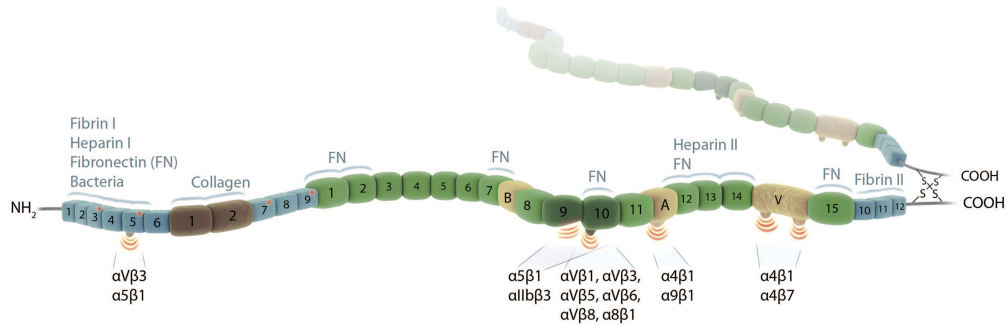


Fig. 4.1 – Fibronectin has several interaction sites: The three different modules (type I, blue; type II, brown, type III, green) are symmetric on both strands of the dimer. The RGD motif is located in the 10th type III domain. Image courtesy by *Prof. Faessler* as fig. 1 in [130]

Similar to the presentation of the RGD sequence in an exposed loop of a protein, the RGD peptide must be accessible by the binding site of the integrin, if it is immobilized on an artificial surface. Therefore a minimum spacing between the RGD sequence and the anchoring moiety of 4.6 or 3.5 nm is required [132,133] even though the experimental data available so far does not lead to a uniform theory to explain the need for a spacer [129]. If the spacer length is too long, on the other hand, a reduced cell attachment is observed [132]. This is not only caused by an increasing entropy, but also because cells seem to prefer a tight binding to more rigid surfaces [129].

Chondrocytes attach to fibronectin, collagen type II and VI, vitronectin and osteopontin in an RGD dependent manner [134,135]. This could be shown by adhesion assays in the presence of RGD. The adhesion was inhibited >80-90% to fibronectin, vitronectin and osteopontin by a linear RGD peptide [134]. Collagen type II and VI adhesion could be inhibited by a cyclic RGD [135].

In order to precisely control the interaction of cells with their extracellular environment nanostructured surfaces developed by *Spatz et al.* were employed (chapter 4.1.3). They allow the immobilization of peptides at defined spacings on an otherwise protein resistant surface. Therefore glass surfaces are first partially decorated with gold particles of defined size and in a defined spacing described in more detail in the following chapter and subsequently coated with a special poly(ethylenglycol) (PEG) layer that covalently binds only to the glass. This PEG passivation layer prevents adsorption of proteins [136] and thus inhibits adhesion of cells, where the non-structured area of the surface serves as an internal control to judge the quality of the passivation. The height of the hydrated PEG layer is estimated to be 5.0 ± 0.7 nm [136]. The gold particles of about 7 to 8 nm [137] are still freely addressable by thiolated peptides.

In this work a cyclic RGD derivative was employed to study integrin activation. It can be immobilized on the gold dots via its thiolated linker on the end of the 2 nm spacer and was kindly provided by *Prof. Kessler*, TU Muenchen. Thus nanopatterned adhesive interfaces (fig. 4.2) for the activation of integrin functions can be created [138–140].

4.1.2 The PCC can be Controlled with Adhesion Receptors

In this part of the work the integrin-mediated interactions of cells is analyzed in adhesion studies. The influence on the adhesion area, the size of the PCC and the impact on the growth of RCJ-P cells is measured. At first, we analyzed the behaviour of

the cells on different surfaces functionalized homogeneously with different proteins and peptides. Thereby we could show that there is a direct relationship between the ratio of the adhesion area, the type of surface and the growth rate.

The adhesion of cells were compared on two different non-modified surfaces: glass and gold-coated surfaces. Both surfaces do not present any interaction points towards the cells. Thus the cells express their own adhesion proteins, which physisorb in different amounts to the substrates depending on the materials properties.

In addition, the cells were observed on glass surfaces coated with the ECM proteins collagen and fibronectin and on gold coated surfaces with the integrin activating RGD peptides. The adhesion area depends on the type of the surface coating: Glass and gold surfaces, which both present no integrin activating signals themselves, show similar adhesion areas. The adhesion areas observed on protein coated surfaces is significantly larger. Fibronectin coated surfaces induce the largest adhesion areas, followed directly by collagen coated surfaces. RGD coated surfaces show about the same adhesion area, as the unfunctionalized gold surface.

However, if the size of the PCC is also measured, it becomes evident, that the adhesion signals of the pure gold surface and the RGD modified surface are not the same: the PCC is considerably smaller on the RGD coated surface (fig. 4.3a). Assuming a round cell shape, the thickness of the PCC can be calculated based on the measured adhesion and PCC area (fig. 4.3b). The PCC shows about the same thickness on RGD coated surfaces and unfunctionalized surfaces, but is significantly larger on the other surfaces. Thus the adhesion area is not directly related to the thickness of the PCC.

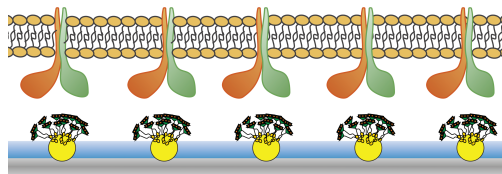


Fig. 4.2 – Schematic drawing of the employed nanostructured surfaces to control integrin activation: A cyclic arginin-glycine-aspartate (RGD) peptide is covalently bound with its thiol group to the gold particles of the partly nanostructured surface. Unspecific adsorption of proteins and cells is prevented by poly(ethylenglycol) (PEG, blue layer) covalently bound to the whole glass slide. The size of the integrins (red and green subunit) ensures that one gold particle cannot interact with more than one integrin.

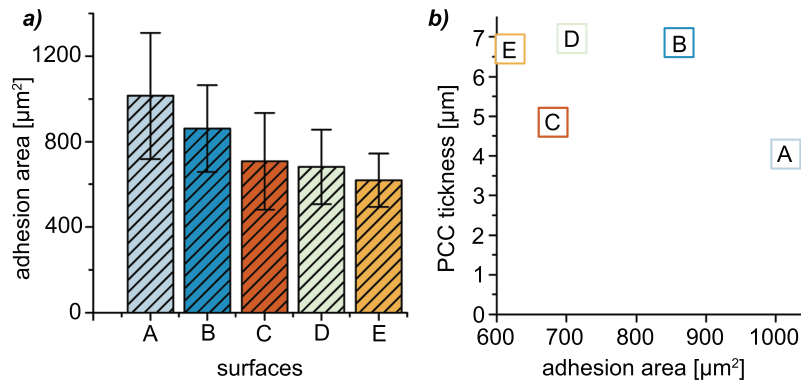


Fig. 4.3 – Influence of the different surfaces: The adhesion area strongly depends on the employed surface. a) The largest adhesion area is found on fibronectin coated surfaces (A, light blue), followed by collagen coated surfaces (B, dark blue). The adhesion area of RGD functionalized (C, red) and unfunctionalized gold surfaces (D, light green) and glass slides (E, orange) is about the same. b) However, the adhesion area is not correlated to the PCC thickness.

The ratio of the PCC area to the adhesion area varies between 0.60 to 1.14 on the different surfaces. It is similar for cells adhered to collagen and fibronectin coated surfaces as well as on unfunctionalised gold surfaces. Cells on these surfaces also show similar proliferation rates. Interestingly, the population doubling time, characterizing the proliferation rate is directly proportional to the ratio of the PCC to adhesion area (fig. 4.4). Thus cells with larger PCC to adhesion area ratios, as observed for example on glass slides, proliferate faster, than cells with lower ratios, as expressed on RGD functionalized surfaces.

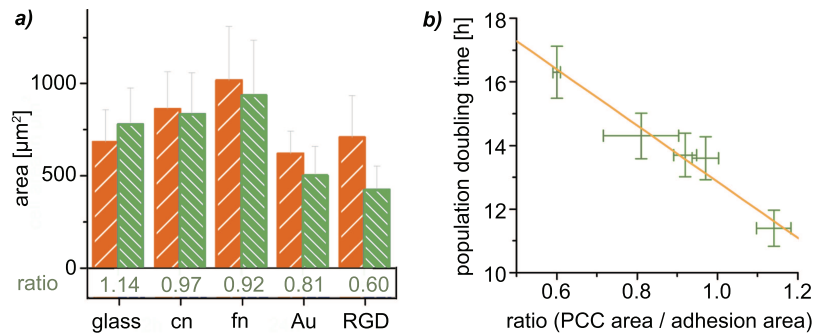


Fig. 4.4 – The ratio between PCC and adhesion area is correlated to the growth rate: a) The adhesion area (red, ascending large stripes) is not correlated to the PCC area (green, descending dense stripes) on glass surfaces, collagen (cn) or fibronectin (fn) coated glass slides, or on gold (Au) surfaces and RGD-labelled gold surfaces. The ratio is determined by the PCC area vs. the adhesion area on fixed RCJ-P cells. b) This ratio is directly related to the growth rate of the cells given by the population doubling time.

The different surfaces activate integrins in a different manner and possibly with a different density. The concentration of the RGD motif is highest on the gold surfaces functionalized with RGD peptides, as the proteins preadsorbed to the surfaces or produced by the cells contain a high amount of other amino acid sequences as well. The influence of the protein concentration on the integrin activation was first checked by surfaces coated with different amounts of fibronectin. The uncoated surface was further filled with bovine serum albumin (BSA) to prevent unspecific adsorption of proteins secreted by the cells (surfaces were kindly provided by *Vamsi Kodali*, Georgia Tech., USA).

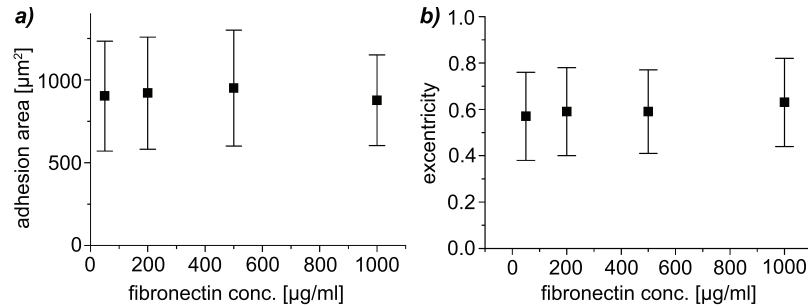


Fig. 4.5 – Adhesion areas as well as the cell’s eccentricity do not change with different fibronectin concentrations: a) Cells adhered on glass surfaces prepared with different amounts of fibronectin show gaussian distributions of the adhesion area with no significant differences (averaged over at least 70 cells per sample). b) The eccentricity of the cells defined as the ratio of minor to major axis of the fitted ellipsoid also show now significant differences. Error bars depict the standard deviations.

Comparison of cells adhered to fibronectin with original concentrations of 1 mg/ml down to 50 $\mu\text{g/ml}$ showed no significant difference in adhesion area or shape. The general shape of the cells is distinguished by fitting an ellipse to each cell characterized by the minor and major axis. The ratio of minor to major axis gives a feeling for the ellipticity, where one corresponds to a perfect circle and zero to a straight line (fig. 4.5).

Integrin activation can be controlled more precisely by the adhesive nanostructured surfaces. Therefore, the measurement procedures was established first to determine the changes induced by the altered integrin activations.

4.1.3 Analyzing Integrin Activation Induced Changes on Chondrocytes

Activation of integrins might trigger a multitude of different responses. Obviously the adhesion itself might depend on the density and geometrical arrangement of RGD motives. The adhesion of cells to a certain substrate can generally be judged by multiple factors: the adhesion area defined as the cell membrane area attached to the substrate [141], the cell shape, the cell’s motility [142] or on a more detailed level by the size and shape of focal adhesions [143] or the expression of proteins involved in focal contact formations. Apart from these adhesion induced changes, it was interesting to see if the PCC was also affected by a different amount of integrin activation. Therefore 3D PEAs were performed and the PCC was stained with GFPn. In order to compare the cells on the different nanostructured surfaces ensuring the same amount of GFPn and bleaching conditions, special substrates were prepared. Nearly half the surface was covered with gold particles at an average spacing of 57 nm and the other with a spacing

of 74 nm leaving a small stripe of unstructured area in between to control the quality of the passivation layer.

The motility of cells is characterized by two different time scales: The motion of the complete cell over the surface and the motion of cell membrane protrusions where the cell's main position is not significantly changed. The first motion is observable on the time scale of minutes, whereas the second 'exploratory' motion takes place in the time scale of seconds.

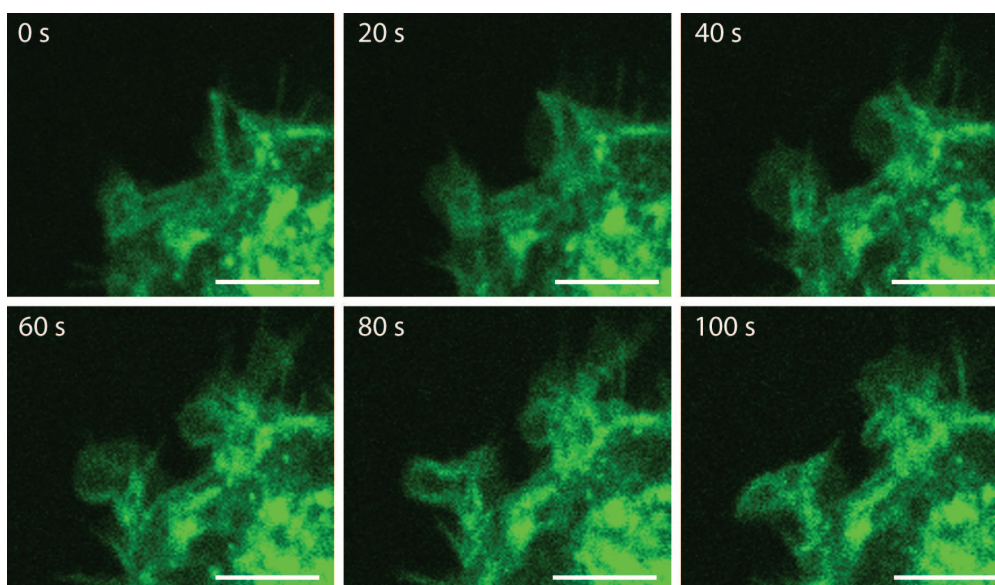


Fig. 4.6 – Membrane protrusions on cells adhered to nanopatterns with 57 nm spacing are stable on short time scales: Example of the typical motion of cell protrusions after an adhesion time of 24 h. The cell membrane was stained with WGA488 (green), which is also staining internal membrane enclosed compartments. The scale bars correspond to 5 μm .

Cells adhered to 57 nm spaced nanopatterned surfaces show nearly no movements of cell protrusions within 100 s (fig. 4.6). Cells adhered to the 74 nm spaced nanopattern on the other hand, not only form longer cell protrusions, but they also constantly probe the surface in their close proximity showing fast dynamic changes of their membrane edges (fig. 4.7).

Whereas it is very difficult to conclude anything about the adhesion area on these surfaces, the size of the PCC is clearly correlated to the spacing of the nanostructures. Thus the GFPn staining comparing cells on the 57 nm spacing with the 74 nm spacing on one substrates shows markedly stronger fluorescence on the larger interparticle distances (fig. 4.8).

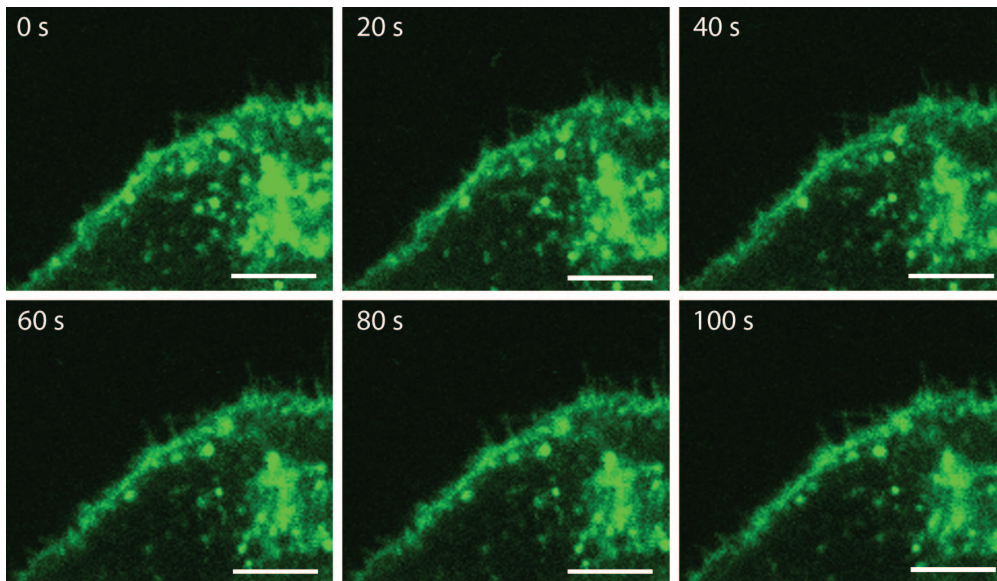


Fig. 4.7 – Membrane protrusions on cells adhered to nanopatterns with 74 nm spacing are dynamic on short time scales: Example of the typical motion of cell protrusions after an adhesion time of 24 h. The cell membrane was stained with WGA488 (green). The scale bars correspond to 5 μm .

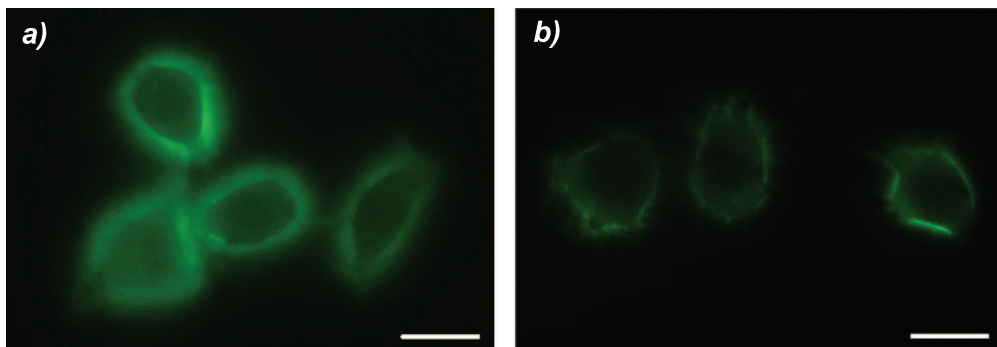


Fig. 4.8 – The thickness of the PCC seems to depend on the amount of integrin activation: Fluorescence microscopy images of GFPn staining (green) indicate thinner PCCs on nanostructures with an average spacing of 57 nm (a) between the gold particles than with 74 nm average spacings (b). Scale bars correspond to 20 μm .

3D particle exclusion assay additionally varifiy, that the PCC is larger at the apical side of the cells (fig. 4.9).

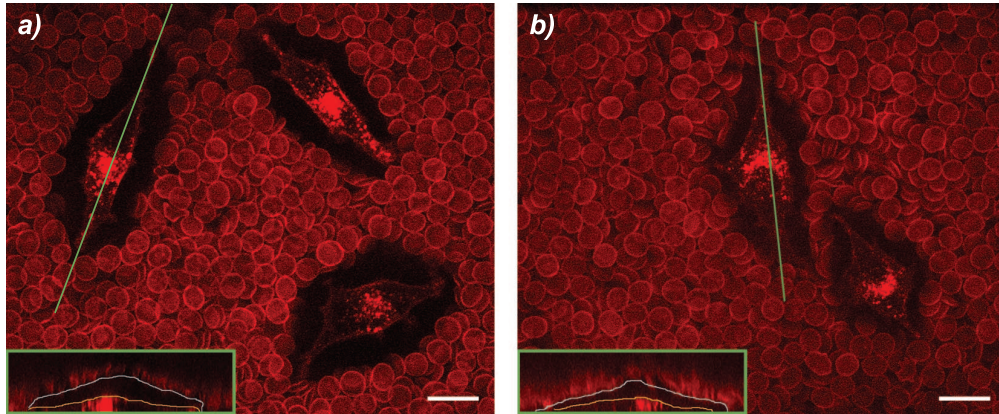


Fig. 4.9 – The thickness of the PCC seems to depend on the amount of integrin activation: PEAs with fluorescently marked erythrocytes and RCJ-P cells show that the PCC is not only smaller around the cell in 2 dimensions, but also on top of the cell. The cells have been compared on adhesive surfaces with interparticle distances of 74 nm (a) or 57 nm (b) after 12 h. The insets show z-projections with outlined cell surfaces (orange) and PCC edges (blue) marked by the PEA.

Statistical analysis of the cell surface area in particular lead to very inconsistent results, showing large deviations between different samples and even between different areas of the surface. Thus the adhesion area tended to be larger closer to the dipping line. These inconsistencies could be related to the production of the nanostructured surfaces. Instead of continuing with the cell experiments, I therefore first optimized the characterization methods of the nanostructured surfaces and subsequently their production described in detail in the next chapters.

4.2 Block-Copolymer Micellar Nanolithography

The nanostructured surfaces developed by [144–146] present an ideal platform to study the interaction of cells with specific receptors. They enable the defined presentation of one type of ligand on an otherwise inert background. In contrast to the concentration regulated immobilization of receptors, we do not control the density statistically here. Instead it is precisely adjusted by the inter-particle spacing of the gold particles serving as anchor points for the receptors. Thus these interfaces are also ideally suited to study clustering effects important for many biological signalling processes [147].

New possibilities to obtain better ordered nanostructured glass surfaces especially for large scale cell analysis were exploited (in cooperation with *Eva Bock* [148]). Additionally, new solution surface based methods and optimizations based on the solvent to adjust the inter-particle spacings were discovered, which lead to a broader range of possible spacings, for the same gold dot size, than previously achievable.

Nanostructured surfaces with metal particles of 1–15 nm [149] in a quasi-hexagonal pattern with interparticle spacings between 25–250 nm [150] can be produced with block-copolymer micellar nanolithography (BCML). This technique is based on the self-assembly of micelles of diblock-copolymers loaded with metal salts after dipping a hydrophilic surface into the micellar solution. First the diblock-copolymer with a hydrophilic block of poly-2-vinylpyridine (P2VP) and a hydrophobic block of polystyrene (PS) is dissolved in a solvent, typically toluene. A concentration above the critical micelle concentration (cmc) [151] is chosen to ensure aggregation of most polymers into micelles. Their hydrophilic cores are subsequently loaded with metal salts, such as $\text{HAuCl}_4 \cdot 3\text{H}_2\text{O}$ (fig. 4.10).

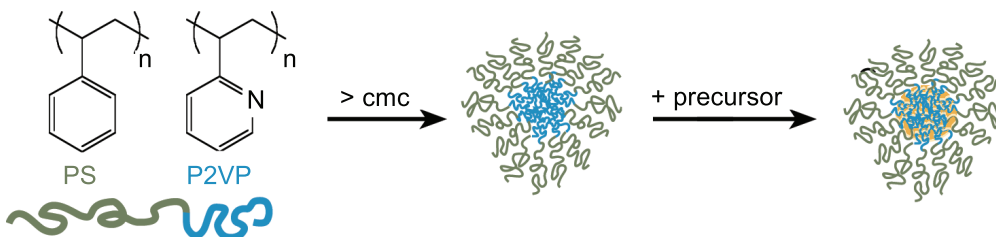


Fig. 4.10 – Formation of micellar solutions: the diblock-copolymers consist of hydrophobic block of polystyrene (PS) and hydrophilic block of poly-2-vinyl-pyridine (P2VP). In a non-polar solvent like toluene they form inverse micelles above the critical micelle concentration (cmc). The hydrophilic micelle cores are subsequently loaded with metal salts.

The micelles are transferred to the desired surface by dip-coating. Therefore the surface is dipped into the micellar solution at a defined speed in a 90° angle towards the solution surface. The self-assembly of micelles on the immersed surfaces is based on a two-step process (fig. 4.11). First, the hydrophilic surfaces are probably covered with a layer of free polymers with the P2VP groups adsorbing to the surfaces leaving the hydrophobic PS groups dangling in solution [152]. This polymer layer has been measured with surface plasmon spectroscopy in a total internal reflection setup with non-metal salt loaded PS-PVP solutions [153]. Additional evidence for the formation of such a polymer layer has been obtained with AFM measurements in non-metal salt loaded PS-PVP polymer solutions below 10 % [154]. They could also prove that the micelles are not adsorbed in solution. Instead, complete micelles are most likely deposited on the surface during retraction of the sample, as their hydrodynamic radius determined in dynamic light scattering experiments corresponds to the spacing determined with

the AFM for pure diblock-copolymer solutions [155].

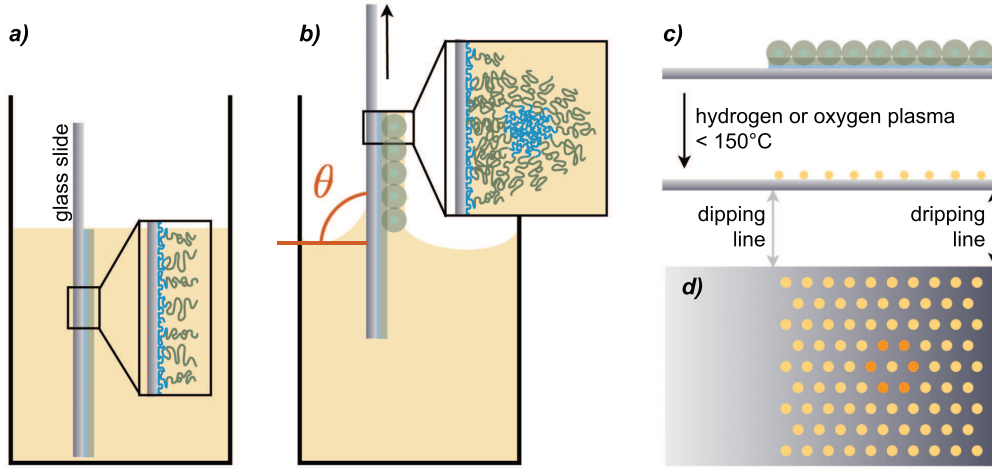


Fig. 4.11 – Self-assembly of micelles on a hydrophilic surface: a) In a first step free polymers adsorb to the hydrophilic surface with the hydrophilic P2VP groups leaving the PS groups dangling in solutions. This adsorption takes place while the surface is immersed in the solution. b) The glass slide is retracted at a tilt angle θ of 90° . The micelles are extracted during the retraction of the surface where they arrange in a quasi-hexagonal order during evaporation of the solvent. c) The dried surfaces are subsequently treated with a hydrogen or oxygen plasma which burns away all polymers and simultaneously reduces the gold salt to elemental gold leaving quasi-hexagonal ordered gold particles on the surface with distinct spacings of 25 to 250 nm. As the surface is only nanostructured up to the dipping line, the unstructured surface can be employed as an internal reference. d) Hexagonal pattern of gold particles in top view.

The dip-coated and dried surfaces are subsequently subjected to a plasma treatment in which the polymer is burned away completely and the gold salt is reduced to elemental gold particles. The size of the gold particles depends on the employed polymer and especially the length of the hydrophilic P2VP part [153], as well as on the gold salt loading by which it can be varied between 1 and 15 nm [149]. The spacing between the individual gold particles is governed primarily by the length of the hydrophobic PS block [153], but also by the physical properties of the dipped surface [149, 156], the polymer concentration [139] and the retraction speed [139, 140, 157], and can thus be varied between 25 to 250 nm [150].

The film height of pure solvent films adsorbed to surfaces during dip-coating depends on the physical properties of the solution such as viscosity η , density ρ and surface tension σ [158]. For low capillary numbers $Ca = \mu U / \sigma \ll 1$ the viscous contribution to the normal pressure can be neglected:

$$h_\infty = 0.946 \sqrt{\frac{\sigma}{\rho g}} Ca^{2/3} \quad (4.1)$$

$$\Rightarrow h_\infty = C \cdot (\rho g)^{-1/2} (\eta U)^{2/3} \sigma^{-1/6} \quad (4.2)$$

where g is the standard acceleration of gravity and U stands for the retraction velocity. The applicability of this model has been expanded to larger capillary numbers for immersing the rectangular surface perpendicular to the solution with no tilt angle [159]:

$$h_\infty = 0.946 \sqrt{\frac{\sigma}{\rho g}} Ca^{2/3} - 0.107 Ca \quad (4.3)$$

This theory has been successfully linked to the particle spacing of dip-coated micellar solutions [157].

The film height determines the number of micelles per area on the surface. Once the solvent evaporates these are ordered by capillary forces forming hexagonal, closely packed monomicellar films. As micelles are not hard spheres, which particularly holds true for large micelles, they can flatten on the surface to form regular arrays over a relatively broad range of concentrations. Thus the inter-particle spacing can be adjusted by either the overall concentration of micelles in solution or by the height of the extracted film (fig. 4.12).

The number of particles n_m on a certain area A is given by the volume above this area V and the concentration c_m of micelles in the solution.

$$\frac{n_m}{A} = \frac{V \cdot c_m}{A} = \frac{(h \cdot A) \cdot c_m}{A} \quad (4.4)$$

Thus the areal density of the particles on the surface ρ_A is directly proportional to the film height and the concentration of micelles c_m (fig. 4.12):

$$\rho_A = h \cdot c_m \quad (4.5)$$

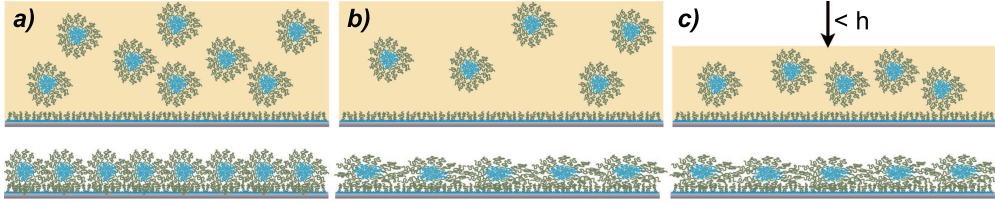


Fig. 4.12 – Dependence of the inter-particle spacing on the film height and the micellar concentration: Large micelles in particular can flatten out on the surface and can thus be arranged in regular arrays with varying inter-particle distances. a) The micelles are deposited on the surface after evaporation of the solvent ordered by capillary forces. Larger inter-particle distances are obtained with lower micellar concentrations (b) or smaller film heights (c).

The areal density ρ_A is directly related to the inter-particle spacing d_s for homogenous distributions of gold particles:

$$\rho_A = \frac{2}{\sqrt{3} \cdot d_s^2} \quad (4.6)$$

Thus the inter-particle spacing can directly be compared to the concentration and the film height:

$$d_s = \sqrt{\frac{4}{\sqrt{3} \rho_A}} = 1.075 \cdot c_m^{-1/2} \cdot h^{-1/2} \quad (4.7)$$

This equation resembles the inverse relationship between the inter-particle distances and the concentration. The inverse relationship to the retraction speed U is obtained by its proportionality to the height of the film given by equation 4.2:

$$d_s \propto U^{-1/3} \quad (4.8)$$

However, the relation between the spacing and the concentration is not as simple as suggested by equation 4.7, as the concentration of the micellar film will also influence the viscosity of the solution and thus the height of the extracted film.

4.3 Quality Control of Nanopatterned Surfaces

The quality of the nanostructured surfaces influences the significant results of cell experimental results. Therefore it is important to characterize the different problems that can arise in the production of surfaces with BCML. Apart from large defects easily visible in the SEM, but not detectable in standard microscopy, the nanopattern needs to be homogeneous over the complete surface. The distribution of the diameter of the gold particles should be as narrow as possible and last but not least particles should be arranged regularly on the surface.

4.3.1 Particle Size Distribution

The dimensions of the gold particles influence their accessibility within the passivating PEG layer and the interaction potential with membrane receptors. Thus a fixed gold particle size is desired for cell experiments.

The size of the gold particles is determined by the size of the micellar core and its gold salt loading. The size of the core depends on the length of the polymers and the respective length of the hydrophilic and hydrophobic chain, which show good monodispersities for the employed polymers. It also depends on the assembly of the block-copolymer into micelles. Aggregation of polymers as well as inhomogeneous distribution of the gold salt, e.g. due to inadequate mixing, compromise the monodispersity of the micelles.

The dimensions of the gold particles can be characterized in transmission electron microscopy (TEM). However, these measurements require a special grid surface which is too small to be dip-coated. Dropcasting of micellar solutions onto these surfaces nevertheless leads to similar nanostructures, where the amount of gold in a micellar core should not depend on the interparticle spacing.

The size distribution on a single surface can also be determined from SEM images (fig. 4.13). For these characterizations it is especially important to carefully adjust all apertures and lenses to obtain spherical particles without astigmatism. In order to compare the size distribution independently from the number of visualized particles, the histogram is normalized by the overall number of detected particles. Where the size distribution, given by the width of the gaussian fit, is comparable between different particles the size of the particle also depends on the brightness, contrast and threshold employed for the detection of the particle.

4.3.2 Long and Short Range Order of Nanostructured Surfaces

Two length regimes are important for the quality of the quasi-hexagonal arrangement of gold particles: short and long range orders. The short range order is characterized by the spacing between nearest neighbors and their geometrical arrangements. Thus the particles should be arranged in a hexagonal pattern with each particle enclosed by six others. However, if the soft micelles are not arranged perfectly, different numbers of nearest neighbors are observed. The quality of the geometrical short range arrangement can be illustrated with a Voronoi diagram [160]. The radial distribution function (RDF) on the other hand does not consider the geometrical order of particles, but instead characterizes the density distribution of particles on a surface [150,161].

Voronoi Diagrams Describe the Geometrical Arrangement

The gold particles should be arranged in a hexagonal pattern on the surface, based on the closed packed structure of their micelles. Hence, all particles should have exactly six nearest neighbors. In a Voronoi diagram, a Delaunay triangulation is employed to

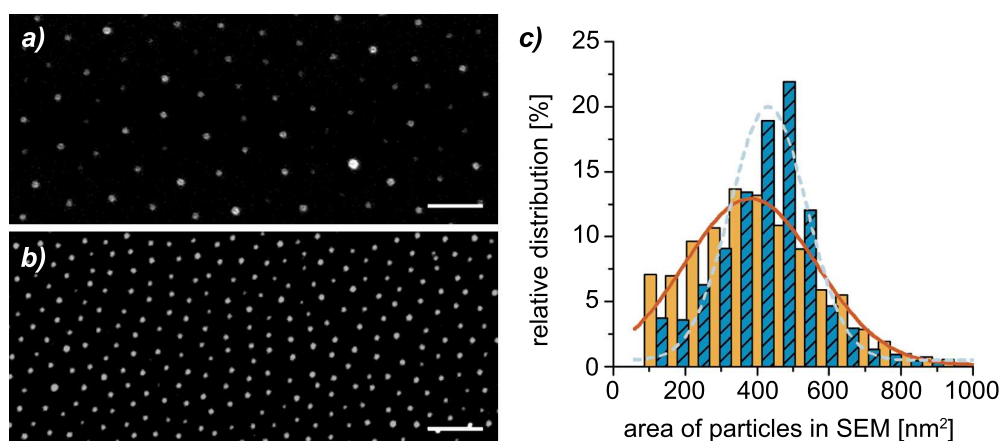


Fig. 4.13 – The size distribution of gold particles varies depending on the preparation procedure. Different volumes of the same micellar solution (16 and 12 ml of 1056er polymer in toluene) were prepared under identical conditions. The nanostructured surfaces were observed in the SEM, with careful adjustment of the apertures and lenses to obtain spherical particles without astigmatism. The images were adjusted for optimal particle recognition performed with ImageJ. Preparation of large amounts of micellar solutions (a, orange solid columns in c) leads to a broad distribution of gold particle sizes, which is not observed for smaller amounts (b, blue striped columns). In order to compare the size distribution independently from the spacing, varied here by the dipping speed, the histogram is normalized by the overall number of detected particles. The size distribution can be fitted by Gaussians underlining the difference in the size distribution given by the center position and the standard deviation of the 12 ml solution (light blue, dashed line in c): $431 \pm 213 \text{ nm}^2$ and the 16 ml solution (dark red, straight line in c): $381 \pm 368 \text{ nm}^2$, corresponding to an average diameter ranging between 11.86 and 20.22 nm for 12 ml and a range of 2.96 up to 21.8 nm for 16 ml solutions. Scale bars in the SEM cut outs correspond to 100 nm.

place each particle in a so-called Voronoi cell. This polygon shares one side with each of its nearest neighbors. Each cell can subsequently be color-coded by the number of enclosing neighbors to judge the quality of their geometrical arrangement [160].

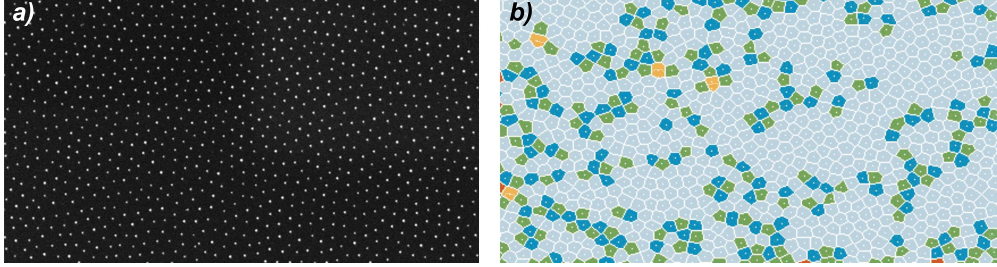


Fig. 4.14 – The Voronoi Diagram illustrates the geometrical arrangement of the gold particles: First the center of each gold particle on the SEM image (a) is determined. Following a Delaunay triangulation, a Voronoi cell is placed around each gold particle center depicting a polygon adjacent to all nearest neighbors. These polygons are then color coded by the number of nearest neighbors (b), where light blue corresponds to six, dark blue to seven, orange to eight, green to five and dark orange to four nearest neighbors. The Voronoi parameter for this surface is $\psi_{V6} = 0.67$ following equation 4.3.2

The hexagonal Voronoi parameter ψ_{V6} was defined as the ratio of Voronoi cells vc with six neighbors vc_6 (eq. 4.3.2). Thus a perfectly hexagonal surface corresponds to a Voronoi parameter of one.

$$\psi_{V6} = \frac{vc_6}{vc} \quad (4.9)$$

The Radial Distribution Function (RDF) Depicts the Short and Long Range Translational Arrangement

The radial distribution function (RDF) $g(r)$ is defined by the local density ρ at a given distance r towards the center normalized by the overall density of the system ρ_0 (fig. 4.15):

$$g(r) = \frac{\rho(r)}{\rho_0} \quad (4.10)$$

The local density $\rho(r)$ is given by the number of particles in a ring defined by the radius r with the thickness dr divided by the area of this ring:

$$\rho(r) = \frac{N(r + dr)}{2\pi r dr} \quad (4.11)$$

The resulting RDF illustrates the periodicity of the nanopattern. Ideally, sharp peaks are observed for each 'round' of gold particles (fig. 4.15). Deviations from the perfect order lead to a broadening of the peaks increasing with larger radii. Thus the long range order of the system is indicated by the number of recognizable peaks. The short range order on the other hand is related to the width of the first peak, whose center corresponds to the average inter-particle distances.

In order to characterize the quality of larger surfaces the RDF based on one center particle was adopted to display the RDF averaged over many particles. Therefore the

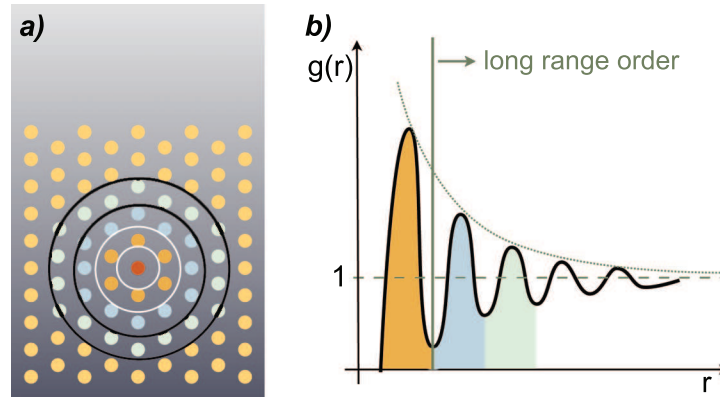


Fig. 4.15 – The radial distribution function (RDF) characterizes the particle density on a surface. a) First, the number of particles in a given ring with radius r and thickness dr from the center (red) is determined (e.g. green particles within the ring delimited by the black rings). The corresponding local density $\rho_A(r)$ within this ring is obtained after dividing by the area of the ring. The radial distribution function $g(r)$ correlates the local density with the overall density of the system (eq. 4.3.2). b) The first peak of the radial distribution function indicates the average spacing where the broadness of the peak is correlated to the variance of the spacing. The long range order is indicated by the number of peaks appearing at higher distances.

maximal distance r_{max} was defined to be calculated and averaged over the RDF of all particles with at least this distance towards the edges of the image (fig. 4.16). Thus the same number of particles are considered for each calculated RDF. As this approach considers all particles of an image, it is not prone to defects at the center of the SEM image. Additionally, the position of each particle was identified first and then the RDF was calculated independent from the size of the particles in order to separate these different parameters from each other.

The averaged RDF can mathematically be described as an overlay of multiple gaussian functions (fig. 4.17). Ideally, the area of each gaussian fit should be the same (fig. 4.17a) corresponding to the periodicity of the system - e.g. the area would be one if the RDF was displayed in periodicity (fig. 4.17).

The center of the first gaussian fit corresponds to the average spacing, where its broadness is related to the accuracy of the short range order characterized by the standard deviation of the spacing.

4.3.3 Homogeneity of the Inter-Particle Spacing Across the Surface

The homogeneity of the nanopattern across the surface can be obtained by comparing the order of the nanostructures at different positions on the glass slide. Thereby it is important to compare the structures horizontally and vertically. In order to correlate the cell experimental results to the inter-particle distances, it is important to either have a homogeneous distribution on the whole surface or to have well defined changes in the spacing. Often the gold dot density is much higher and less ordered in up to 1 mm distance to the dipping line. A higher density of gold dots is normally also present for about 1-2 mm at the dripping line on the bottom of the glass slide. Both areas are therefore excluded from the analysis.

The radial distribution function can also be averaged over particles from SEM im-

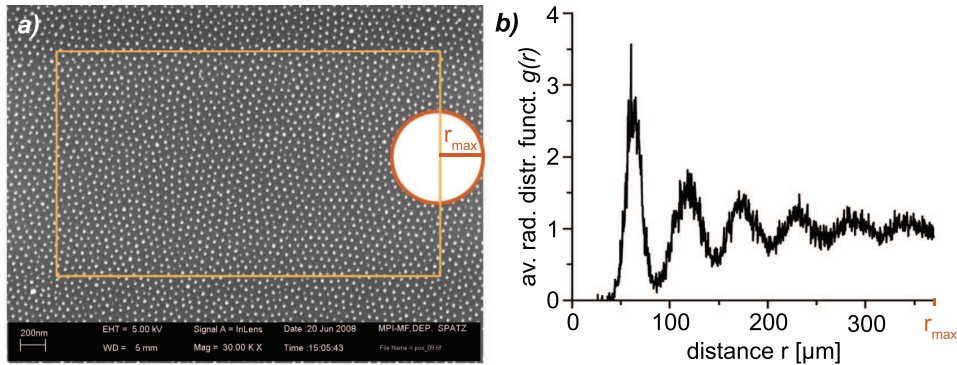


Fig. 4.16 – Calculating the average RDF: a) First the position of all particles on the SEM image are determined. For a given maximal distance r_{max} , the particles with at least this distance to the edges (within the orange frame) of the image are identified. For each of these particle the RDF is calculated up to this maximal radius (red circle) and subsequently averaged by a self-written IDL program (b).

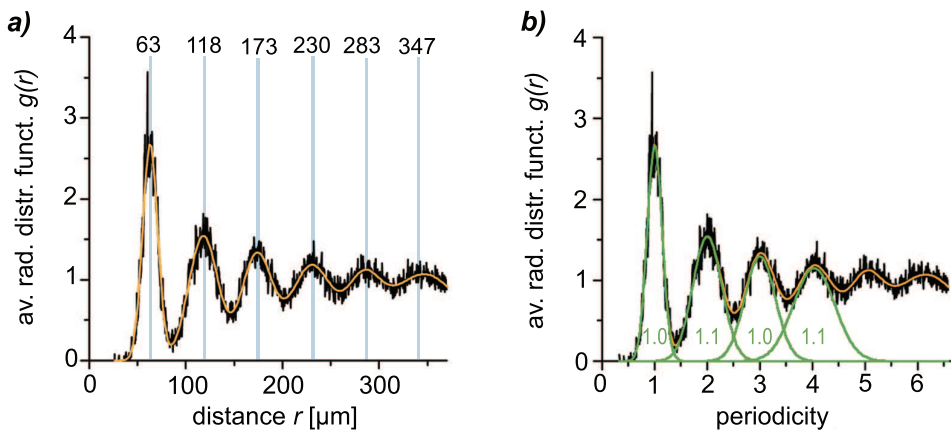


Fig. 4.17 – Gaussian fit to the average RDF: The averaged RDF of fig. 4.16 was fitted with six gaussians. a) The combined average curve of all six gaussian fits (orange) corresponds very well to the calculated average RDF. The center of the first peak corresponds to the average spacing, where its standard deviation is characterized by the broadness of the peak given by the width of the gauss fit. Thus the average spacing of the gold particles on the image of fig. 4.16 is $63.0 \pm 7.8 \mu\text{m}$. The center position of all gaussian fits, given in the graph, are not exactly multiples of the first peak due to the hexagonal arrangement of the particles, but are spaced with a homogenous periodicity. b) If the RDF is displayed in terms of the periodicity, the area of each gaussian curve (green) should correspond to one.

ages of different positions to compare the homogeneity over very large distances. Even if the RDF of a single SEM image indicates a uniform distribution of particles, only the averaging over different SEM images separated by millimeters allows an extensive characterization of the complete surface (fig. 4.18)

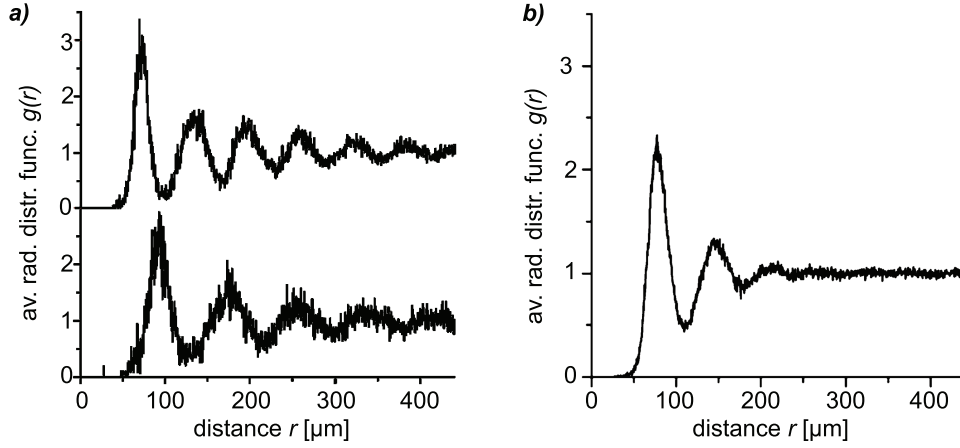


Fig. 4.18 – RDF averaged over the complete surface: a) The RDF of the single SEM images at 2 (top) and 8 mm (bottom) distance to the dipping line suggest a homogeneous short and long range order over one image. Comparison of the two indicates a change in the inter-particle spacing from 75.60 ± 9.03 nm to 93.30 ± 12.56 nm, resulting from a spatial gradient here (see chapter 4.4.1). b) The RDF averaged over 14 images across the complete surface illustrates the inhomogeneity by the reduced long range order indicated by the few distinguishable peaks. The first peak indicates a broader distribution of the inter-particle spacing of 79.51 ± 12.7 nm.

4.3.4 Characterization of the Translational Short Range Order

The gold particles around the nearest neighbors in the second ring do not all have the same distance towards the center particle (black lines in fig. 4.19). This is caused by the non-karthesian coordinate system of the lattice structure. The translational order of the two-dimensional crystal structure should therefore be based on the hexagonal lattice structure spanned by two vectors of equal length with an interior angle of 60° . If the length of the vector corresponds to the inter-particle spacing, the distance between the center particle and all particles in the second ring corresponds to an even multiple of the unit vector (fig. 4.19):

This setup can be mathematically described by the reciprocal lattice. Then the translational order of the nanostructured surface depends on the periodicity of a set of superpositioned plane density waves $\psi_{\vec{G}}(\vec{r})$ [162]:

$$\psi_{\vec{G}}(\vec{r}) = e^{i\vec{G}\vec{r}} \quad (4.12)$$

where \vec{G} is the reciprocal lattice vector for the array. As $\psi_{\vec{G}}(\vec{r})$ vanishes in a homogeneous fluid for each \vec{G} and its average reaches unity magnitude in a perfect crystal, a subset of $\psi_{\vec{G}}(\vec{r})$ serves as an order parameter describing translational ordering of any symmetry lattice.

In an extreme case, the very short range order depends on the uniformity of the distance to the nearest neighbors, which is the same in real space and in the hexagonal

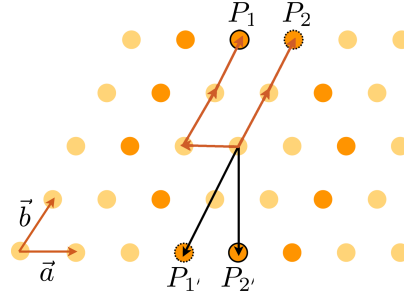


Fig. 4.19 – The hexagonal lattice structure of the gold particles are best described by a non-karthesian coordinate system: The distance of the center particle to particles in the 'second round' (dark orange) is not homogeneous in a standard coordinate system ($|P_{1'}| \neq |P_{2'}|$), but can be described by multiples of the lattice vectors (red): $|P_1| = |-\vec{a} + 2\vec{b}| = 1$ and $|P_2| = |2\vec{b}| = 2$.

lattice. All of these distances should ideally correspond to the unit vector. Thus the very short order can be defined by the deviation of the first peak of the RDF compared to the value one. As this deviation depends on the height and the broadness of the peak, the full width at half maxima (FWHM) of the gauss fit divided by the interparticle spacing was used:

$$\psi_{RDF} = 1 - \frac{FWHM}{spacing} \quad (4.13)$$

This definition allows the comparison of the homogeneity of the interparticle spacing for different interparticle distances.

4.3.5 Characterization of the Geometrical Short Range Order

So far, the fraction of hexagonally arranged particles was characterized to determine the quality of the geometrical arrangement of the particles. But even if all particles would be surrounded by six nearest neighbors they would not need to be regularly arranged with angles of $n/6 \cdot 2\pi$. Such an asymmetric hexagonality is characterized by the sixfold bond-orientational order parameter ψ_6 introduced in the KTHNY theory by *Kosterlitz, Thouless, Halperin, Nelson and Young*: [163–165]

$$\psi_6 = \left| \frac{1}{N_{bonds}} \sum_j \sum_k e^{i6\theta_{jk}} \right| \quad (4.14)$$

where θ_{ij} is the angle between the bond connecting sites i and j with respect to a reference direction and the angle brackets indicate and average over the nearest neighbors j .

Phillipe Girard (EMBL, Heidelberg) has implemented this last order parameter in an ImageJ plugin, where ψ_6 is calculated for each particles in respect to its six nearest neighbors.

4.3.6 Implications of the Particle Arrangement for Cell Experiments

A combination of the Voronoi diagram (chapter 4.3.2), the RDF (chapter 4.3.2) and the overall density enables a comprehensive characterization of the particles on a surface.

The overall density should be related to the strength of the triggered signal and is the most commonly monitored parameter for studying cell signal responses. On a perfect nanostructured surface, the signal would directly be related to the inter-particle distances (eq. 4.6). However, holes, e.g. caused by empty micelles or lost gold particles, will reduce the density without significantly altering the inter-particle spacing determined by the first peak of the RDF.

The short range order is expressed by the geometrical alignment and the average spacing of the particles, quantified by ψ_{V6} and ψ_{RDF} . The later might limit cluster formations between integral parts of the cell to the interacting receptors whereas the geometrical alignment of the particles might influence the angle at which these proteins would need to interact which might be limited by their bending rigidity or bulkiness.

The long range translational order, depicted by the RDF, is especially important to enable cell assays on large surfaces requiring a homogenous nanopattern for comparable results.

4.4 Optimization of the Nano-Structured Surfaces for Cell Experiments

Nanostructured surfaces for cell experiments need to fulfill special requirements: As the cells are observed in bright field and fluorescent microscopy, glass slides are suited best. They need to be nanostructures homogeneously across the whole surface without larger defects, as these are not detectable during the cell experiments.

In order to compare cell responses on different gold particle densities, the spacing of the particles has to be varied independently of their size over a large range. Preliminary experiments indicate, that RCJ-P cells should be studied on spacings ranging between 50 and 110 nm. In the cell experiments performed in our group so far, the spacing of the gold particles has been controlled by the choice of the polymer [138], the retraction speed [139, 140] and the concentration of the solution [137]. Variation of the dipping speed with suitable diblock-copolymers dissolved in toluene leads to a possible variation of the spacing over 30 nm with the same solution [139]. The use of only one solution is an advantage of the retraction speed based variation of interparticle distances, as the size of the gold particles should be identical on all surfaces. Whereas different diblock-copolymers often not only lead to different spacings, but also to different sizes of gold particles [153] which might change the interaction with the cell as the amount and accessibility of receptors bound to one particle might be changed as well.

Here, two more possibilities for the variation of the spacing of the gold particles are introduced. Both methods are based on a single polymer, which should ensure constant particle sizes and lead to a possible variation of the interparticle distance over 75 nm.

4.4.1 Variations of the Micellar Solutions Solvent

Micellar solutions with PS-PVP diblock copolymers can not only be prepared in toluene, but also in *ortho*-xylene [166] or in other xylene isomers as well as in toluene-xylene mixtures [167]. The different physical properties of the xylene isomers should lead to different spacings according to the differences of the retracted film heights calculated with eq. 4.2 (Table 4.1).

Table 4.1 – Physical properties of the xylene isomers compared to toluene from [Lange’s Handbook.] and [BGI536] with the calculated film height based on eq. 4.2 for a retraction speed of 11.5 mm/min.

	<i>ortho</i> - xylene	<i>para</i> - xylene	<i>meta</i> - xylene	toluene
σ [mN/m]	30.1	28.9	28.3	28.5
ρ [g/cm ²]	0.880	0.864	0.861	0.871
μ [mPa · s]	0.810	0.620	0.620	0.587
χ	0.76	0.86	0.87	0.82
h [nm]	529	452	450	432

Accordingly, the corresponding nanostructured surfaces also showed different spacings depending on the isomer used to produce the polymer solution. Thus the spacing was considerably smaller for *ortho*-xylene than for *meta*- or *para*-xylene, which showed about the same interparticle distances (fig. 4.20).

A combination of the different xylene isomers at different retraction speeds enables the preparation of homogenous surfaces with spacings between 55 nm and 130 nm with

one polymer at a constant polymer and gold salt concentration (fig. 4.21).

However, the size of the micelles is not only determined by the length of the two blocks of the diblock copolymer [168], but is also dependant on the solvents. Thus the micellar core can be specifically solvated leading e.g. to an enrichment of benzene in hexane [169]. This solvatization can lead to enlarged stabilized micelles as observed for PS-P2VP micelles after addition of water [148]. The bulk solvent also affects the formation of micelles characterized by the Huggins parameter χ [169], which is similar for *meta*- and *para*-xylene, but smaller for *ortho*-xylene (compare table ??). Accordingly, *Krishnamoorthy et al.* showed that the size of unloaded PS-P2VP micelles are not only deposited on the silicon surface with different interparticle spacings. They were also able to show in AFM and light scattering experiments that the size of the micelles depends on the solvent [167]. Furthermore they propose a change in aggregation number corresponding to the number of polymers in one micelle, inconsistently observing similar aggregation numbers for micellar solutions with *ortho*- and *meta*-xylene. This aggregation number is about twice as high as the aggregation number observed in *para*-xylene. Such large variations in aggregation numbers will not only change the concentration of micelles c_m in solution leading to different interparticle spacings (compare chapter 4.2), but will additionally affect the amount of gold salt within the core and thus the particle size.

Apart from the possibility of varying the spacing by the choice of the solvent, the micellar solution in xylene show longer life times and minor defects.

4.5 Unexpected Solution Surface Effects can be Utilized to Control the Interparticle Spacing

The standard procedure for the dip-coating of surfaces is based on round glass beakers in which the micellar solution is transferred right before the experiments. Coating of large surfaces thus requires a large volume of micellar solution. Preparation of a large volume of solution is not only costly but may also lead to inhomogeneous particle sizes as described in chapter 4.3.1. Therefore alternative geometries for dipping jars were tested (in cooperation with *Eva Bock*, MPI Stuttgart).

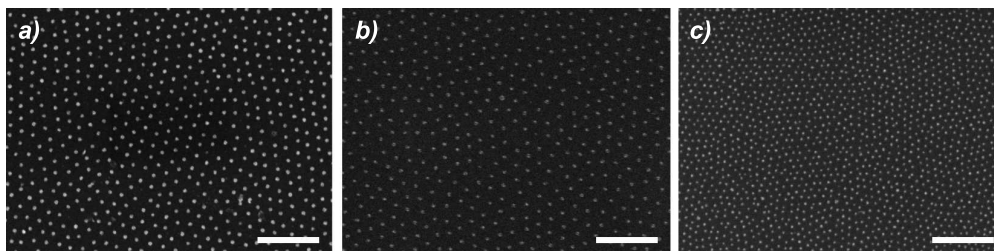


Fig. 4.20 – The interparticle spacing depends on the solvent of the micellar solution: Three different solutions with 5 mg/ml of 1056er diblock copolymer were prepared with a 0.5 gold salt loading. The spacing of the *meta*-xylene (a) solution corresponds to the *para*-xylene (b) solution at a retraction speed of 11.5 mm/min. The *meta*-xylene (c) solutions leads to much smaller spacings at the same dipping velocity (table 4.2). All scale bars correspond to 500 nm.

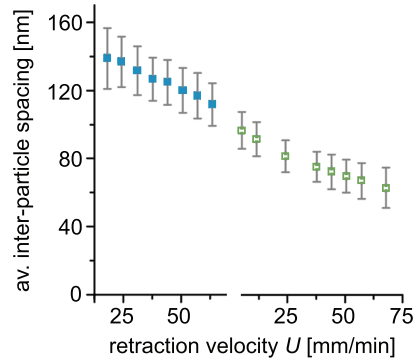


Fig. 4.21 – The interparticle spacing can be varied between 55 and 130 nm by adjusting the retraction velocity for two different solutions with the 1056er polymer in *ortho*-xylene (green, open symbols) and *meta*-xylene (blue, solid symbols).

4.5.1 Confined solution surface leads to linear increasing inter-particle distances

Dip-coating of 24×24 cm glass slides in a rectangular jar of 1×3 cm base area leads to gradients of increasing interparticle distances from the dipping line towards the dripping line (fig. 4.22). The nanopattern in the vertical direction parallel to the solution surface is very homogenous with good sixfold bond-orientational order parameters ψ_6 above 0.6.

The gradients of the interparticle distances are very reproducible over several surfaces with linear increasing spacings observed for different 1056er and 2076er polymer toluene solutions. Typically the interparticle distances increase by about 35 nm/10 mm for a micellar solution prepared with 1056er polymer in toluene dip-coated at a retraction speed of 11.5 mm/min. However the observed gradients do not simply depend on the geometry of the dipping jar, as the steepness of the gradient changes between different preparation cycles. Additionally, the tilt angle (compare fig. 4.10) at which the surfaces are dipped into the solution, which was kept constant during each preparation cycle, seems to play an important role in such a confined setup.

The sixfold bond-orientational order parameters ψ_6 , as calculated by the ImageJ plugin provided by *P. Girard*, has been shown to depend inversely on the interparticle

Table 4.2 – The interparticle distances depend on the employed solvent: The three different xylene solutions described in fig. 4.20 show different interparticle spacings roughly corresponding to the calculated film heights (table 4.1). However, the distances obtained with the corresponding toluene solutions are not the smallest as calculated.

	<i>ortho</i> - xylene	<i>para</i> - xylene	<i>meta</i> - xylene	toluene
spacing	67.5	111.6	112.2	79.6
st.dev.	11.3	10.8	11.3	9.2
ψ_{V6}	0.7	0.7	0.7	0.8
ψ_{RDF}	0.6	0.8	0.8	0.7

spacing [139, 150]. Nonetheless, we did not observe significant changes of the order parameter along these gradients (fig. 4.22).

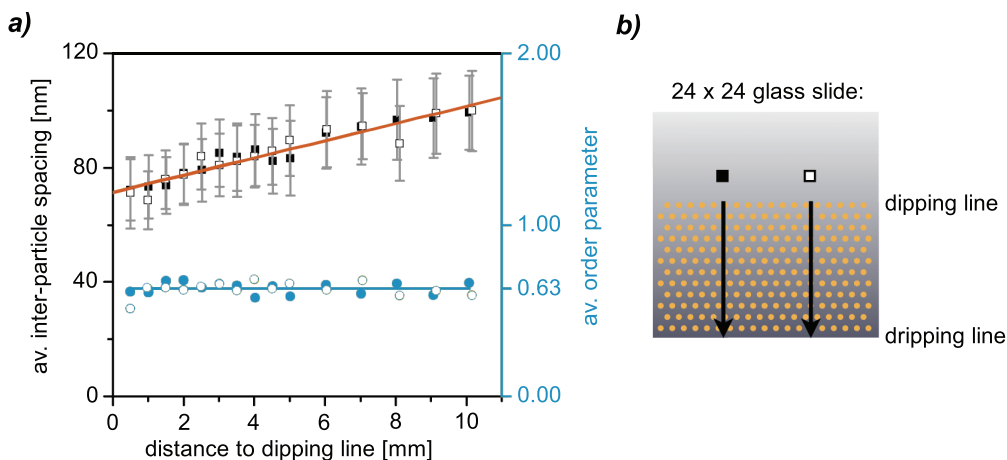


Fig. 4.22 – The interparticle spacing changes gradually if the 24×24 cm glass slides were dip-coated in a rectangular dipping jar of 1×3 cm base area. a) The spacing of the gold particles increases linearly from the dipping line towards the dripping line, changing by about 35 nm from an interparticle spacing of 75 nm to 110 nm within 10 mm in a standard 1056er solution dipped at 6 V. However, the spacing is very homogenous parallel to the dipping line. The error bars depict the averaged standard deviations. Interestingly, the average order parameter (blue) does not change considerably across the surface. b) Schematical presentation of the position dependent analysis of the nanostructured surface by SEM.

A similar gradient was observed with different batches of micellar solutions. The effect is not consequently caused by the preparation of the micellar solution, but might still depend on the type of the employed diblock copolymer, which influences the size of the micelles and thus their elasticity. Only larger micelles can be transferred onto glass slides at different retraction speeds without dewetting effects (chapter 4.2). Thus only those might show a gradient in this setup.

The modified area of the solution surface in front of the immersed glass slide was identified as a possible cause for the spatial gradient of the interparticle spacing. In order to test this hypothesis, the surface area of the solution was varied in front of the glass slide between 0.5 cm and 2.5 cm independently from all other parameter except for the volume of micellar solution in front of the glass slide. Therefore slim glass slides ($0.8\text{-}0.9 \times 2.4$ cm) were dip-coated at a perpendicular direction in the rectangular jar (fig. 4.23).

The spacing of the gold particles increases towards the dripping line if the slim glass slides are dipped in a perpendicular manner with 0.5 cm distance to the wall (fig. 4.23c). This setup corresponds to dip-coating 24×24 glass slide in the parallel direction (fig. 4.23b). No gradient is formed, if the glass slide was dipped at 2.5 cm distance towards the wall of the dipping jar. The slight gradient at 1.5 cm distance to the wall is mainly due to the first and last point which are largely affected by the dipping and dripping line. The average order parameter is not changed, except if the surface is dipped at distances lower than 0.5 cm towards the wall.

The results obtained with 0.7 cm glass cover slides are very puzzling. With these glass slides no gradients were observed no matter if the distance to the wall is 2.5 or 0.5 cm. Also, no gradients were detected if they are dipped in the usual parallel

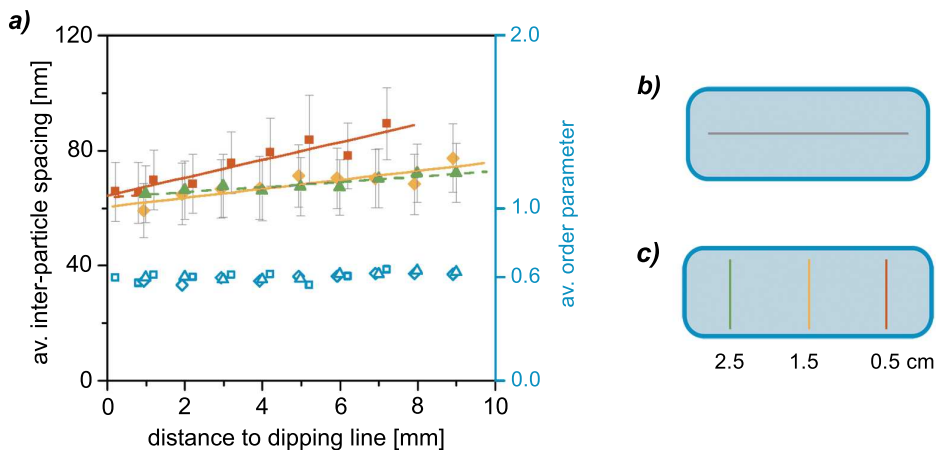


Fig. 4.23 – Variation of the surface area could be achieved by dipping slim glass slides, about 0.8 cm wide into the rectangular jar at a perpendicular orientation. a) If the glass slides are not dip-coated parallel to the long side of the dipping jar (b), but turned by 90 degrees (c), different distances to the wall of the jar can be compared at otherwise constant parameters. The interparticle spacing varies gradually on the surface dipped closest to the glass wall (red squares). No significant changes of the distances are observed for 2.5 cm distance to the wall (green triangles), where the surface dipped with 1.5 cm distance to the glass wall (orange diamonds) shows only a slight gradient increased by the edges close to the dipping and dripping line. Interestingly, all averaged order parameters are comparable.

direction. Consistent with these results, no gradients were observed if the 0.8-0.9 cm wide glass slides are dipped in the parallel orientation with 0.5 cm distance to the glass wall. Thus we believe the effective solution surface area, depending on the size of the glass slide and its accessible solution surface, must be important. Therefore the solution surface before the glass slide was calculated. In order to compare different widths of glass surfaces and to take the solution surface area on the side of the glass slide into account. We determined an 'accessible depth' d_{acc} of the solution surface as the area of the solution surface A_s before the glass slide divided by the width of the glass slide w_g :

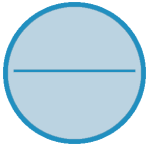
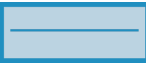
$$d_{acc} = A_s/w_g \quad (4.15)$$

Comparison of the accessible depth suggests a very narrow range in which gradients appear (table 4.3).

If the gradient was caused by a different formation of the meniscus due to the close proximity to the wall, the only parameter that should matter, would be the distance towards the glass wall of the jar. However, no gradient is observed if slim glass slides are dipped in the same manner as the 24×24 cm glass slides. If the dipping jar is filled up to the rim with micellar solution and an inverse meniscus is observed, the order is completely lost. Even though, the order parameter is not affected by the closer proximity to the wall even for the surfaces with spatial gradients.

As the micelles are not absorbed onto the surface in solution, but during its retraction (see chapter 4.1.3) the micellar concentration close to the surface of the solution plays a vital role. In order to double check that the volume of the micellar solution in front of the glass slide does not play a role, a special dipping jar was designed. It is based on the same rectangular design, but with an additional bulge to enlarge the solution surface (fig. 4.25).

Table 4.3 – Accessible solution surface. The different dipping geometries and width of glass slides lead to different areas of solution surfaces accessible to the glass slide. These can be compared by calculating the accessible depth of solution surface d_{acc} . The dip-coated area was calculated assuming an immersion depth of 10 mm .

geometry of jar w/ glass slide	A_s [mm^2]	d_{acc} [mm]	gradient observed?	dip-coated area of slide [mm^2]
	270	$270/24 = 11.3$	no	240
	130	$130/24 = 5.4$	yes	
	150	$150/8.5 = 17.6$ $150/7 = 21.4$	no	85 or 70
	130	$130/8.5 = 15.3$ $130/7 = 18.6$	no	
	50	$50/8.5 = 5.9$ $50/7 = 7.1$	yes	
	50	$50/8.5 = 5.9$ $50/7 = 7.1$	no	

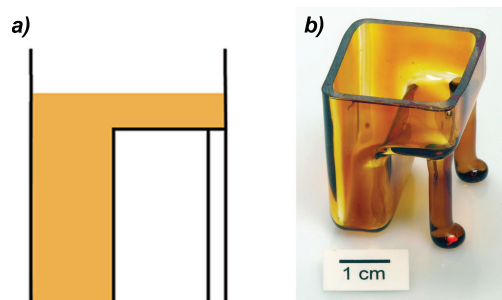


Fig. 4.24 – Design of new dipping jar: Based on the rectangular jar with an extra bulge to enlarge the solution surface in front of the dip-coated glass slide. Photograph by *B. Heinze*, MPI Stuttgart.

24 × 24 cm glass slides prepared in these new dipping jars do not show any spatial variations of the interparticle spacing, but homogenous nanostructures across the complete surface. Thus this new dipping jars design enables the production of large nanostructured surfaces with a reduced volume of the micellar solution.

4.5.2 Trapped Solvent Vapors Influence Interparticle Distances

The geometry of the dipping jar above the solution additionally influences the interparticle distances. Since toluene and xylene vapors are considerably heavier than air, they can be trapped by high side walls. If convection is prevented, the spacing of the gold particles produced in such an enriched atmosphere is larger than in an open jar. We first observed this effect in rectangular jars of different heights [148] and subsequently designed lids with different heights for the new dipping jar. The spacing is considerably larger with the high lid than without one, where the height of the lid does not play a role (fig. 4.25 and table 4.4). The same trend can be observed for micellar solutions in toluene and all three xylene isomers.

Table 4.4 – The interparticle spacing is increased in the dipping jar with a high lid: Glass slides were dip-coated in a 1056er polymer micellar solution in *para*-xylene at 11.5 mm/min. The effect on the geometrical order ψ_{V6} and the translational order ψ_{RDF} is not as easy to judge.

solution	spacing	st. dev.	ψ_{V6}	ψ_{RDF}
B1	127.1	13.7	0.66	0.75
B2	126.0	13.7	0.63	0.74
Bo	86.2	11.9	0.65	0.68
Bv	90.1	11.0	0.65	0.71

The geometrical order characterized by χ_{V6} also seems to depend on the amount of trapped vapors, as it is similar for all surfaces dip-coated with and without the lid, even though the increased interparticle distances should lead to reduced geometrical order parameters. Comparison of different surfaces dip-coated at different retraction speeds show a clear relation between the areal density and the retraction speed (fig. 4.26a) following the predicted $U^{2/3}$ relation (see equation 4.2). The geometrical order also follows the $U^{2/3}$ relation. Correlating the geometrical order directly with the areal density shows an exponential dependence of these two parameters (fig. 4.26b). The results correspond to the observation by *Lohmueller and Arnold et al.*, who showed that the sixfold bond-orientational parameter, as calculated by the Plugin programmed by *P. Girard*, ψ_6 is inversely related to the interparticle spacing [139, 150]. The translational short range order ψ_{RDF} on the other hand does not show a clear dependence on the interparticle spacing.

Given that the order of the nanostructures is related to the interparticle spacing, surfaces with about the same spacings dip-coated in the new dipping jars with and without a lid were compared. Therefore the interparticle spacings were adjusted by variation of the retraction speeds. The geometrical order observed on the surfaces dip-coated with a lid show improved geometrical orders: where the same micellar solution leads to $\psi_{V6} = 0.73$ without a lid at 11.5 mm/min, it leads to $\psi_{V6} = 0.78$ with a lid at 68 mm/min (with standard deviation of 0.02, averaged over four surfaces each). Additionally, the long range order is significantly improved (fig. 4.27).

In conclusion, the new dipping jar design leads to improved nanostructured surfaces with homogenous interparticle distances throughout the complete nanostructured area.

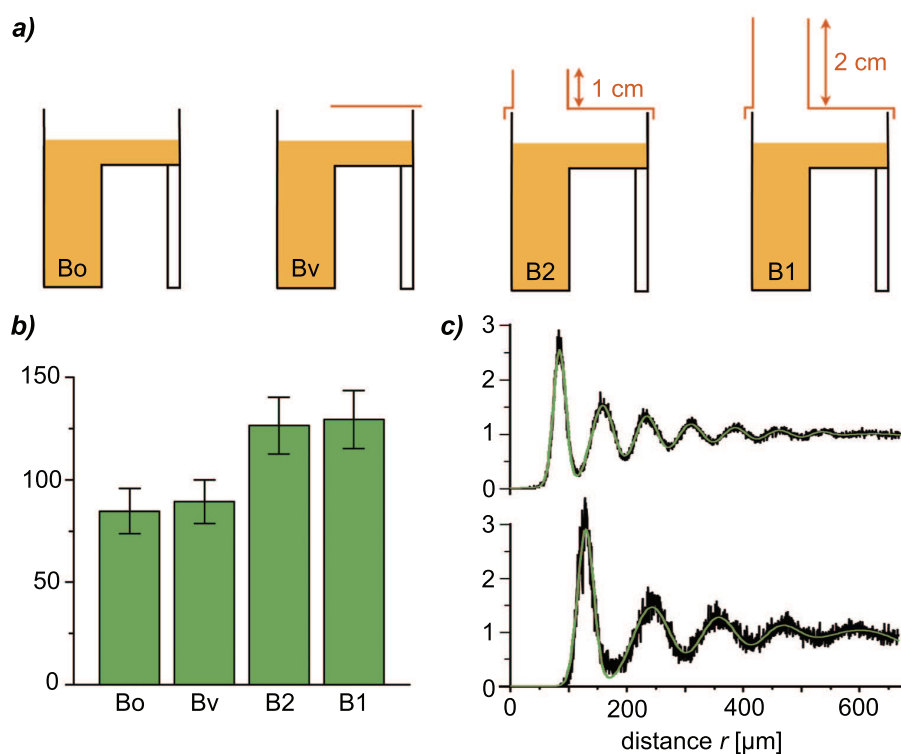


Fig. 4.25 – Trapped vapors influence the interparticle spacing: As the solvent vapors are heavier than air, they can be enriched above the solution by a suitable lid. Therefore, the lid of the the newly designed dipping jar was varied. a) Schematic side view of the setup without a lid (Bo), front covered by a large cover glass (Bv) and with an especially designed lid of 1 cm height (B2) and 2 cm height (B1). b) The average spacing obtained by the gaussian fit to the RDF are comparable for the open and front-covered jar, which probably trap the same amount of solvent vapors, if no additional air convections, e.g. a hood, are present. The height of the lid also seems to be not as important, where the interparticle distances are considerably enlarged by the application of a lid. c) Comparison of the radial distribution function of Bo (top) and B1 (bottom), depicted with a multiple-gaussian fit, emphasizes the large difference in the spacing of the gold particles. The RDFs were averaged over nine images leading to noisier data of larger spacings due to the lower number of particles on each image. As the widths and number of the peaks is comparable, the order does not seem to be significantly affected.

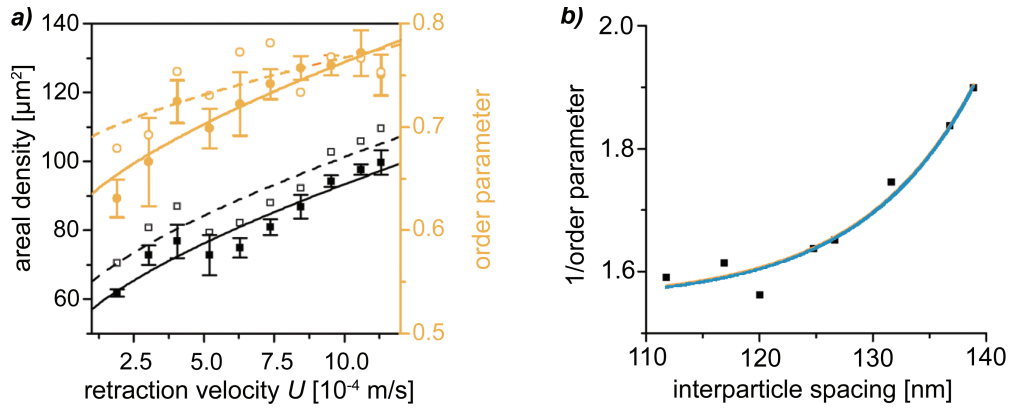


Fig. 4.26 – The areal density of gold particles depends on the retraction speed: The measured areal density averaged over 6 images (black squares) does not correspond to the density calculated from the interparticle spacing of the same images (open squares) following eq. 4.5. However, both densities can be fitted by a power law proportional to $U^{2/3}$ as predicted by eq. 4.2. The order of the nanostructured surface seems to depend on the interparticle spacing, where the geometrical order parameter ψ_V (orange circles) is proportional to $U^{2/3}$, as well as the translational short order parameter ψ_{RDF} (orange rings).

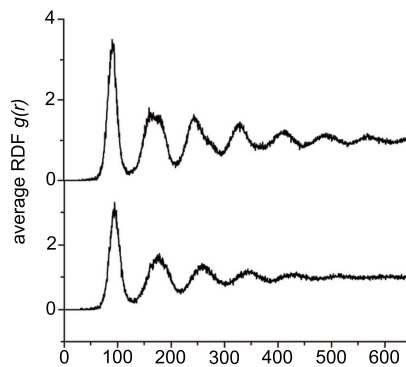


Fig. 4.27 – The new dipping jar design improves the long range order: In order to compare the quality of the long range order, the radial distribution function was calculated for surfaces with about the same inter particle spacing. It was averaged over nine different areas on one surface and was reproducible over three surfaces.

In combination with a lid high enough to trap solvent vapors sufficiently the geometrical order as well as the long range translational order have been successfully improved. Depending on the chosen solvent the interparticle spacing can now be varied between 100-140 nm with the 1056er polymer in *meta*- and *para*-xylene, where larger distances are achievable by diluting the micellar solution. Smaller interparticle spacings are achievable at higher micellar concentrations, down to about 70 nm. Alternatively the nano-structured surfaces can be prepared with micellar solutions in *ortho*-xylene leading to interparticle distances of 55-100 nm at a concentration of 5 mg/ml which can further be adjusted.

4.5.3 First Cell Experiments on Optimized Surfaces

First optimized, homogenous surfaces were prepared with an interparticle spacing of 70 nm (st. dev. 8 nm) with a 1056er polymer solutions at 6 mg/ml in *para*-xylene. Half of the glass slide was nanostructured, whereas the other half was coated with an RGD functionalized gold layer serving as an internal control between different sets of nanostructures. These surfaces showed a very good order over the complete surfaces ($\psi_{v6} = 0.69$ and $\psi_{RDF} = 0.70$) and the same interparticle distances on the first and last slide of the batch. The corresponding results were consistent of different samples and could be statistically analyzed.

The adhesion as well as the PCC area increase significantly over time, whereas their ratio decreases between 12 and 24 h of adhesion (fig. 4.28). On both nanostructured and gold RGD functionalized surfaces, the ratio decreases from 1.2 after 12 h to 1.0 after 24 h. Even though the ratio of adhesion and PCC area is the same on both surfaces, the areas do not correspond to one another. Both the adhesion area as well as the PCC area are significantly smaller on the nanostructured surfaces after 12 h and 24 h of adhesion.

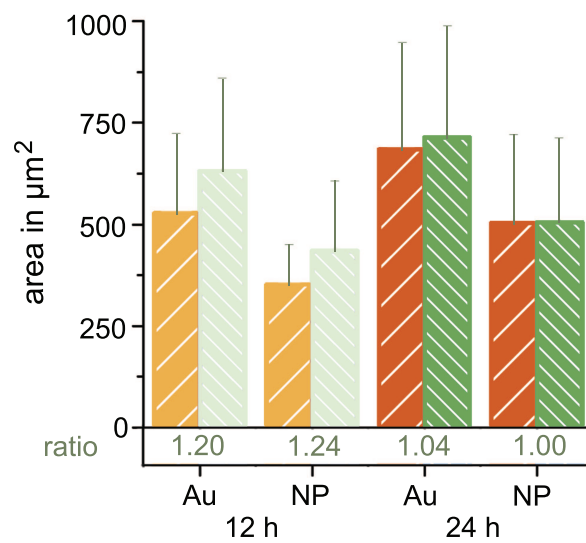


Fig. 4.28 – Nanostructured surfaces have a significant effect on the adhesion and the PCC: The cells were seeded on surfaces that were partially coated with a gold layer and partially nanostructured and subsequently RGD-functionalized. The adhesion area (large orange stripes) was significantly larger on the gold surface, than on the nanopatterned (NP) surface both after 12 (light colors) and 24 h (dark colors). The area of the PCC (small green stripes) was also significantly smaller on the NP surface at both time points. Both adhesion and PCC area increase significantly over time, where their ratio decreases.

Chapter 5

Materials and Methods

Within the scope of this work a multitude of techniques have been applied to physically characterize the samples. The techniques that have not been explained in detail so far, are briefly introduced here along with their technical specification. First the employed imaging techniques are summarized (chapter 5.1), followed by the diverse cell culture protocols (chapter 5.2) and the different methods for surface preparations (chapter 5.5) concluded with the micro-rheology details (chapter 5.4).

5.1 Imaging Techniques

5.1.1 Electron Microscopy

An electron beam is employed to image conductive surfaces with submicrometer resolution in a scanning electron microscope (SEM). The sample surface is scanned by a focused beam of primary electrons. This produces secondary products, such as X-rays, electrons or light, depending on the penetration depth, the studied material and the acceleration voltage. The interaction products used most frequently for the generation of images in scanning electron microscopy are the secondary (SE) and backscattered electrons (BSE).

Secondary electrons are generated by inelastic scattering of the primary electrons on the atomic core or on the electrons of the atomic shell of the sample material. Secondary electrons are low energy electrons (< 50 eV), which are either generated at the spot center (SE1), after multiple scattering events (SE2) or by BSE (SE3).

Our SEM Setup (Ultra 55 electron microscope with a field emission gun, Zeiss SMT) is equipped with different detectors. The inlens detector is ideally suited to map surfaces and is thus employed for my applications. It enables almost pure detection of secondary electrons (mostly SE1 and SE2). By default, an acceleration voltage of 5 kV was used at a working distance of 5 mm.

5.1.2 Light Microscopy

Standard bright-field and fluorescent images were taken on an inverted AxioVert 200M microscope (Zeiss, fig. 5.1). It can be employed in bright field, phase contrast, differential interference contrast (DIC) and fluorescent mode. Additionally it has been equipped with reflection interference contrast microscopy (RICM, see 5.1.3). A heated stage (Zeiss) and a home-built CO₂-chamber provide ideal conditions for cell imaging. The microscope is fully motorized and can be controlled manually or with the AxioVision4.4 software (Zeiss).

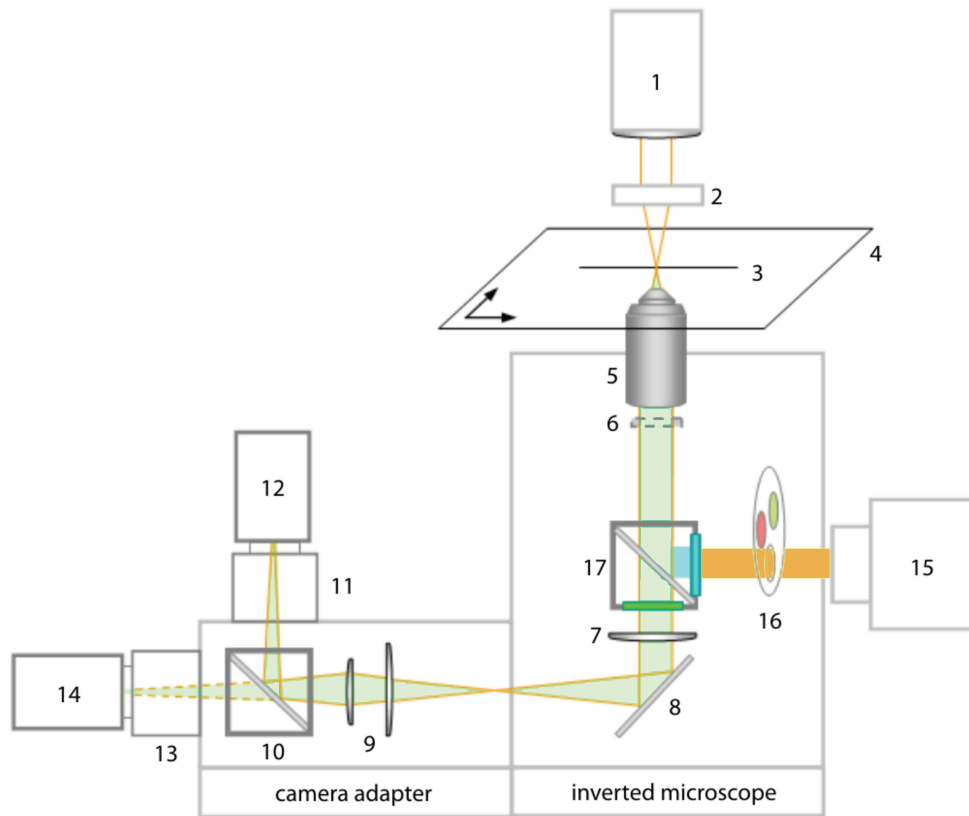


Fig. 5.1 – Setup of the AxioVert200M microscope: The light (1) is focused by the condenser (2) onto the sample (3) on the motorized xy-table (4). It is collected by the objective (5) and might pass through a Nomarski prism (6) in DIC mode. The parallel light is focused by the optovar (7) and mirrored (8) into the camera adapter. The telescope (9) transfers the image to the right position after being mirrored (10) through the C-mount (11) onto the camera or through passing the mirror-position (10) and a C-mount (13) onto another camera (14). In fluorescent mode, the light (15) passes the filter wheel (16) and the excitation filter in the filter cube (17). The excitation light is mirrored onto the sample and the emitted light that is shifted to higher wavelength through the Stoke's shift passes the mirror and the emission filter and follows the way of the bright light.

Bright Field Imaging

The microscope is fully motorized and can handle a huge variety of possibilities. Illumination of the sample is achieved by a HAL100 lamp in bright field mode. The light is adjusted according to Koehler [170] with the help of the condenser (compare No. 2 in fig. 5.1) before each set of similar measurements. The condenser is also used to position the circular aperture into the path of light in phase contrast mode. The exact position of the aperture is adjusted prior to each set of similar measurements with the help of an ocular telescope (Zeiss). The specific phase contrast aperture is chosen according to the needs of the objectives. For DIC a wollaston prism is added beneath the objective close to its back aperture (compare No. 6 in fig. 5.1) and another one is switched in place in the condenser above.

Fluorescence

Fluorescence is excited either by a xenon or an HBO lamp leading to similar results in normal fluorescence mode. The fluorescent filters (table 5.1) were chosen according to the applied dye. DAPI, WGA350 and the BrightBlue beads were imaged with the DAPI filter. GFPn, WGA488, YellowGreen beads and DiO were visualized with the eGFP filter. WGA555, mcherry-actin, BrightRed beads and DiI were visualized with the TRITC filter.

Table 5.1 – List of fluorescent filters employed in the motorized filter wheel in pos. 17, fig. 5.1

short name	company name	company	ex. [nm]	em. [nm]	mirror
DAPI	No. 49	Zeiss	365	445/50	FT395
eGFP	No. 38	Zeiss	470/40	525/50	FT495
TRITC	F36-503	AHF	543/22	593/40	BS562

Objectives

The applied objectives (Zeiss) differ in their magnification, working distance and numerical aperture. All these specifications can be found in the name of the objective (table 5.2). The first part of the name (e.g. EC Plan-Neofluar) specifies the general category of the objective. The neofluar objectives are all optimized for fluorescence. The number following the name denotes the magnification and the number following the backslash the numerical aperture. The name of objectives optimized for immersion fluids contains the abbreviation of the immersion fluid after the corresponding numerical aperture. If the objective can be used in phase contrast or DIC mode this is noted afterwards.

Most objectives are infinity corrected. This implies that the light leaving the objective will be parallel and needs to be focused for visualization, e.g. with an optovar. After the 'infinity' and the backslash the working distance is specified. This denotes the distance between the upper objective lens and the sample. The 40x water objective can be adjusted to the optimal working distance at a specific temperature as implied with the abbreviation 'Korr' before 'infinity'. After temperature equilibration this has been done before each set of measurements. The 63x DIC objective can be used with water or glycerin as immersion fluid after correct adjustment of the correction ring. If not otherwise noted it has been used with glycerin as immersion fluid.

Table 5.2 – List of Zeiss objectives most often used on the AxioVert200 M:

short name	complete label
10x	EC Plan-Neofluar 10x/0.3 Ph1 infinity/-
20x	LD Plan-Neofluar 20x/0.4 Ph2 Korr infinity/0-1.5
40x air	EC Plan-Neofluar 40x/0.75 Ph2 infinity/0.17
40x water	40x/1.2 W Korr infinity/0.14-0.18
63x DIC	new DIC obj.
63x water	63x C-Apochromat 63x/1.20 W Korr UV-VIS-IR
63x RICM	Plan Neofluar 63/1.25 Antiflex

Additional magnification can be achieved with the optovar (compare No. 7, fig. 5.1). Three different optovars with a magnification of 1.0, 1.6 and 2.5 are installed and can be switched easily.

Image Acquisition

The camera adapter (Zeiss) on the left port of the microscope allows to switch between two connected cameras by sliding a 100 % mirror in or out of the path of light (compare No. 10 in fig. 5.1). The light can also be split between the two cameras with the beam splitter 50R/50T VIS (AHF).

According to the different needs of the experiments different cameras are used. The Orca-ER (Hamamatsu, Japan) has a very high resolution and is very light sensitive. Therefore it is used in most applications. The PhantomV7.2 (VisionResearch, USA) is used for high speed image acquisition in microrheology. Image acquisition is achieved with AxioVision 4.5 and 4.0 (Zeiss) with the Orca camera. Wasabi (Hamamatsu) is used to acquire two images simultaneously from two Orca cameras and the phantom 630 software is used with the phantom camera.

Probe Table with CO₂ Chamber

The microscope is equipped with a motorized xy-table (Ludl) that can be controlled during image acquisition with the AxioVision 4.5 software (Zeiss) or manually with a LEP program (Ludl). Different sample holders can be replaced by a heatable inset (Zeiss), which is used in cell experiments set to 37°C. It is also used in microrheology experiments at variable temperatures. If not otherwise noted all microrheology experiments without cells are performed in the closed heating stage at 25°C. A special self-build, easily removable Plexiglas chamber can be placed above the heating table ensuring a 5 % CO₂ atmosphere as the sample closes the bottom of the heating chamber. It is equipped with a CO₂ sensor (GMP221, Vaisala) and controller (Typ GMM221, Vaisala) regulating the intake of CO₂.

5.1.3 Reflection Interference Contrast Microscopy (RICM)

Interference contrast microscopy was originally introduced to study cell adhesion and focal contacts without the need for fluorescent labeling [171]. In this special microscopical setup the interference pattern of a sample (e.g. a cell) on a plane glass slide is visualized. If monochromatic, polarised light is employed the interference pattern can even be evaluated quantitatively [172]. In such a reflection interference contrast microscope (RICM) setup the image is formed by superposition of the light waves reflected from the top surface of the planar substrate I_1 and from the bottom surface of the sample I_2 . A special antiflex illumination technique further effectively suppresses

all straight light [173]: The RICM-objective renders the incident light, linearly polarized by an integrated quarter-wave plate. Reflection at both interfaces of the sample reverses the direction of polarization of this circularly polarized light. When it passes through the quarter-wave plate again, it emerges as linearly polarized light but with the polarization turned by an angle of $2\pi/2$ with respect to the incident light. A second polarizer, crossed by $2\pi/2$ with respect to the first one, allows this light to go through but cuts off all stray light [112].

The intensity distribution $I(h(x, y), \lambda)$ of the interference pattern for a given wavelength λ is given by

$$I(h(x, y), \lambda) = I_1 + I_2 + 2\sqrt{I_1 I_2} \cos\left(\frac{4\pi n h(x, y)}{\lambda} + \delta\right) \quad (5.1)$$

where n is the refractive index of the medium and δ is the phase shift of the light reflected from the sample. The height is thus given by $h(x, y)$ at the lateral position x, y and can thus be calculated from the acquired intensity profiles with an ambiguity of $\Delta h = p\lambda/2\pi$.

This limitation can be overcome with dual-wavelength RICM (DW-RICM), which enables the determination of the absolute vertical position with an excellent resolution [112]. It has also been successfully applied to determine the height of ultrathin (50-250 nm) crosslinked HA cushions [174, 175]. Another advantage of this technique is its high sensitivity below water and the possibility of rapid measurements of distances with 10 ms time resolution [112].

For the HA model systems (chapter 3.4.4) it was important to determine the exact vertical position of a polystyrene beads at much larger distances than observed by Schilling et al. We were able to achieve this by visualization of the interference pattern of three different wavelength simultaneously (3 λ -RICM).

Even though interference contrast microscopy has been widely used to study cell adhesion [176], interpretation of the data in this context is more difficult because of possible multiple reflections from the cell membrane and internal organelles and the influence of different refractive indices of the different cell organelles. It has found wide applications for vesicle spreading though [177]¹.

Setup of the 3 λ -RICM

Therefore, I installed a special optical RICM setup (fig. 5.2) on a standard inverted microscope (Axiovert200, Zeiss). The sample was illuminated by a Xenon lamp directed by two parallel iris-system within the microscope. The antireflex technique has been realized with an 63x oil objective (compare table 5.2) and the RICM filter cube (in position No. 17 in figure 5.1). The RICM cube (AHF) consists of a beam splitter 50R/50T VIS, two polarisation filters and one longpass blocking filter GG 420. The RICM filters (D490/10, D546/10 and D630/10 (AHF)) can either be placed in the motorized filter wheel (compare fig. 5.1 No. 16) enabling an easy, automated exchange for a standard RICM images, or they can be mounted in the special 3 λ -RICM cage system (Thorlabs, fig. 5.2) to image all three wavelengths simultaneously, where one wavelength is displayed on one camera (chapter 5.1.2), and the other two are displayed vertically split on the other camera. The whole system was covered with a custom built light protection system to ensure the best possible image quality. As the green and blue wavelength are detected on the same camera, the required exposure times should be very similar. Therefore we employed a Xenon lamp, which has a constant intensity over all wavelength. Faster acquisition times for the high intensity peaks of the mercury lamp can on the other hand be acquired with the HBO lamp (Zeiss).

¹and references within

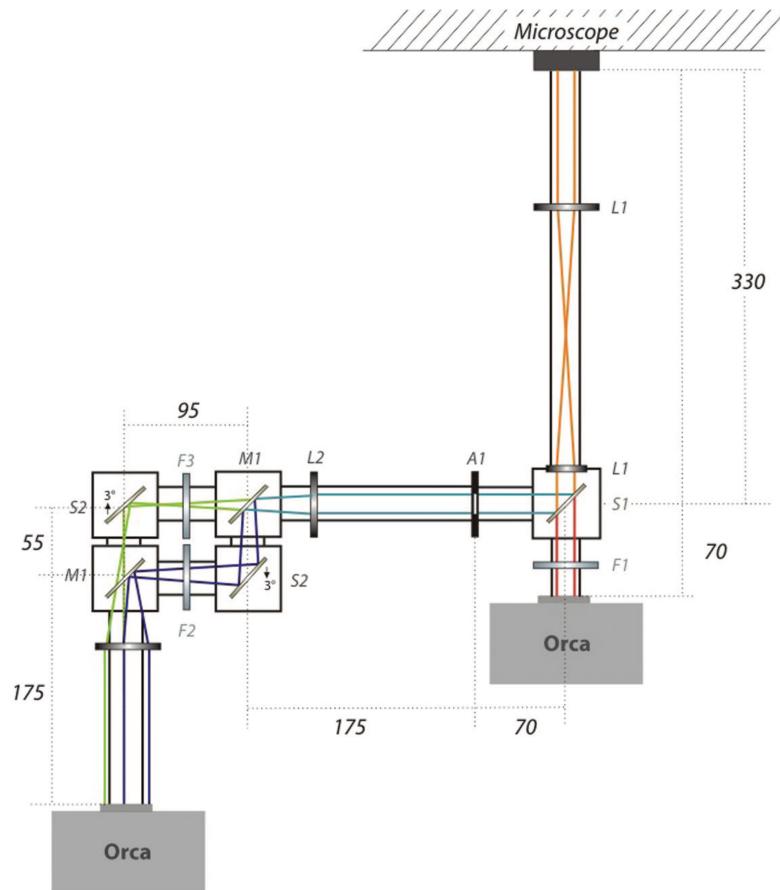


Fig. 5.2 – Setup of the 3λ -RICM cage system: The polychromatic light emerging from the microscope is separated by their wavelengths. A first telescope consisting of lens L1 ($f = 100$ mm) and L2 ($f = 125$ mm) transfers the image from the original camera position to the new camera position on the right. A second telescope performs the same operation for the second camera. The beamsplitter S1 (600DCXR, AHF) reflects light between 425-580 nm and allows light between 620-800 nm to pass through. The red light is filtered by the bandpass filter F1 (630/10) before it is imaged by the right camera. The light reflected at S1 passes through a beamsplitter corner, in which the light is split into the wavelength by the first longpass beamsplitter M1 (Q505 LP), which transmits light above 505 and reflects the rest. The blue light is subsequently filtered by the bandpass filter F2 (490/10) and the green light by F3 (546/10). The broadband mirrors S2 are tilted at a 3 degree angle to ensure a vertically split image on the camera. To prevent an overlay of these two images a special rectangular aperture A1 is inserted at the conjugated plane of the final camera position.

5.1.4 Spinning Disc Microscopy

The confocal spinning disc experiments were performed on an AxioVert200 M (Zeiss) equipped with a Perkin-Elmer Ultraview ER System with an Ar/Kr-Laser for 488 nm and 568 nm wavelengths and a water immersion objective (Zeiss, C-Apochromat, 40x, NA=1.1). The cell membrane and the erythrocytes were labeled using WGA555 and DiI and the hyaluronan using the GFPn fusion protein. Images were taken 4 μm above the surface with an ORCA-ER CCD camera (Hamamatsu) at an exposure time of 200 ms (568 nm) and 2500 ms (488 nm). Fluorescent profiles of the PCC were chosen perpendicular to the cell surface summed over a width of 10 pixels to reduce noise, where the fluorescent image of the membrane was applied to determine the cell surface, which was set to zero in the PCC profile.

5.2 Cultivating the Different Cells

All protocols involving cells were performed in a sterile hood (HeraSafe, Thermo) following standard sterile techniques to prevent contamination. All cells were incubated at 37°C and 5 % CO₂ atmosphere in an incubator (HeraCell, Thermo) if not noted otherwise. Cryo-storage was maintained in liquid nitrogen tanks. The cells were first frozen over night at -20°C or -80°C and then transferred to the liquid nitrogen tank.².

The cells are regularly checked for mycoplasma using a 0.01 % 4',6-Diamidino-2-phenylindol (DAPI) solution. This fluorescent dye intercalates into DNA and thus stains the nucleus as well as mycoplasmas (absorption maxima: 358 nm, emission maxima: 461 nm). It also binds to RNA, but the emission maxima (400 nm) in this case is much lower, so that RNA and mycoplasmas can be distinguished by the right choice of fluorescent filters. Samples are first fixed for 15 min in a DAPI-methanol solution, then washed with methanol for 5 min and finally rinsed 3 times for 5 min with PBS. Fluorescent images are taken with the DAPI-filter set.

If not noted otherwise, all cell culture solutions were purchased at Gibco, the cell culture flasks at Nunc and all other disposable plasticware at Greiner Bio-one.

5.2.1 Rat Chondrocyte Cell Line RCJ-P

Rat chondrocyte cells RCJ-P (rat chondrocytes from fetal calvaria, batch 15.01.98; Prochon Biotech, Rehovot, Israel) were kindly provided by *B. Geiger* (Weizman Institut, Rehovot, Israel). They were started at passage 2 and cultured no higher than passage 20. If not otherwise noted they were cultured in MEM alpha medium containing 15 % fetal bovine serum (FBS) and 2 % L-glutamine [28]. To prevent dedifferentiation they were split at maximal 90 % confluency. For cell splitting they were first washed with warm PBS (37°C) and then incubated for 4 min in a warm trypsin-EDTA 2.5%2 solution at 37°C. After diluting in 5 ml of media they were centrifuged at maximal 800 rpm at room temperature for 5 min. The cell pellet was then resuspended in media containing FBS and L-glutamin and plated in new tissue culture flasks or probe chambers.

For cryo-storage the cells were resuspended in FBS containing 10 % dimethylsulfoxid (DMSO) and 10 % alpha-MEM medium. After thawing the cells, no extra amount of FBS was added to the medium to keep culture conditions as constant as possible.

²it seems best to freeze them at -80°C, so all cells were frozen in the -80°C freezer after its installation in October 2006

Cultivating the RCJ-P in CO₂-independent media

To study the results of different media on the pericellular coat, cells were cultured in CO₂-independent medium containing 15 % FBS and 2 % L-glutamine at 37°C in an incubator without CO₂ atmosphere for two passages before sample preparation. The cells were otherwise treated the same as in MEM alpha medium.

Synchronisation of RCJ-P cells

For division experiments, the cells were first starved: The media was exchanged with media devoid of FBS for 8-10 hours. Cells were split and transferred to FBS containing medium afterwards. Most cells would then be dividing 5-6 hours after plating.

5.2.2 Primary Human Cells (HCH)

Primary human chondrocytes (HCH) were derived from the knee joint of a 57 year, Caucasian male (PromoCell, Lot-No.:1737). They have a population doubling time in log phase (h/PD) of 79.8 h and otherwise a population doubling time of ≤ 10 with a viability of approx. 84 %. They were cultured in chondrocyte growth media with SupplementMix (PromoCell). To prevent dedifferentiation they were split at maximal 80 % confluency. For cell splitting a DetachKit (PromoCell) was used at room temperature. The cells are first washed with HepesBSS (containing 30mM Hepes, D-Glucose, NaCl, KCl, NaPhosphate and Phenol Red) and are then incubated with Trypsin / EDTA solution for about 5 min at room temperature. After all cells have been detached the trypsin neutralizing solution (TNS) from soybean (0.05 %) is added and the cells are centrifuged at about 800 rpm for 5 min. After resuspension in growth media they are transferred to new culture flasks or probe chambers. For cryo-storage the cells were resuspended in FBS cryo solution (PromoCell).

HCH Cell Mycoplasma Treatment

The HCH cells were infected with mycoplasmas and therefore treated with BM-cyclin, (Boehringer). For two weeks 10 mg/ml of BM-cyclin 1 were added to the media every three days and afterwards 5 mg/ml of BM-cyclin 2 were added over two weeks every four days. The HCH cells did not survive the first treatment, but a freshly dethawed vial could successfully be treated. From these cells a new stock of cells was added to the cryo storage and subsequently used for all experiments.

5.2.3 Transfected HEK Cells (HK2GFP)

Transfected human embryonic kidney cells (HEK cells)³ termed HK2GFP are cultivated in a 1:1 mixture of D-MEM (Gibco) and F12 medium (Gibco) supplemented with 10 % FBS, 1 % L-glutamine and 0.01 % puromycin (10 mg/ml, ready made solution, Sigma). For cell splitting they were first washed with PBS and then incubated for 5 min in a trypsin-EDTA 2.5% (Gibco) solution at 37°C. After diluting in 5 ml of media they were centrifuged at about 1000 rpm at room temperature for 5 min. The cell pellet was then resuspended in media containing FBS and L-glutamine and plated in new tissue culture flasks (Nunc)). For cryo-storage the cells were resuspended in FBS containing 10 % DMSO. Since the HEK cell eventually lose the ability to produce GFPn, lots of cells were kept in cryo storage at early passages.

³kindly provided by U. Rauch, Uppsala University, Uppsala, Sweden

Harvesting the GFPn Enriched Media

After confluency is reached, about 80 % of the medium is replaced every two days with FBS-free medium. To purify the harvested medium from cells or cell fragments it is centrifuged at 2000 rpm for 20 min. One tablet of a protease inhibitor cocktail (PIC complete EDTA free, Roche) is added to 50 ml of supernatant and either frozen until further purification or immediately processed.

5.3 Cell Protocols

5.3.1 Preparing Cell Samples

To ensure healthy cells in combination with the possibility to easily reduce the amount of media for short time periods to 100-200 μ l for protein or staining experiments, a Teflon chamber has been designed that can serve both purposes (fig. 5.3). The circular glass slides (Wenzel) are glued to the Teflon chamber with vacuum grease (medium viscosity) after they had been cleaned with lint-free paper (Kimwipes).

During incubation of the cells, the sample holder is filled up completely with 3 ml of media. If not otherwise noted cells are allowed to adhere to the surface for 6 h prior to the experiment. Phenol-red free medium containing the required supplements is used for fluorescent microscopy to avoid background fluorescence by the media. In GFPn staining experiments, the growth medium is removed and 200 μ l of GFPn containing media are added into the small volume above the cells. The nanostructured surfaces

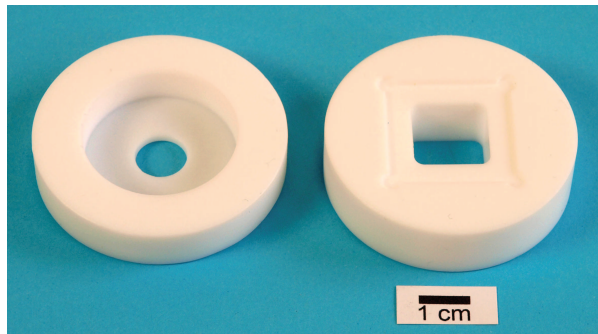


Fig. 5.3 – Teflon holder: for different cell experiments. The *GFPn holder* on the left ensures healthy cells by a total media volume of 3 ml which can easily be reduced to about 100-200 μ l for staining experiments. The sample holder on the right is ideally suited to observe cells on nanostructured surfaces, fitting a standard 24 x 24 mm glass slide which can be fixed with twinsil into the inset.

are prepared on 24 x 24 glass slides. To utilize the complete surface, they are glued to special rectangular teflon holders (fig. 5.3) with twinsil (Picodent), a two-component dentist's glue, that can be applied on wet surfaces.

5.3.2 Particle Exclusion Assay with Erythrocytes

The PEA should be performed with cleaned erythrocytes that can not lead to artefacts in the size or structure of the PCC. Such artefacts could be introduced for example through hyaladherins contained in the blood.

The erythrocytes are isolated from fresh 'food safe' pig (*Sus scrofa domestica*) blood provided by the veterinary service of the Fleischversorgungszentrum Mannheim.

The fresh blood, is directly transferred into a storage flask that contains 1.5 mg/ml EDTA as anticoagulant. The bottle is closed and gently turned (not shaken, to avoid foam) to ensure a good mixing of anticoagulant and blood. The blood is transported in a cooled box and stored in a refrigerator at 4°C, where it can be used for up to 48 h.

For the preparation of an erythrocyte sample a 50 ml falcon filled with blood is centrifuged at 4°C for 30 min at 1800 rpm. The erythrocytes sediment during this centrifugation and will form a dark red cushion in the lower part of the flask.⁴ This bottom layer is carefully transferred to a new falcon, mixed with ice cold PBS and the complete procedure is repeated at least two times.

The cleaned erythrocytes are diluted in media so that addition of one droplet to the sample will form a nice close monolayer not more than 8 μm in height.

5.3.3 Membrane Staining

The cell membrane of RCJ-P cells can be stained homogenously on living cells with dye conjugated wheat germ agglutinin (WGA). This carbohydrate-binding protein of approximately 36 kDa selectively recognizes sialic acid and N-acetylglucosaminyl sugar residues on the cell membrane. Molecular probes offers a wide variety of different conjugates, including different Alexa-dyes. The WGA dyes are employed at a concentration of 1.5%, incubated for five minutes and washed with twice with culture media.

Pig erythrocytes do not possess any of the WGA binding carbohydrates. Therefore they are stained with carbocyanine dyes DiO or DiI (Vybrant solutions, Invitrogen). About 10 μl of the dye solution are added to 1 ml of cleaned erythrocytes and centrifuge after 10 min incubation. They are washed at least three times to prevent co-staining of other cells.

5.3.4 Fixation of Adherent Cells

Mild fixation methods based on glutaraldehyde (Serva) do not destroy the interactions with hyaluronan and thus leave the PCC intact [24]. Adherent cells are incubated with a 1 % glutaraldehyde solution in PBS for 5 min. After the glutaraldehyde solution has been removed, the cells are immediately covered with a 1 % bovine serum albumin (BSA, fraction V, Serva) solution in PBS and washed twice with this solution over 5 min each.

As expected, the adhesion area is not affected by the fixation (table 5.4). Even though the fixation significantly influences the PCC size (table 5.3), the PCC should be affected similarly in all experiments, leading to comparable results, as long as all parameters are kept constant.

5.3.5 Hyaluronidase Treatment

The cells were incubated with *Streptomyces hyaluronidase* (Seikagaku Kogyo Corp., Tokyo, Japan), which is specific for hyaluronan and does not possess any additional proteolytic activities. The PCC is removed within seconds after addition of a solution in PBS adjusted to a final concentration of 0.2 mg/ml.

5.3.6 mCherry Actin Transfection of RCJ-P Cells

RCJ-P cells were transfected with vectors encoding mCherry labeled actin. The DNA plasmid was introduced into the cell following the lipofectamin protocol provided by Invitrogen. Afterwards the transfected cells produce labeled actin in addition to their

⁴On top of the erythrocytes one can see a thin white film of low density leukocytes, called the "buffy coat". The rest of the falcon is filled with a brownish-yellow coloured serum.

normal actin. Both monomers are incorporated into the actin structures of the cell, such as the stress fibers and the actin cortex. The applied fluorescent marker belongs to a new class of fluorescent proteins introduced by *R. Y. Tsien's* group in 2004 [178]. These so called mfruits exhibit very good fluorescent intensity, low bleaching and low toxicity [178, 179]. The DNA-vector encoding the mCherry-actin we used in our experiments was kindly provided by *Roger Y. Tsien* (University of California San Diego, USA).

The general protocol for transfecting cells with lipofectamin is well established, but needs to be adjusted to each cell type. The artificial liposomes consist of a mixture of neutral and cationic lipids that form complexes with the negatively charged DNA and are taken up by the cell. The liposomes sometimes cause cell death as does the introduced DNA plasmid. The cell count (table 5.5) with RCJ-P cells showed the expected 15% lethality rate due to the cationic lipids and no additional lethality caused by the plasmid.

After the transfection, the cells were transferred to standard medium containing growth factors. An hour later confocal images were taken (5.4). The successfully transfected cells showed a strong fluorescence homogenously distributed throughout the complete cell. At that time most cells were still round up and had not started to adhere. About 2 h later the fluorescent signal was still as strong and the cells appeared to be in the process of adhering to the surface. Although the actin seemed to be diffusely located throughout the cell, some structures with high intensity staining could be observed (fig. 5.4). If the transfection mixture was left on the cells for more than 4h, or if the cells were left to adhere for more than 4h after in medium containing serum, the staining appeared blotched and less intense.

RCJ-P cells were transfected with mCherry actin vectors with the help of lipofectamin (Invitrogen). Therefore the RCJ-P cells were plated in a 6-well plate at a concentration that would result in a confluency of 50-80 % overnight. Two samples of 125 μ l serum free alpha-MEM medium were prepared. 2 m/g of DNA was added to one of them and 5/ml of lipofectamin transfection agent was added to the other. Then the two solutions were combined, gently mixed and incubated for 30 min at room temperature. Subsequently 750 μ l of serum-free alpha-MEM were added to the incubated solution. The growth medium of the adhered cells was replaced with 1 ml of serum free alpha-MEM medium and the transfection mixture was added. The cells were then incubated at 37°C for 4-6 hours before they were split and replated in serum containing media.

For the determination of the induced lethality three different cell samples were prepared simultaneously with the same number of cells. One sample was transfected as described above. The treatment of the second differed in the absence of the DNA vector, whereas neither DNA nor lipofectamin were added to the third sample (positive

Table 5.3 – Adhesion area after 24 h on glass

	total number of cells	average adhesion area [μm²]	standard deviation
fixed	55	683	162
un-fixed	65	742	189

Table 5.4 – PCC area after 24 on glass

	total number of cells	average adhesion area [μm²]	standard deviation
fixed	55	773	198
un-fixed	65	871	211

Table 5.5 – Analysis of the lethality of transfection in RCJ-P cells. Negative control: untreated cells; positive control: lipofectamine treated cells; transfected sample: cells treated with lipofectamine and the mCherry-actin vector. The numbers correspond to the total number of cells.

positive control	307500
negative control	262500
transfected sample	262500

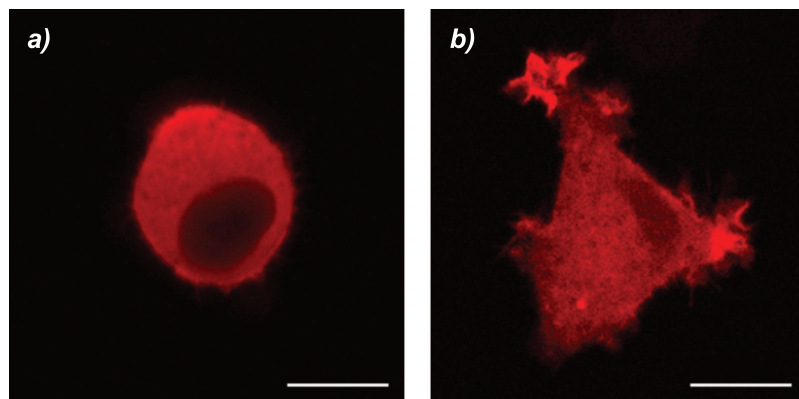


Fig. 5.4 – Confocal images of RCJ-P cells transfected with mCherry actin. Left: Cut through a cell about one hour after transferring cells to medium with growth factors. The actin is still homogeneously distributed within the cytosol. Right: Cell starting to adhere about two hours later. The first stress fibers can be observed directly above the surface especially on the 'arms of the cell'.

control). The number of cells after the completed procedure was counted in a Neubauer cytometer and the cell concentration per well determined.

5.3.7 Purification of the eGFP Labelled Link Module GFPn

The transfected HEK cells all show a strong fluorescence, stable over several passages. Confocal spinning disc images (fig. 5.5) prove the presence of GFPn inside the cells. The GFP intensity outside of the cell correspond to the general noise due to the presence of GFPn in media. Thus no strong PCC hinders the secretion of GFPn into the surrounding medium. Thus, the GFPn enriched medium is harvested every two days up to several weeks while the cells continue to grow in a thick epithelial layer.

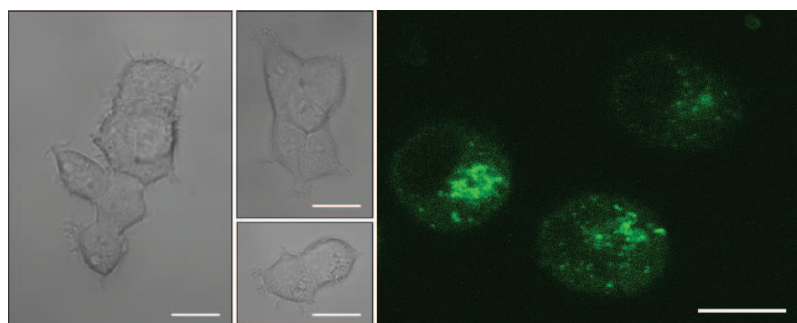


Fig. 5.5 – The transfected HEK cells (HK2GFP) typical form clusters. Images were taken in bright field mode; right: GFPn (green) producing cells do not show a fluorescent pericellular coat. Thus the GFPn is enriched in the media. The confocal image is taken through the middle of the HK2GFP cells. All size bars correspond to 10 μm .

The purification of GFPn is based on the affinity of nickel-nitriloacid (Ni-NTA) to form complexes with histidine residues. A 6x His tag was introduced in the GFPn sequence especially for this purpose.

The Ni-NTA agarose beads (Qiagen) are first washed twice in sterile PBS. Therefore 50 μl of Ni-NTA slurry are dissolved in 1 ml PBS, centrifuged for 2 min at 2000 rpm and resuspended in PBS. The equilibrated beads are then incubated in 50 μl of harvested media containing the GFPn (see 5.2.3) on a rotary wheel at 4°C for 2 h. The beads are separated from the media in a polypropylene column (Qiagen) and washed twice with 800 μl of wash buffer (table 5.6) to prevent unspecific absorption of other proteins. The GFPn is released from the beads with 100 μl of eluation buffer. To desalt the purified protein a dialysis cassette (Pierce, Slide-A-Lyzer 7 kDa cutoff, Cat. No. 66370) is applied.

To control the quality of the purification process the different fractions can be analysed in different ways. The fluorescence of the GFP (fig. 5.6) can be measured with a fluorimeter (Ex.: 488 nm, Em.: 510 nm). The amount of different proteins can be checked by SDS-Page analysis and the final protein concentration can be estimated by colorimetric essays like the Bradford test and the BCA or by calculating the ratio of the adsorption at 240 nm and 260 nm.

The final protein concentration can be estimated by colorimetric assays like the Bradford test and the bicinchoninic acid (BCA) assay or by calculating the ratio of the adsorption at 240 nm and 260 nm. The concentration in the purified sample ranges between 0.1 and 0.5 mg/ml.

Table 5.6 – Wash buffer solutions (adjusted to $pH = 8$ with NaOH)

50 mM	$\text{Na}_2\text{H}_2\text{PO}_4$	137.99 g/mol	6.90 g/l
300 mM	NaCl	58.44 g/mol	17.54 g/l
20 mM	imidazole	68.08 g/mol	1.36 g/l

Table 5.7 – Elution buffer solutions (adjusted to $pH = 8$ with NaOH)

50 mM	$\text{Na}_2\text{H}_2\text{PO}_4$	137.99 g/mol	6.90 g/l
300 mM	NaCl	58.44 g/mol	17.54 g/l
250 mM	imidazole	68.08 g/mol	17.00 g/l

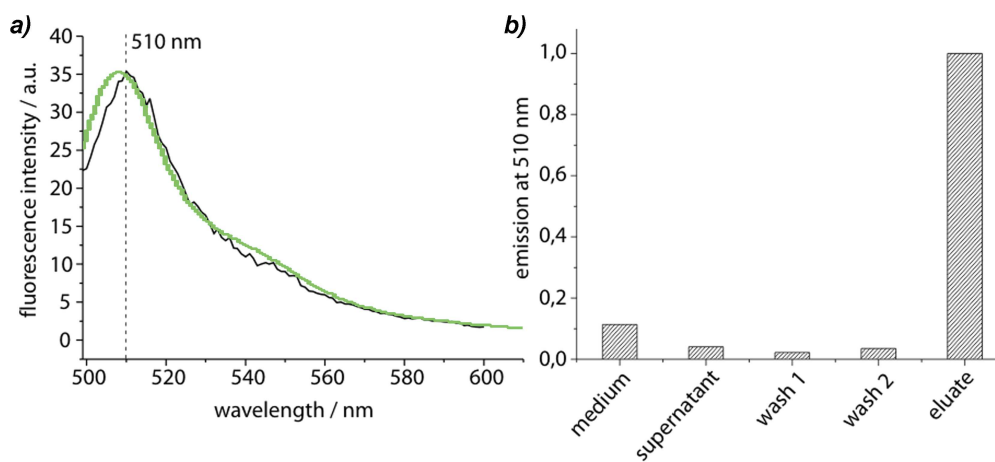


Fig. 5.6 – GFPn fluorescence: a) The fluorescence spectrum of GFPn (black line) corresponds well to that of unmodified eGFP (green - spectra for eGFP provided by Invitrogen). The spectrum was taken upon excitation at 488 nm. b) The GFPn can be enriched to a 100fold concentration. Normalized fluorescence intensity of the different fractions collected in the purification process are shown.

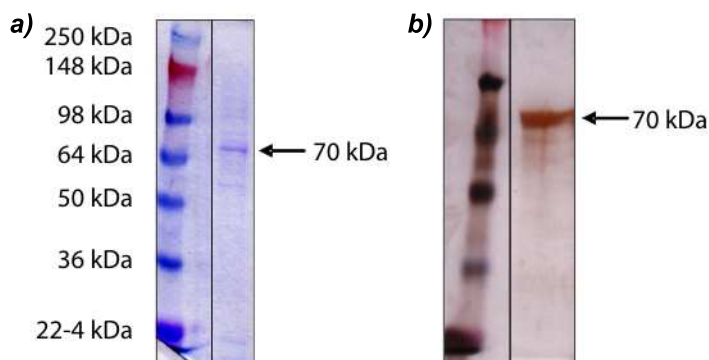


Fig. 5.7 – SDS page analysis of the eluate shows a clear band at 70 kDa. a) Coomassie staining and b) silver staining show the clear 70 kDa band of GFPn and little other proteins. Both gels have been run simultaneously with the ladder and placed next to each other for better comparability.

In a sodium dodecyl sulfate polyacrylamid gel electrophoresis (SDS-PAGE) the proteins are separated depending on their size. It is important to note, that the SDS denaturates the protein. Any attached hyaluronan will therefore not be detectable with this method. The amount of protein in the harvested medium is initially too low for SDS-Page. Therefore, the protein is first precipitated with trichloroacetic acid (TCA): 0.1 g TCA crystals are added to 1 ml of medium and gently vortexed. After 30 min of incubation on ice the eppendorf is centrifuged for 10 min at 13-15.000 rpm at 4°C. The supernatant is removed and the pellet is dissolved in 500 μ l of ethanol. The washing step is repeated. The pellet is dried on a speedvac and then resuspended in 20 μ l of sample buffer, ready to be added to the gel. For the SDS-Page analysis the following Invitrogen products were used together with the Invitrogen electrophoresis power supply:

Novex-Tris-Glycine Gels, 10%, 12 well (EC60752BOX)

Novex Tris-Glycine SDS sample buffer, 20ml, 2x (LC2676)

The GFPn protein has a molecular weight of about 70 kDa. Its band can be observed after staining the gels either with Coomassie or by a silver staining (fig. 5.7).

For rapid testing of the GFPn purification a dot-blot using anti-His antibodies is used. As shown in fig. 5.8, the final eluates contain a high concentration of the purified fusion protein. As expected, the concentration diminishes in the subsequent eluations, leaving only a small amount of protein in eluate 3. It can also be observed, that some fusion protein seems to flow through the columns after being coupled to the NTA beads, as well as in the washing process.

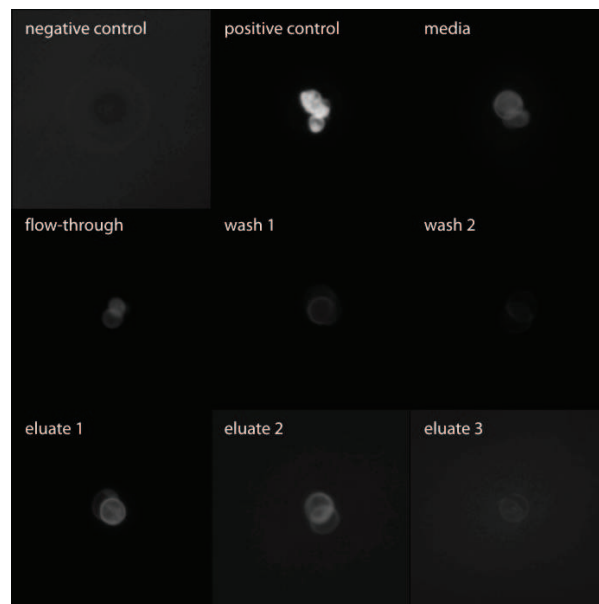


Fig. 5.8 – Dot Blot using anti-His tag antibodies to detect GFPn in the different fractions of the GFPn purification

5.4 Microrheology

5.4.1 Microrheology Chamber

In a typical microrheological setup the Brownian motion of the embedded particle would be influenced by flow or evaporation and the solution might be affected by oxidation. Therefore the chamber needs to be sealed airtight preventing enclosed air bubbles. These criteria require special probe chambers for passive Microrheology. To visualize the movement of the particles the chamber needs to be suitable for microscopic imaging, best preventing any additional reflexes that would reduce the image quality. Additionally, precious protein solutions call for the ability to perform measurements of small sample sizes. The employed microrheology chambers are assembled out of glass slices fixed with transparent UV glue (fig. 5.9). After the chamber is filled with about $5 \mu\text{l}$ of sample solution containing the beads, it is sealed with vacuum grease.

The temperature is controlled by a heatable microscope stage that allows access of the objective through a hole on the bottom. It is otherwise closed and thus prevents air currents. It can also be darkened easily to enhance the sensitivity of fluorescence imaging.

Microrheology chambers of different heights were tested. It turned out, that a height of 1 mm sometimes leads to convective flow within the chamber. This might be caused by a thermal gradient between the upper part of the chamber that was heated and the bottom part in contact with the immersion oil or water of the objective that was not temperature controlled. Chambers with a height of about $150 \mu\text{m}$ did not show any flow at any height if they were properly sealed and no air bubbles were enclosed (fig. 5.9). This height is still sufficient to measure far away from any walls to ensure that the stoke's drag is neglectable.

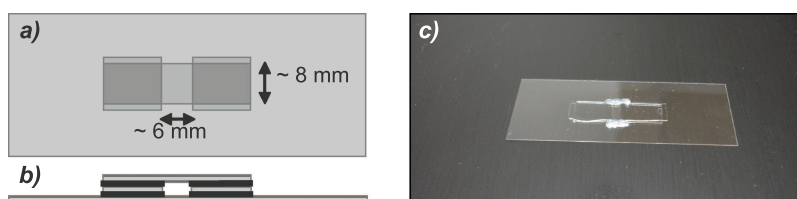


Fig. 5.9 – Design of the transparent, airtight microrheology chambers: a) top view: two small glass pieces are glued on a supporting glass slide and covered with a longer piece. b) side view: the glue (black lines) seals the attachment area above and below the sidepieces. Height of the resulting chamber: $150 \mu\text{m}$. c) photo of a microrheology chamber filled with sample and sealed with vacuum grease.

To prevent adsorption of sample polymers on the chamber walls that might change the physical properties of the solution or the effective concentration the glass pieces are passivated with BSA if protein samples are measured.

5.4.2 Tracer Particles

The tracer particles chosen for passive particle tracking microrheology need to fulfill a couple of criteria concerning their size, material and surface chemistry. The size of the bead should be chosen according to the desired measurement properties. But it also needs to be adequate for the precise determination of the bead's position. The position can be defined best, if the size of the bead corresponds to 5 to 20 pixels which of course also depends to a certain extend on the employed magnification. For bright field visualization in our microrheology setup a minimal size of 750 nm is required. The position determination of smaller beads can still be achieved if fluorescent beads are

used. Due to their longer exposure time the accessible framerates will be lower resulting in a smaller range of frequency of the acquired loss and storage moduli. Fluoresbright polystyrene particles (Polyscience, Heidelberg) can be recorded at a maximal frame rate of 1000 fps and are still precisely detectable down to a size of 400 μm . These beads also have the desired monodispersity.

Beads in the micron range with a good monodispersity can be made of polystyrene or silica. The choice of material influences the weight of the particle and therefore the settling rate. Polystyrene beads have a density similar to water (1.0 g/ml), whereas silica particles have a higher density (1.96 g/ml). Therefore measurements with 1 μm polystyrene beads can be performed over several hours, whereas 1 μm silica beads will sink out of the field of view in about an hour.⁵ The different refractive indices (1.6 at 589 nm for polystyrene beads vs. 1.4 for silica beads) additionally leads to different appearances in the microscope. For the passive particle tracking microrheology experiments only polystyrene beads were employed.

The chemical composition of the beads also influences their surface chemistry and therefore their adsorption properties. Polystyrene beads are available with different functional groups. To prevent adsorption of proteins polystyrene beads can additionally be functionalized with polyethylenglycol [180]. Adsorption of polymers should generally be avoided since it might change the physical properties of the solution and may also lead to bridging flocculation. For the measurements in glycerin-water solution different surface functionalizations were tested.

The concentration of beads within the probe should be high enough to have as many beads in the field of view as possible. Adding beads diluted in water also changes the sample and should thus be considered during sample preparation. For two-point microrheology the concentration should be chosen according to a sufficient range of interparticle distances. *Gardel et. al.* [54] have worked with distances between 3 and 30 μm . Therefore a concentration of about 5×10^8 beads/ml is used. To ensure that the beads are not aggregated before they are added to the sample, they are sonicated for 1 min, always stored at 4°C and all buffer solutions are freshly prepared or thawed.

5.4.3 Microscope Setup

Accurate particle tracking is based on well adjusted image acquisition. The center of a particle is best recognized if the particle shows a Gaussian intensity distribution. If the beads are recorded in bright field illumination the refraction of the light will only lead to a Gaussian distribution of light intensity, if the illumination is adjusted correctly under the conditions set forth by *August Koehler* (1866-1948) [170].

Particles have to be recorded with a large enough distance to any wall to ensure that wall effects are neglectable. Therefore the center of the microrheology chamber was set into focus corresponding to a height of about 75 μm above the bottom glass slide. To achieve the best resolution of the imaged beads different objectives were compared. Generally water or glycerin immersion objective are suited better than oil immersion objektives, which face additional aberrations when focusing into a water sample. Water objectives also have the advantage that they can be adjusted to the thickness of the cover slide and the temperature⁶.

⁵The sinking velocity for 1 μm particles in water at 20°C can be calculated by Stoke's law: $2.77 \cdot 10^{-6}$ cm/sec for polystyrene beads, $5.26 \cdot 10^{-4}$ cm/sec for silica particles.

⁶the refractive index of the immersion oil changes at higher temperatures leading to additional aberrations with an oil immersion objective

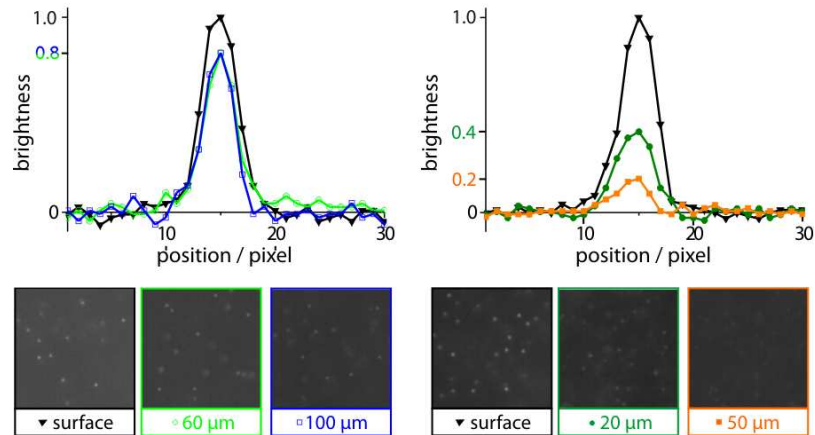


Fig. 5.10 – Water immersion objectives are better suited for focusing into an aqueous solution containing fluorescent beads than oil immersion objectives: $0.75 \mu\text{m}$ Fluoresbriht Yellow polystyrene beads in aqueous solution were imaged with a (left) 40x water immersion objective in a combination with a 2.5 optovar resulting in a 100x magnification and a (right) 100x oil immersion objective. For easier comparison normalized profiles through a bead at different distances to the surface are depicted. The signal-to-noise ratio is only slightly reduced by focusing into the aqueous solution with a water immersion objective, but drastically decreased with an oil immersion objective.

Advantages and Disadvantages of Water and Oil Immersion Objectives

Polystyrene beads of at least $0.75 \mu\text{m}$ can be visualized nicely with the Zeiss 40x/1.2 W Korr infinity/0.14-0.18 objective in combination with a 2.5 optovar leading to an effective magnification of 100-times. Even if the beads are imaged within the sample the signal-to-noise ratio is hardly affected (fig. 5.10).

To image beads of less than $0.75 \mu\text{m}$ a 100-times magnification as achieved with the 40x water objective in combination with the 2.5 optovar is no longer sufficient. Therefore the quality of the image resolution with a 100x objective in combination with the 2.5 optovar was tested. Images were taken with the same exposure time ($9400 \mu\text{s}$) on the Phantom camera in an aqueous solution (fig. 5.10). The sample was only illuminated during the recording time (only one picture taken). Therefore, the overall fluorescent was stable as also checked by a second set of images taken afterwards. The best image is achieved directly above the surface of the glass cover slip. Focusing into the sample decreases the signal-to-noise ratio dramatically (fig. 5.10). However, the beads can still be imaged at a focus depth of up to $20 \mu\text{m}$, which is sufficient for bead tracing.

5.4.4 Calibration with Solutions of Known Properties

Glycerol (also termed glycerin or propantriol, figure 5.11) is easily soluble in water forming a purely viscous solution. The viscosity of this solution can be precisely adjusted by the temperature and the weight percentage of glycerol in water (fig. 5.11). The different viscosities are well tabulated [181]. Therefore, the accuracy of the passive particle-tracking microrheological measurements was tested on different glycerol-water solutions.

The weight percentage of glycerin (P) in the solution depends on the density of glycerin (d_g) and water (d_w) and their amounts (g and w):

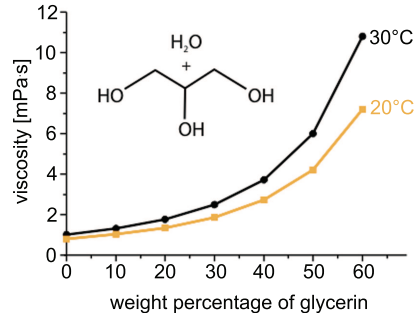


Fig. 5.11 – The viscosity of water-glycerin solutions depends on the percentage of glycerin as well as on the temperature. The chemical structure of glycerin is shown in the inset. The viscosity data is taken from ??.

$$P = \frac{d_g \cdot g}{d_g \cdot g + d_w \cdot w} \quad (5.2)$$

During preparation of the solutions careful attention was paid to keeping the original, strongly hygroscopic glycerin solution water free. The accurate amount of the highly viscous glycerin was measured with the help of a special pipette (Eppendorf).

The viscosity of glycerol water solutions has been successfully measured with passive particle tracking microrheology. I tested different sizes of beads and different imaging modes to find possible error sources.

Table 5.8 – Measured viscosity with MR at different exposure times

exposure time	viscosity [mPa · s]
300	3.5
400	3.7
450	3.8
500	3.3
600	3.2

5.4.5 Microrheology within the PCC of Living Cells

The RCJ-P cells are prepared in the sample holders (compare 5.3.1) and allowed to adhere in the incubator for 6 h. The cells are first checked for contamination that would not be visible later on when the beads are added. Then the medium is removed and 200 μl of fresh media containing 3 μl of fluorescent beads and 3 μl of membrane dye (WGA350) is added. After 5 min incubation time the chamber is filled up with additional 2-3 ml of fresh media. The fresh media contains the required amount of FBS and L-glutamine and is warmed to about 37°C. The chamber is positioned inside the heating table of the microscope. If not otherwise noted the microscope is used with the 63x DIC objective in combination with the 1.0x or 1.6x optovar and the filter is chosen as specified earlier. The cell surface is defined visually by focusing through the sample. The height moved upwards for imaging is specified by the microscopes motorized objective holder and within 0.1 /m accuracy. Image acquisition was performed

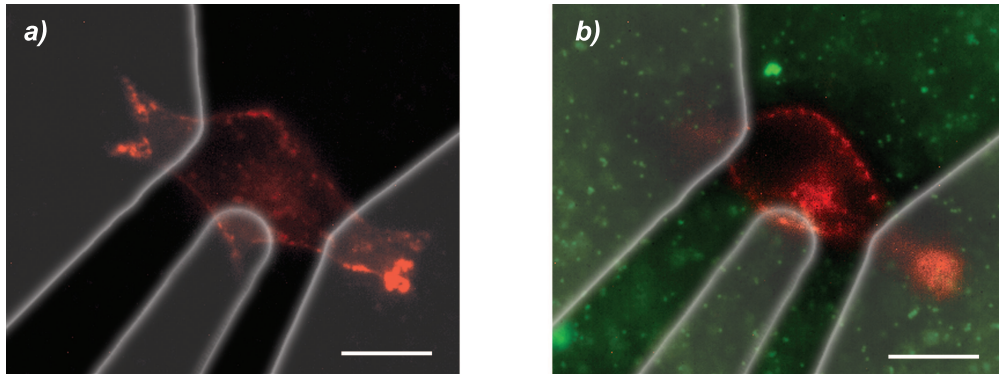


Fig. 5.12 – With the help of the WGA350 stained cell membrane (blue) at the surface of the glass slide (left) presumably motile regions of the cell are identified and marked. The movement of the green fluorescent tracer particles is observed 5/ μ m above the surface (left).

with the Phantom camera and analysis with a combination of the already described IDL programs and self-written IDL programs.

The fluorescent staining of the pericellular coat with GFPn and the particle exclusion assays suggest an inhomogenous amount of pericellular coat on cell protrusions. Therefore these areas are first identified on the image of the cell taken at the surface of the glass slide. The excluded areas (marked by white lines and white shading in fig. 5.12) are chosen to be perpendicular to the cell surface or excluding an area of at least $5\mu\text{m}$ around a small filopodia (thin arm).

The MSD is calculated for each track individually. For easier comparison of these tracks the local slope at 0.005 - 0.05 s and the local value at 0.01 s are calculated. The two dimensional MSD was calculated for each individual track and the values were subsequently multiplied by $3/2$ to obtain the three dimensional MSD [68]. In order to compare the MSD values at different positions they are compared at one specific lag time τ .

5.5 Surface Preparation

5.5.1 Cleansing of Glass Surfaces

Generally, all 24x24 glass slides (No. 1, Roth) were cleaned with freshly prepared piranha solution, consisting of 1 part hydrogenperoxide solution (30 % p.a., Merck) and 2 parts concentrated sulfuric acid (Merck). Therefore the glass surfaces are placed in a special teflon holder to enable the simultaneous cleansing of several glass slides. After an incubation time of at least an hour, the glass slides are transferred to milliQ water in their holder and washed at least three times. After a 5 min ultra sound treatment the water is replaced again and the glass slides are dried in a nitrogen stream right before further usage.

5.5.2 Fibronectin- and Collagen-Coating of Glass Surfaces

The cleaned glass slides are coated with $5\mu\text{g}/\text{cm}^2$ of fibronectin (bovine, Sigma-Aldrich). Therefore the buffered (0.5 M NaCl, 0.05 M TRIS, pH 7.5) stock solution (1 mg/ml) is diluted with PBS to a final concentration of $50\mu\text{g}/\text{ml}$. The surfaces are covered with $100\mu\text{l}/\text{cm}^2$ of this solution and incubated for 30 min in the incubator

granting a humid, warm atmosphere. After careful removal of the solution the surfaces are immediately employed in cell experiments.

In order to coat cleaned glass surfaces with collagen type II from articular bovine tissue (BD Biosciences), the acetic acid stock solution (3.48 mg/ml) is diluted to 50 $\mu\text{g}/\text{ml}$. This solution is incubated with 100 $\mu\text{l}/\text{cm}^2$ for one hour at room temperature. Afterwards the surface is washed repeatedly to remove the acetic acid.

5.5.3 Thin Film Coating with a Sputter Coater

Prior the SEM measurement, nanostructured glass surfaces are coated with a thin layer of carbon and critically point-dried cells with a thin gold layer to render the surfaces conductive and thus detectable in the SEM (Bal-TEC Med020 Modular High Vacuum Coating System, Witte).

Glass slides are coated with a thin gold layer by sputtering them first with a thin titan layer of about 3 nm ($1.2 \cdot 10^2$ mbar Ar pressure, 120 mA for 20 sec.) to enhance the stability of the subsequently sputtered gold layer with a thickness of about 15 nm ($5 \cdot 10^2$ mbar Ar pressure, 30 mA for 50 sec.).

5.5.4 Nanostructured Surfaces

The gold loaded micellar solution were prepared inside a glove box (M. Braun, nitrogen as processing gas) with different solvents. Toluene (p.a., Merck) as well as the xylenes (p.a., pure isomers, Merck) were dried over a 3 Å molecular sieve. Poly(styrene(x)-*block*-(2-vinylpyridine)(y)), abbreviated to PS(x)-*b*-P2VP(y), diblock copolymers are dissolved in the dried solvent to a final concentration of 5 mg/ml. After stirring the solution for 24 h to obtain uniform micelles, the gold salt is added. The amount of required gold salt depends on the loading L :

$$L = \frac{n[\text{HAuCl}_4]\text{VP}}{m(\text{VP})} \quad (5.3)$$

Thus the amount of gold salt to be added can be determined:

$$m(\text{HAuCl}_4 \cdot 3\text{H}_2\text{O}) = \frac{m(\text{polymer})}{M(\text{polymer})} \cdot (\text{VPunits} \cdot L) \cdot M(\text{HAuCl}_4 \cdot 3\text{H}_2\text{O}) \quad (5.4)$$

Within this thesis, different diblock copolymers have been employed. Mostly PS(1056)-*b*-P2VP(495) abbreviated as 1056er polymer. Comparative measurements have been carried out with PS(501)-*b*-P2VP(235), abbreviated as 501er, and PS(2076)-*b*-P2VP(571) abbreviated to 2076er. After addition of the tetrachloroaurate(III)-trihydrate to the solution with a loading of 0.5, the solution is stirred for another 24 h to ensure a homogenous distribution of the gold salt inside the micellar cores.

The cleaned glass slides were dip-coated into the micellar solution with a home-build machine allowing to adjust the immersion and retraction speed and ensuring the right immersion angle of the glass slide in relation to the solution surface.

Passivation with mPEG2000-Urea

The area between the gold particles is covalently passivated with a thin layer of mPEG2000-urea. After a brief activation in hydrogen plasma (5 min, 0.4 mbar H₂, 150 W) the nanostructured glass surfaces are immersed in a 1 mM solution of the linear polyethylene glycol, mPEG2000-urea, (CH₃-(O-CH₂-CH₂)₄₃-NH-CO-NH-CH₂-CH₂-CH₂-Si(OEt)₃) in dry toluene (p.A. from Merck) with 0.05% triethylamine (Sigma) at 80°C in nitrogen atmosphere for at least 16 hours. To remove non-covalently bound PEG molecules, the substrates are rinsed extensively with ethyl acetate and methanol (p.a. from Aldrich) before they are further functionalized.

RGD Functionalization

The gold particles or homogenous gold layers are biofunctionalised after passivation by an incubation with a 25 μM aqueous solution of the c(-RGDfK-) thiol(= c[RGDfK(Ahx-Mpa)]) provided kindly by *Prof. Kessler* for 4 hours. Subsequently, the samples are rinsed with MilliQ-water and shaken for 24 hours to remove the non-covalently bound c(-RGDfK-) thiols exchanging the MilliQ-water three times. Finally they are placed in PBS solution and not allowed to dry while the glass slides are fixed to the teflon holders and the cell suspension is added on the glass slides.

Bibliography

- [1] B Alberts, A Johnson, P Walter, J Lewis, M Raff, and K Roberts. *Molecular Biology of the Cell*. Taylor and Francis, 5th edition, 2008.
- [2] E Sackmann. *Handbook of Biological Physics*, volume 1(A), chapter Biological membranes - architecture and function, pages 1–62. Elsevier Science B.V., 1995.
- [3] T K Lindhorst. *Essentials of Carbohydrate Chemistry and Biochemistry*. Wiley, 2000.
- [4] D Boal. *Mechanics of the Cell*. Cambridge Univ. Pr., 2002.
- [5] B J Clarris and J R Fraser. On the pericellular zone of some mammalian cells in vitro. *Exp. Cell Res.*, 49:181–93, 1968.
- [6] M Mammen, S K Choi, and G M Whitesides. Polyvalente Wechselwirkungen in biologischen Systemen: Auswirkungen auf das Design und die Verwendung multivalenter Liganden und Inhibitoren. *Angew. Chem.*, 110:2908–2953, 1998.
- [7] S Sabri, M Soler, C Foa, A Pierres, A M Benoliel, and P Bongrand. Glycocalyx modulation is a physiological means of regulating cell adhesion. *J. Cell Sci.*, 113:1589–1600, 2000.
- [8] M Smith, D Long, E Damiano, and K Ley. Near-wall μ -PIV reveals a hydrodynamically relevant endothelial surface layer in venules in vivo. *Biophys. J.*, 85:637–645, 2003.
- [9] S P Evanko, M Tammi, R H Tammi, and T N Wight. Hyaluronan-dependent pericellular matrix. *Adv. Drug Deliv. Rev.*, 59(13):1351–1365, 2007.
- [10] B P Toole. Hyaluronan in morphogenesis. *Sem. Cell Dev. Bio.*, 12(2):79–87, 2001.
- [11] R Kosaki, K Watanabe, and Y Yamaguchi. Overproduction of hyaluronan by expression of the hyaluronan synthase HAS2 enhances anchorage-independent growth and tumorigenicity. *Cancer Res.*, 59(5):1141–1145, 1999.
- [12] M P Maleski and C B Knudson. Hyaluronan-mediated aggregation of limb bud mesenchyme and mesenchymal condensation during chondrogenesis. *Exp. Cell Res.*, 225(1):55–66, 1996.
- [13] K Rilla, M J Lammi, R Sironen, K Toeronen, M Luukkonen, V C Hascall, R J Midura, M Hyttinen, J Pelkonen, M Tammi, and R H Tammi. Changed lamellipodial extension, adhesion plaques and migration in epidermal keratinocytes containing constitutively expressed sense and antisense hyaluronan synthase 2 (Has2) genes. *J. Cell Sci.*, 115:3633–3643, 2002.

- [14] J Bakkers. Has2 is required upstream of Rac1 to govern dorsal migration of lateral cells during zebrafish gastrulation. *Development*, 131(3):525–537, 2004.
- [15] C Ricciardelli, D L Russell, M P Ween, K Mayne, S Suwivat, S Byers, V R Marshall, W D Tilley, and D J Horsfall. Formation of hyaluronan- and versican-rich pericellular matrix by prostate cancer cells promotes cell motility. *J. Biol. Chem.*, 282(14):10814–10825, 2007.
- [16] N Itano, F Atsumi, T Sawai, Y Yamada, O Miyaishi, T Senga, M Hamaguchi, and K Kimata. Abnormal accumulation of hyaluronan matrix diminishes contact inhibition of cell growth and promotes cell migration. *Proc. Natl. Acad. Sci. USA*, 99(6):3609–3614, 2002.
- [17] A Zoltan-Jones, L Huang, S Ghatak, and B P Toole. Elevated hyaluronan production induces mesenchymal and transformed properties in epithelial cells. *J. Biol. Chem.*, 278(46):45801–45810, 2003.
- [18] S Meran, S Enoch, R Steadman, A O Phillips, D Thomas, and P Stephens. Involvement of hyaluronan in regulating fibroblast differentiation. *J. Biol. Chem.*, 282(35):25687–25697, 2007.
- [19] S P Evanko, J C Angello, and T N Wight. Formation of hyaluronan- and versican-rich pericellular matrix is required for proliferation and migration of vascular smooth muscle cells. *Arterioscler Thromb Vasc. Biol.*, 19(4):1004–1013, 1999.
- [20] M Brecht, U Mayer, E Schlosser, and P Prehm. Increased hyaluronate synthesis is required for fibroblast detachment and mitosis. *Biochem. J.*, 239(2):445–450, 1986.
- [21] K Rilla, R Tiihonen, A Kultti, M Tammi, and R H Tammi. Pericellular hyaluronan coat visualized in live cells with a fluorescent probe is scaffolded by plasma membrane protrusions. *J. Histochem. Cytochem.*, 56:901–910, 2008.
- [22] S Adamia, C A Maxwell, and L M Pilarski. Hyaluronan and hyaluronan synthases: potential therapeutic targets in cancer. *Current Drug Targets*, 5:3–14, 2005.
- [23] M Cohen, Z Kam, L Addadi, and B Geiger. Dynamic study of the transition from hyaluronan- to integrin-mediated adhesion in chondrocytes. *EMBO J.*, 25(2):302–311, 2006.
- [24] C B Knudson. Hyaluronan receptor-directed assembly of chondrocyte pericellular matrix. *J. Cell Biol.*, 120(3):825–834, 1993.
- [25] W H McBride and J B Bard. Hyaluronidase-sensitive halos around adherent cells. Their role in blocking lymphocyte-mediated cytolysis. *J. Exp. Med.*, 149(2):507–15, 1979.
- [26] A Blom, H Pertoft, and E Fries. Inter-alpha-inhibitor is required for the formation of the hyaluronan-containing coat on fibroblasts and mesothelial cells. *J. Biol. Chem.*, 270(17):9698–9701, 1995.
- [27] J B Leach C E Schmidt. Hyaluronan. *Encyclopedia Biomat. Biomed. Eng.*, pages 779–789, 2004.
- [28] M Cohen, E Klein, B Geiger, and L Addadi. Organization and adhesive properties of the hyaluronan pericellular coat of chondrocytes and epithelial cells. *Biophys. J.*, 85(3):1996–2005, 2003.

- [29] C A de la Motte, V C Hascall, J Drazba, S K Bandyopadhyay, and S A Strong. Mononuclear leukocytes bind to specific hyaluronan structures on colon mucosal smooth muscle cells treated with polyinosinic acid:polycytidylic acid: Inter-alpha-trypsin inhibitor is crucial to structure and function. *Am. J. Pathol.*, 163(1):121–133, 2003.
- [30] W Selbi, C de la Motte, V Hascall, and A Day. Characterization of hyaluronan cable structure and function in renal proximal tubular epithelial cells. *Kidney Int.*, 2006.
- [31] V C Hascall, A K Majors, C A de la Motte, S P Evanko, A Wang, J A Drazba, S A Strong, and T N Wight. Intracellular hyaluronan: a new frontier for inflammation? *Biochim. Biophys. Acta*, 1673:3–12, 2004.
- [32] T Jokela, A Lindgren, K Rilla, E Maytin, and V Hascall. Induction of hyaluronan cables and monocyte adherence in epidermal keratinocytes. *Conn. Tissue Res.*, 49:115–119, 2008.
- [33] K Meyer and J W Palmer. The polysaccharide of the vitreous humor. *J. Biol. Chem.*, 107(3):629–634, 1934.
- [34] B Weissmann and K Meyer. Structure of hyaluronic acid: The glucuronic linkage. *J. Am. Chem. Soc.*, 74(18):4729–4729, 1952.
- [35] B Weissmann and K Meyer. The structure of hyalobiuronic acid and of hyaluronic acid from umbilical cord. *J. Am. Chem. Soc.*, 76(7):1753–1757, 1954.
- [36] P Prehm. *Biotechnology of Biopolymers*, chapter 5: Hyaluronan, pages 379–399. Wiley-VCH, 2002.
- [37] P L DeAngelis. Hyaluronan synthases: fascinating glycosyltransferases from vertebrates, bacterial pathogens, and algal viruses. *Cell. Mol. Life Sci.*, 56(7):670–682, 1999.
- [38] P H Weigel, V Hascall, and M Tammi. Hyaluronan synthases. *J. Biol. Chem.*, 272(22):13997–14000, 1997.
- [39] P H Weigel and P L DeAngelis. Hyaluronan synthases: A decade-plus of novel glycosyltransferases. *J. Biol. Chem.*, 282(51):36777–36781, 2007.
- [40] B P Toole. Hyaluronan: from extracellular glue to pericellular cue. *Nat. Rev. Cancer*, 4(7):528–539, 2004.
- [41] M Tammi, A J Day, and E A Turley. Hyaluronan and homeostasis: a balancing act. *J. Biol. Chem.*, 277(7):4581–4584, 2002.
- [42] N Itano, T Sawai, M Yoshida, P Lenas, Y Yamada, M Imagawa, T Shinomura, M Hamaguchi, Y Yoshida, Y Ohnuki, S Miyauchi, A P Spicer, J A McDonald, and K Kimata. Three isoforms of mammalian hyaluronan synthases have distinct enzymatic properties. *J. Biol. Chem.*, 274(35):25085–25092, 1999.
- [43] H Chao and A P Spicer. Natural antisense mRNAs to hyaluronan synthase 2 inhibit hyaluronan biosynthesis and cell proliferation. *J. Biol. Chem.*, 280(30):27513–27522, 2005.
- [44] A J Day and G D Prestwich. Hyaluronan-binding proteins: tying up the giant. *J. Biol. Chem.*, 277(7):4585–4588, 2002.
- [45] A J Day and J K Sheehan. Hyaluronan: polysaccharide chaos to protein organisation. *Curr. Opin. Struc. Bio.*, 11:617–622, 2001.

- [46] J Kahmann, R O'Brien, J Werner, and D Heinegard. Localization and characterization of the hyaluronan-binding site on the link module from human TSG-6. *Structure*, 8:763–774, 2000.
- [47] L Ng, A Grodzinsky, J Sandy, A Plaas, and C Ortiz. Individual cartilage aggrecan macromolecules and their constituent glycosaminoglycans visualized via atomic force microscopy. *J. Struct. Bio.*, 143:242–257, 2003.
- [48] M Bathe. A coarse-grained molecular model for glycosaminoglycans: Application to chondroitin, chondroitin sulfate, and hyaluronic acid. *Biophys. J.*, 88(6):3870–3887, 2005.
- [49] C A Poole. Articular cartilage chondrons: form, function and failure. *J. Anatomy*, 191:1–13, 1997.
- [50] A Benninghoff. Form und Bau der Gelenkknorpel in ihren Beziehungen zur Funktion. *Cell Tissue Res.*, 2(5):783–862, 1925.
- [51] P van der Kraan, P Buma, T van Kuppevelt, and W B van der Berg. Interaction of chondrocytes, extracellular matrix and growth factors: relevance for articular cartilage tissue engineering. *Osteoarthritis Cart.*, 10:631–637, 2002.
- [52] E Zimmerman, B Geiger, and L Addadi. Initial stages of cell-matrix adhesion can be mediated and modulated by cell-surface hyaluronan. *Biophys. J.*, 82(4):1848–1857, 2002.
- [53] M Cohen, D Joester, I Sabanay, L Addadi, and B Geiger. Hyaluronan in the pericellular coat: an additional layer of complexity in early cell adhesion events. *Soft Matter*, 327(3):327–332, 2007.
- [54] M L Gardel, M T Valentine, and D A Weitz. *Microscale Diagnostic Techniques*, chapter Microrheology, pages 1–50. Springer-Verlag, Berlin, 2005.
- [55] F C MacKintosh and C F Schmidt. Microrheology. *Curr. Opin. Coll. Inter. Sci.*, 4:300–307, 1999.
- [56] T A Waigh. Microrheology of complex fluids. *Rep. Prog. Phys.*, 68:685–742, 2005.
- [57] V Breedveld and D Pine. Microrheology as a tool for high-throughput screening. *J. Mat. Sci.*, 38:4461–4470, 2003.
- [58] R R Brau, J M Ferrer, H Lee, C E Castro, B K Tam, P B Tarsa, P Matsudaira, M C Boyce, R D Kamm, and M J Lang. Passive and active microrheology with optical tweezers. *J. Opt. A: Pure Appl. Opt.*, 9(8):S103–S112, 2007.
- [59] J Sato and V Breedveld. Transient rheology of solvent-responsive complex fluids by integrating microrheology and microfluidics. *J. Rheol.*, 50(1):1–19, 2005.
- [60] R Brown. A brief account of microscopical observations made in the months of june, july, and august, 1827, on the particles contained in the pollen of plants; and on the general existence of active molecules in organic and inorganic bodies. *Phil. Magazine N*, pages 161–173, 1828.
- [61] R Brown. Additional remarks on active molecules. *Phil. Magazine N*, pages 161–166, 1829.
- [62] E Nelson. *Dynamical Theories of Brownian Motion, Mathematical Notes, Princeton University Press.*, volume 2nd. Princeton University Press., 2001.
- [63] P Nelson. *Biological Physics - Energy, Information, Life*. W. H. Freeman, 2004.

- [64] R Slopek, H McKinley, C Henderson, and V Breedveld. In situ monitoring of mechanical properties during photopolymerization with particle tracking microrheology. *Polymer*, 47(7):2263–2268, 2006.
- [65] J Xu, V Viasnoff, and D Wirtz. Compliance of actin filament networks measured by particle-tracking microrheology and diffusing wave spectroscopy. *Rheol. Acta*, 37:387–398, 1998.
- [66] T G Mason and D A Weitz. Optical measurements of frequency-dependent linear viscoelastic moduli of complex fluids. *Phys. Rev. Lett.*, 74:1250–1253, 1995.
- [67] A J Levine and T C Lubensky. One- and two-particle microrheology. *Phys. Rev. Lett.*, 85(8):1774–1777, 2000.
- [68] T G Mason, K Ganesan, J H van Zanten, D Wirtz, and S C Kuo. Particle tracking microrheology of complex fluids. *Phys. Rev. Lett.*, 79(17):3282–3285, 1997.
- [69] T G Mason. Estimating the viscoelastic moduli of complex fluids using the generalized stokes-einstein equation. *Rheol. Acta*, 39(4):371–378, 2000.
- [70] I Y Wong, M L Gardel, D R Reichman, E R Weeks, M Valentine, E R Bastow, and D A Weitz. Anomalous diffusion probes microstructure dynamics of entangled f-actin networks. *Phys. Rev. Lett.*, 92(17):178101, 2004.
- [71] M L Gardel, M Valentine, J C Crocker, E R Bastow, and D A Weitz. Microrheology of entangled f-actin solutions. *Phys. Rev. Lett.*, 91(15):158302, 2003.
- [72] R Tharmann, M M A E Claessens, and E R Bastow. Micro- and macrorheological properties of actin networks effectively cross-linked by depletion forces. *Biophys. J.*, 90(7):2622–2627, 2006.
- [73] A Goodman, Y Tseng, and D Wirtz. Effect of length, topology, and concentration on the microviscosity and microheterogeneity of DNA solutions. *J. Mol. Biol.*, 323(2):199–215, 2002.
- [74] S Sivaramakrishnan, J V DeGiulio, L Lorand, R D Goldman, and K M Ridge. Micromechanical properties of keratin intermediate filament networks. *Proc. Natl. Acad. Sci. USA*, 105(3):889–94, 2008.
- [75] B Hoffman, G Massiera, K Van Citters, and J Crocker. The consensus mechanics of cultured mammalian cells. *Proc. Natl. Acad. Sci. USA*, 103(27):10259–10264, 2006.
- [76] H Zhang, S L Baader, M Sixt, J Kappler, and U Rauch. Neurocan-GFP fusion protein: a new approach to detect hyaluronan on tissue sections and living cells. *J. Histochem. Cytochem.*, 52(7):915–922, 2004.
- [77] F Yang, L G Moss, and G N Phillips. The molecular structure of green fluorescent protein. *Nat. Biotech.*, 14(10):1246–1251, 1996.
- [78] R Tammi and M Tammi. Correlations between hyaluronan and epidermal proliferation as studied by [3H]glucosamine and [3H]thymidine incorporations and staining of hyaluronan on mitotic keratinocytes. *Exp. Cell Res.*, 195(2):524–7, 1991.
- [79] S Evanko, W Parks, and T Wight. Intracellular hyaluronan in arterial smooth muscle cells: Association with microtubules, RHAMM, and the mitotic spindle. *J. Histochem. Cytochem.*, 52(12):1525–1535, 2004.
- [80] M Sun. Multiple membrane tethers probed by atomic force microscopy. *Biophys. J.*, 89(6):4320–4329, 2005.

- [81] S Tsukita. ERM family members as molecular linkers between the cell surface glycoprotein CD44 and actin-based cytoskeletons. *J. Cell Biol.*, 126(2):391–401, 1994.
- [82] S Yonemura, S Tsukita, and S Tsukita. Direct involvement of ezrin/radixin/moesin (ERM)-binding membrane proteins in the organization of microvilli in collaboration with activated ERM proteins. *J. Cell Biol.*, 145(7):1497–1509, 1999.
- [83] L G Alexopoulos, L A Setton, and F Guilak. The biomechanical role of the chondrocyte pericellular matrix in articular cartilage. *Acta Biomater.*, 1(3):317–325, 2005.
- [84] J Dudhia, C M Davidson, T M Wells, D H Vynios, T Hardingham, and M T Bayliss. Age-related changes in the content of the C-terminal region of aggrecan in human articular cartilage. *Biochem. J.*, 313:933–940, 1996.
- [85] G Verbruggen, M Cornelissen, K F Almqvist, L Wang, D Elewaut, C Broddelez, L de Ridder, and E M Veys. Influence of aging on the synthesis and morphology of the aggrecans synthesized by differentiated human articular chondrocytes. *Osteoarthritis Cart.*, 8(3):170–179, 2000.
- [86] G Rizkalla, A Reiner, E Bogoch, and A R Poole. Studies of the articular cartilage proteoglycan aggrecan in health and osteoarthritis. Evidence for molecular heterogeneity and extensive molecular changes in disease. *J. Clin. Invest.*, 90(6):2268–2277, 1992.
- [87] P M Freeman, R N Natarajan, J H Kimura, and T P Andriacchi. Chondrocyte cells respond mechanically to compressive loads. *J. Orthop. Res.*, 12(3):311–320, 1994.
- [88] D Lee and D Bader. The development and characterization of an in vitro system to study strain-induced cell deformation. *In Vitro Cell. Dev. Bio. Animal*, 31(11):828–835, 1995.
- [89] S Roberts, M Knight, D Lee, and D Bader. Mechanical compression influences intracellular Ca^{2+} signaling in chondrocytes seeded in agarose. *J. Appl. Phys.*, 90:1385–1391, 2001.
- [90] M Knight, T Toyoda, D Lee, and D Bader. Mechanical compression and hydrostatic pressure induce reversible changes in actin cytoskeletal organisation in chondrocytes in agarose. *J. Biomech.*, 39(8):1547–1551, 2006.
- [91] T Momberger, J Levick, and R Mason. Hyaluronan secretion by synovioocytes is mechanosensitive. *Matrix Biol.*, 24(8):510–519, 2005.
- [92] R M Hochmuth. Micropipette aspiration of living cells. *J. Biomech.*, 33(1):15–22, 2000.
- [93] L G Alexopoulos, GM Williams, ML Upton, L A Setton, and F Guilak. Osteoarthritic changes in the biphasic mechanical properties of the chondrocyte pericellular matrix in articular cartilage. *J. Biomech.*, 38(3):509–517, 2005.
- [94] W R Trickey, F P T Baaijens, T A Laursen, L G Alexopoulos, and F Guilak. Determination of the Poisson’s ratio of the cell: recovery properties of chondrocytes after release from complete micropipette aspiration. *J. Biomech.*, 39(1):78–87, 2006.
- [95] D L Bader, T Ohashi, M Knight, D A Lee, and M Sato. Deformation properties of articular chondrocytes: a critique of three separate techniques. *Biorheology*, 39(1-2):69–78, 2002.

- [96] L Ng, H H Hung, A Sprunt, S Chubinskaya, C Ortiz, and A Grodzinsky. Nanomechanical properties of individual chondrocytes and their developing growth factor-stimulated pericellular matrix. *J. Biomech.*, 40(5):1011–1023, 2007.
- [97] I Sokolov, S Iyer, V Subba-Rao, R M Gaikwad, and C D Woodworth. Detection of surface brush on biological cells in vitro with atomic force microscopy. *Appl. Phys. Lett.*, 91:023902, 2007.
- [98] L G Alexopoulos, L A Setton, and F Guilak. The biomechanical role of the chondrocyte pericellular matrix in articular cartilage. *Acta Biomaterialia*, 1(3):317–325, 2005.
- [99] I. Teraoka. *Polymer Solutions*. Wiley-Interscience, New York, 2001.
- [100] W E Krause, E G Bellomo, and R H Colby. Rheology of sodium hyaluronate under physiological conditions. *Biomac.*, 2(1):65–69, 2001.
- [101] J Howard. *Mechanics of Motor Proteins and the Cytoskeleton*. Sinauer Associates, Inc., 2001.
- [102] T Fujii, Y Sun, K An, and Z Luo. Mechanical properties of single hyaluronan molecules. *J. Biomech.*, 35:527–531, 2002.
- [103] R Mendichi, L Soltes, and A G Schieroni. Evaluation of radius of gyration and intrinsic viscosity molar mass dependence and stiffness of hyaluronan. *Biomac.*, 4:1805–1810, 2003.
- [104] E Buhler and F Bou. Persistence length for a model semirigid polyelectrolyte as seen by small angle neutron scattering: a relevant variation of the lower bound with ionic strength. *Eur. Phys. J. E*, 10(2):89–92, 2003.
- [105] M K Cowman and S Matsuoka. *The intrinsic viscosity of hyaluronan*, pages 75–78. Woodhead Publishing limited, 2001.
- [106] M Cohen, D Joester, B Geiger, and L Addadi. Spatial and temporal sequence of events in cell adhesion: from molecular recognition to focal adhesion assembly. *ChemBioChem*, 5(10):1393–1399, 2004.
- [107] A Kultti, K Rilla, R Tiihonen, A P Spicer, R H Tammi, and M Tammi. Hyaluronan synthesis induces microvillus-like cell surface protrusions. *J. Biol. Chem.*, 281(23):15821–15828, 2006.
- [108] A Day and C de la Motte. Hyaluronan cross-linking: a protective mechanism in inflammation? *Trends in Immunology*, 26(12):637–643, 2005.
- [109] M Hellmann, M Weiss, and D W Heermann. Monte carlo simulations reveal the straightening of an end-grafted flexible chain with a rigid side chain. *Phys. Rev. E*, 76:021802, 2007.
- [110] R Richter, K Hock, J Burkhartsmeyer, H Boehm, P Bingen, G Wang, N F Steinmetz, D J Evans, and J P Spatz. Membrane-grafted hyaluronan films: A well-defined model system of glycoconjugate cell coats. *J. Am. Chem. Soc.*, 129(17):5306–5307, 2007.
- [111] R P Richter, R Berat, and A Brisson. Formation of solid-supported lipid bilayers: an integrated view. *Langmuir*, 2(8):3497–505, 2006.
- [112] J Schilling, K Sengupta, S Goennenwein, A R Bausch, and E Sackmann. Absolute interfacial distance measurements by dual-wavelength reflection interference contrast microscopy. *Phys. Rev. E*, 69:021901, 2004.

- [113] K Binder. Scaling concepts for polymer brushes and their test with computer simulation. *Europ. Phys. J. E*, 9:293–298, 2002.
- [114] S Alexander. Adsorption of chain molecules with a polar head: a scaling description. *J. Physique (Paris)*, 38:983–987, 1977.
- [115] S T Milner. Polymer brushes. *Science*, 251(4996):905–914, 1991.
- [116] B Zhao and W J Brittain. Polymer brushes: surface-immobilized macromolecules. *Progress in Polymer Sci.*, 25:677–710, 2000.
- [117] A Papagiannopoulos, C M Fernyhough, and T A Waigh. The microrheology of polystyrene sulfonate combs in aqueous solution. *J. Chem. Phys.*, 123(21):214904, 2005.
- [118] M Cowman and S Matsuoka. Experimental approaches to hyaluronan structure. *Carbohydrate Res.*, 340:791–809, 2005.
- [119] C Knudson and W Knudson. Cartilage proteoglycans. *Sem. Cell Dev. Bio.*, 12(2):69–78, 2001.
- [120] R F Loeser. Chondrocyte integrin expression and function. *Biorheology*, 37(1-2):109–16, 2000.
- [121] G M Lee and R F Loese. Interactions of the chondrocyte with its pericellular matrix. *Cells Mat.*, 8:135–149, 1998.
- [122] G M Lee, C A Poole, S S Kelley, J Chang, and B Caterson. Isolated chondrons: a viable alternative for studies of chondrocyte metabolism in vitro. *Osteoarthr. Cartil.*, 5(4):261–74, 1997.
- [123] A van der Flier and A Sonnenberg. Function and interactions of integrins. *Cell Tissue Res.*, 305(3):285–98, 2001.
- [124] G B Fields, J L Lauer, Y Dori, P Forns, Y C Yu, and M Tirrell. Protein-like molecular architecture: biomaterial applications for inducing cellular receptor binding and signal transduction. *Biopolymers*, 47(2):143–51, 1998.
- [125] S P Massia and J A Hubbell. An RGD spacing of 440 nm is sufficient for integrin alpha V beta 3-mediated fibroblast spreading and 140 nm for focal contact and stress fiber formation. *J. Cell Biol.*, 114(5):1089–100, 1991.
- [126] M Aumailley, M Gurrath, G Mueller, J Calvete, R Timpl, and H Kessler. Arg-Gly-Asp constrained within cyclic pentapeptides. strong and selective inhibitors of cell adhesion to vitronectin and laminin fragment P1. *FEBS Lett.*, 291(1):50–4, 1991.
- [127] M Gurrath, G Mueller, H Kessler, M Aumailley, and R Timpl. Conformation/activity studies of rationally designed potent anti-adhesive RGD peptides. *Eur. J. Biochem.*, 210(3):911–21, 1992.
- [128] M Pierschbacher and E Ruoslahti. Cell attachment activity of fibronectin can be duplicated by small synthetic fragments of the molecule. *Nature*, 309:30–33, 1984.
- [129] U Hersel, C Dahmen, and H Kessler. RGD modified polymers: biomaterials for stimulated cell adhesion and beyond. *Biomat.*, 24(24):4385–4415, 2003.
- [130] M Leiss, K Beckmann, A Giros, M Costell, and R Faessler. The role of integrin binding sites in fibronectin matrix assembly in vivo. *Curr. Opin. Cell Biol.*, 20:1–6, 2008.

- [131] M Pfaff, K Tangemann, B Muller, and M Gurrath. Selective recognition of cyclic RGD peptides of NMR defined conformation by different integrins. *J. Biol. Chem.*, 32(12):20233–20238, 1994.
- [132] J H Beer, K T Springer, and B S Coller. Immobilized Arg-Gly-Asp (RGD) peptides of varying lengths as structural probes of the platelet glycoprotein IIb/IIIa receptor. *Blood*, 79(1):117–28, 1992.
- [133] B Nies, G Hoelzemann, S Goodman, and H Kessler. Surface coating with cyclic RGD peptides stimulates osteoblast adhesion and proliferation as well as bone formation. *ChemBioChem*, 1(2):107–114, 2000.
- [134] R F Loeser. Integrin-mediated attachment of articular chondrocytes to extracellular matrix proteins. *Arthritis Rheum.*, 36(8):1103–10, 1993.
- [135] R F Loeser. Modulation of integrin-mediated attachment of chondrocytes to extracellular matrix proteins by cations, retinoic acid, and transforming growth factor beta. *Exp. Cell Res.*, 211(1):17–23, 1994.
- [136] J Bluemmel, N Perschmann, D Aydin, J Drinjakovic, T Surrey, M Lopez-Garcia, H Kessler, and J P Spatz. Protein repellent properties of covalently attached PEG coatings on nanostructured SiO₂-based interfaces. *Biomater.*, 28(32):4739–4747, 2007.
- [137] M Arnold. *Molecularly Defined Nanostructured Interfaces as Tools for the Regulation and the Measurement of Functional Length Scales in Cell Adhesion Mediating Protein Clusters*. PhD thesis, University Heidelberg, 2005.
- [138] M Arnold, E A Cavalcanti-Adam, R Glass, J Bluemmel, W Eck, M Kantlehner, H Kessler, and J P Spatz. Activation of integrin function by nanopatterned adhesive interfaces. *ChemPhysChem*, 5(3):383–388, 2004.
- [139] M Arnold, V Hirschfeld-Warneken, T Lohmueller, P Heil, J Bluemmel, E A Cavalcanti-Adam, M Lopez-Garcia, P Walther, H Kessler, B Geiger, and J P Spatz. Induction of cell polarization and migration by a gradient of nanoscale variations in adhesive ligand spacing. *Nano. Lett.*, 8(7):2063–2069, 2008.
- [140] V C Hirschfeld-Warneken, M Arnold, E A Cavalcanti-Adam, M Lopez-Garcia, H Kessler, and J P Spatz. Cell adhesion and polarisation on molecularly defined spacing gradient surfaces of cyclic RGDfK peptide patches. *Eur. J. Cell Biol.*, 87(8-9):743–750, 2008.
- [141] E A Cavalcanti-Adam, A Micoulet, J Bluemmel, J Auernheimer, H Kessler, and J P Spatz. Lateral spacing of integrin ligands influences cell spreading and focal adhesion assembly. *Eur. J. Cell Biol.*, 85(3-4):219–224, 2006.
- [142] E Cavalcanti-Adam, T Volberg, A Micoulet, H Kessler, B Geiger, and J P Spatz. Cell spreading and focal adhesion dynamics are regulated by spacing of integrin ligands. *Biophys. J.*, 92:2964–2974, 2007.
- [143] R Paul, P Heil, J P Spatz, and U S Schwarz. Propagation of mechanical stress through the actin cytoskeleton toward focal adhesions: model and experiment. *Biophys. J.*, 94(4):1470–82, 2008.
- [144] J P Spatz, V Chan, S Moesmer, F M Kamm, A Plettl, P Ziemann, and M Moeller. A combined top-down/bottom-up approach to the microscopic localization of metallic nanodots. *Adv. Mater.*, 14:1827–1832, 2002.
- [145] J P Spatz, T Herzog, S Moessmer, P Ziemann, and M Moeller. Micellar inorganic-polymer hybrid systems—a tool for nanolithography. *Adv. Mater.*, 11(2):149–153, 1999.

- [146] R Glass, M Moeller, and J P Spatz. Block copolymer micelle nanolithography. *Nanotech.*, 14:1153–1160, 2003.
- [147] P Girard, E A Cavalcanti-Adam, R Kemkemer, and J P Spatz. Cellular chemomechanics at interfaces: sensing, integration and response. *Soft Matter*, 3:307–326, 2007.
- [148] E Bock. *Deposition and Growth of Various Nanomaterials at Nanostructured Interfaces*. PhD thesis, University Heidelberg, 2008.
- [149] G Kaestle, H G Boyen, F Weigl, G Lengl, T Herzog, P Zieman, S Riethmueller, O Mayer, C Harmann, J P Spatz, M Moeller, M Ozawa, F Banhart, M G Garnier, and P Oelhafen. Micellar nanoreactors-preparation and characterization of hexagonally ordered arrays of metallic nanodots. *Adv. Funct. Mat.*, 13(11):853–861, 2003.
- [150] T Lohmueller. *Nanostructured Functional Materials*. PhD thesis, University Heidelberg, 2008.
- [151] Z Gao and A Eisenberg. A model of micellization for block copolymers in solutions. *Macromol.*, 26(26):7353–7360, 1993.
- [152] A Johner and J F Joanny. Block copolymer adsorption in a selective solvent: A kinetic study. *Macromol.*, 23(26):5299–5311, 1991.
- [153] J C Meiners, H Elbs, A Ritzi, J Mlynek, and G Krausch. Chemically functionalized surfaces from ultrathin block-copolymer films. *J. Appl. Phys.*, 80(4):2224–2227, 1996.
- [154] Z Li, W Zhao, Y Liu, M H Rafailovich, J Sokolov, K Khougaz, A Eisenberg, R B Lennox, and G Krausch. Self-ordering of diblock copolymers from solution. *J. Am. Chem. Soc.*, 118(44):10892–10893, 1996.
- [155] J C Meiners, A Quintel-Ritzi, J Mlynek, H Elbs, and G Krausch. Adsorption of block-copolymer micelles from a selective solvent. *Macromol.*, 30(17):4945–4951, 1997.
- [156] J P Spatz, S Mossmer, C Hartmann, M Moeller, T Herzog, M Krieger, H G Boyen, P Ziemann, and B Kabius. Ordered deposition of inorganic clusters from micellar block copolymer films. *Langmuir*, 16(2):407–415, 2000.
- [157] J Bansmann, S Kielbassa, H Hoster, F Weigl, H G Boyen, U Wiedwald, P Ziemann, and R J Behm. Controlling the interparticle spacing of Au-salt loaded micelles and Au nanoparticles on flat surfaces. *Langmuir*, 23:10150–10155, 2007.
- [158] L Landau and B Levich. Dragging of a liquid by a moving plate. *Acta Physicochim. URSS*, 17(42), 1942.
- [159] A Darhuber, S M Troian, J M Davis, S M Miller, and S Wagner. Selective dip-coating of chemically micropatterned surfaces. *J. Appl. Phys.*, 88(9):5119–5126, 2000.
- [160] S H Yun, S I Yoo, J C Jung, W C Zin, and B H Sohn. Highly ordered arrays of nanoparticles in large areas from diblock copolymer micelles in hexagonal self-assembly. *Chem. Mat.*, 18:5654–5648, 2006.
- [161] G Becherer, G Herms, and P Ahrenholz. Die Ermittlung von radialen Verteilungsfunktionen aus dem Beugungsbild zweidimensionaler amorpher Strukturen. *Ann. Phys.*, 472(3-4):166–176, 1966.
- [162] C A Murray and D G Grier. Video microscopy of monodisperse colloidal systems. *Ann. Rev. Phys. Chem.*, 47(1):421–462, 1996.

- [163] D Nelson. Reentrant melting in solid films with quenched random impurities. *Phys. Rev. B*, 27:2902, 1983.
- [164] B Halperin and D Nelson. Theory of two-dimensional melting. *Phys. Rev. Lett.*, 41(2):121–124, 1978.
- [165] D Nelson and B Halperin. Dislocation-mediated melting in two dimensions. *Phys. Rev. B*, 19(2457), 1979.
- [166] S Krishnamoorthy, R Pugin, J Brugger, H Heinzelmann, and C Hinderling. Nanopatterned self-assembled monolayers by using diblock copolymer micelles as nanometer-scale adsorption and etch masks. *Adv. Mat.*, 20(10):1962–1965, 2008.
- [167] S Krishnamoorthy, R Pugin, J Brugger, H Heinzelmann, and C Hinderling. Tuning the dimensions and periodicities of nanostructures starting from the same polystyrene-block-poly(2-vinylpyridine) diblock copolymer. *Adv. Funct. Mat.*, 16(11):1469–1475, 2006.
- [168] S Foerster, M Zisenis, E Wenz, and M Antonietti. Micellization of strongly segregated block copolymers. *J. Chem. Phys.*, 104(24):9956–9970, 1996.
- [169] S Forster and T Plantenberg. Von selbstorganisierenden Polymeren zu Nanohybrid- und Biomaterialien. *Angew. Chem.*, 114(712–739), 2002.
- [170] A Koehler. New system of illumination for photomicrographic purposes. *Z. Wiss. Mikroskopie*, 10:433–440, 1893.
- [171] A S G Curtis. The mechanism of adhesion of cells to glass a study by interference reflection microscopy. *J. Cell Biol.*, 20:199–215, 1964.
- [172] J Raedler and E Sackmann. On the measurement of weak repulsive and frictional colloidal forces by reflection interference contrast microscopy. *Langmuir*, 8:848–853, 1992.
- [173] J Ploem. *Reflection Contrast microscopy as a tool for investigation of the attachment of living cells to a glass surface*. Blackwell Scientific Publications, Oxford, 1975.
- [174] A Albersdoerfer and E Sackmann. Swelling behavior and viscoelasticity of ultrathin grafted hyaluronic acid films. *Euro. Phys. J. B*, 10:663–672, 1999.
- [175] K Sengupta, J Schilling, S Marx, M Fischer, A Bacher, and E Sackmann. Mimicking tissue surfaces by supported membrane coupled ultrathin layer of hyaluronic acid. *Langmuir*, 19:1775–1781, 2003.
- [176] J Bereiter-Hahn, C H Fox, and B Thorell. Quantitative reflection contrast microscopy of living cells. *J. Cell Biol.*, 82:767–779, 1979.
- [177] L Limozin and K Sengupta. Modulation of vesicle adhesion and spreading kinetics by hyaluronan cushions. *Biophys. J.*, 93(9):3300–3313, 2007.
- [178] N C Shaner, R E Campbell, P A Steinbach, B N G Giepmans, A E Palmer, and R Y Tsie. Improved monomeric red, orange and yellow fluorescent proteins derived from *Discosoma* sp. red fluorescent protein. *Nat. Biotech.*, 22:1567–1572, 2004.
- [179] X Shu, N Shaner, C Yarbrough, and R Tsien. Novel chromophores and buried charges control color in mFruits. *Biochemistry*, 45(32):9639–9647, 2006.
- [180] A Kim, V Manoharan, and J Crocker. Swelling-based method for preparing stable, functionalized polymer colloids. *J. Am. Chem. Soc.*, 127:1592–1593, 2005.

- [181] N E Dorsey. *Table of viscosity data from Properties of Ordinary Water-Substance*.
N E Dorsey, 1940.

Danksagung

Mein ganz besonderer Dank geht zu allererst an Joachim Spatz. In ihm habe ich einen Doktorvater gefunden, der mich durchweg in sämtlichen Situationen unterstützt hat. Ob es darum ging, Kontakte mit anderen Gruppen zu knüpfen, die benötigten technischen Bedingungen und Spielzeuge zur Verfügung zu haben oder ein paar Monate in Boston zum Auswerten der Experimente zu verbringen, immer fand er Wege und Möglichkeiten, Hindernisse aus dem Weg zu räumen. Vielen Dank für das in mich gesetzte Vertrauen, die Unterstützung und das Interesse an dieser Arbeit!

Jonathan Sleeman möchte ich für sein fortwährendes Interesse an diesem Projekt und seine Bereitschaft, das Gutachten für diese Arbeit zu erstellen, herzlich danken.

Jennifer Curtis not only introduced me to this inspiring project, but has also become a great friend. I especially thank her for the wonderful month with her and her family in Atlanta.

Ein Großteil dieser Arbeit ist in Zusammenarbeit mit einigen wirklich ausgezeichneten Studenten entstanden, die mit viel Engagement und Interesse diese Arbeit erheblich bereichert haben: Tabea Mundinger, Valentin Hagel, Martin Etzrodt und Daniel Barzan. Vielen Dank an Euch!

This work would not have been possible without the help of several cooperation partners, who did not only provide materials, but also motivation and incentives for his work. I especially like to thank Benni Geiger, Derk Joester, Uwe Rauch and Victor Breedveld and Horst Kessler.

Ralf Richter und Jennifer Curtis möchte ich für unsere intensiven HA-Diskussionsrunden danken, in denen zwei Physiker und ein Chemiker versuchten das Geheimnis dieses vielseitigen Biomoleküls zu lüften.

Mein großer Dank geht an Eva Bock und Theobald Lohmueller für die Einführung in die Herstellung und Charakterisierung der nanostrukturierten Oberflächen. Ganz besonders danken möchte ich Euch jedoch dafür, dass ihr mich trotz meiner anfänglichen vehementen Weigerung schließlich für diese Technik begeistern konntet.

Ganz herzlich möchte ich mich bei Eva Bock für das zweite "Zu Hause" in Stuttgart während der langen Pendelzeit bedanken!

Ada Calvacanti-Adam und Julia Ranzinger gilt mein Dank für die konstante Hilfe bei allen Fragen rund um die Zellen.

Danken möchte ich Lisa Maus für die Unterstützung im Labor und ihre ausgiebige Hilfe beim Schreiben meines ersten Papers und ganz besonders für ihre Freundschaft.

Für die hilfreichen Anmerkungen und Korrekturen meiner Arbeit bedanke ich mich ganz besonders bei Christian Schmitz, wie auch bei Lisa Maus, Claudia Pacholski, Eva Bock, Ilia Louban und Theobald Lohmueller. Ein herzliches Dankeschön für die Englischkorrektur geht an Nadine Koerber.

Für die Herstellung zahlreicher Sonderanfertigungen bedanke ich mich bei den

Werkstätten an der Universität Heidelberg und dem MPI, sowie der Elektronikwerkstatt der Universität Heidelberg.

Außerdem möchte ich mich für die tatkräftige Hilfe der Techniker, besonders bei Richard Morlang, Janis Grigoridis, Margit Kapp, Sigrit Riese und Henriette Ries bedanken.

Ich möchte mich ganz herzlich bei Daniel Barzan, Markus Abel und Julia Ranzinger bedanken, dass sie mehrfach den Weg zur Schlachtereierie übernommen haben, um das für diese Arbeit benötigte frische Schweineblut zu besorgen!

Ein ganz großes Danke geht an die Heidelberger Jungs für viele lustige Stunden bei Grillabenden, Konferenzausflügen und Kaffeepausen und unserer inspirierende Frühstücksrunde!

Dem Stuttgarter Teil unseres Arbeitskreises möchte ich ganz herzlich danken, dass sie mich nach meinem Umzug nach Stuttgart so herzlich aufgenommen haben.

An allen Ecken und Enden haben viele weitere Leute aus unserem AK mitgeholfen, die hier aus Platzgründen nicht einzeln aufgeführt sind: Ihnen gilt ein ganz besonderes Dankeschön!

Auch außerhalb der Arbeit hatte ich das Glück, viele Menschen um mich zu haben, die mich unterstützten und die Freuden und Leiden der letzten Jahre mit mir durchlebt haben. Ganz besonders möchte ich mich bei meinen Heidelberger Mädels bedanken, die leider in alle Winde verweht wurden: Ich bin so froh, dass es Euch gibt!

Auch das unerschütterliche Vertrauen und die Liebe meiner Schwester haben mir immer wieder neue Kraft geschenkt, sowie die Unterstützung meiner Großeltern und Eltern sowie meiner zukünftigen Schwiegereltern.

Und zum Schluss möchte ich dem Menschen danken, der mir wissenschaftlich wie privat die allergrößte Hilfe in den letzten Jahren war und wagemutig genug ist, den Rest seines Lebens an meiner Seite verbringen zu wollen.

Ich erkläre hiermit, dass ich die vorgelegte Dissertation selbst verfasst und mich keiner anderen als der von mir ausdrücklich bezeichneten Quellen und Hilfen bedient habe.

Heidelberg, den 28. Oktober 2008

.....

Heike Boehm